Monthly Notices
of the
ROYAL ASTRONOMICAL SOCIETY

MNRAS **436,** 1919–1954 (2013)
Advance Access publication 2013 October 22

doi:10.1093/mnras/stt1673

Characterization of SCUBA-2 450 μm and 850 μm selected galaxies in the COSMOS field

Caitlin M. Casey,[1]★† Chian-Chou Chen,[1] Lennox L. Cowie,[1] Amy J. Barger,[1,2,3] Peter Capak,[4] Olivier Ilbert,[5] Michael Koss,[1] Nicholas Lee,[1] Emeric Le Floc'h,[6] David B. Sanders[1] and Jonathan P. Williams[1]

[1]*Institute for Astronomy, University of Hawai'i, 2680 Woodlawn Dr, Honolulu, HI 96822, USA*
[2]*Department of Astronomy, University of Wisconsin-Madison, 475 North Charter Street, Madison, WI 53706, USA*
[3]*Department of Physics and Astronomy, University of Hawai'i, 2505 Correa Road, Honolulu, HI 96822, USA*
[4]*Spitzer Science Center, California Institute of Technology, 1200 E. California Blvd, Pasadena, CA, 91125, USA*
[5]*Laboratoire d'Astrophysique de Marseille, 38 rue Frederic Joliot Curie, F-13388 Marseille, France*
[6]*CEA-Saclay, Orme des Merisiers, Bat. 709, F-91191 Gif-sur-Yvette, France*

Accepted 2013 September 4. Received 2013 August 5; in original form 2013 February 11

ABSTRACT

We present deep 450 μm and 850 μm observations of a large, uniformly covered 394 arcmin^2 area in the Cosmic Evolution Survey (COSMOS) field obtained with the SCUBA-2 instrument on the James Clerk Maxwell Telescope (JCMT). We achieve root-mean-square noise values of $\sigma_{450} = 4.13$ mJy and $\sigma_{850} = 0.80$ mJy. The differential and cumulative number counts are presented and compared to similar previous works. Individual point sources are identified at $>3.6\sigma$ significance, a threshold corresponding to a 3–5 per cent sample contamination rate. We identify 78 sources at 450 μm and 99 at 850 μm, with flux densities $S_{450} = 13$–37 mJy and $S_{850} = 2$–16 mJy. Only 62–76 per cent of 450 μm sources are 850 μm detected and 61–81 per cent of 850 μm sources are 450 μm detected. The positional uncertainties at 450 μm are small (1–2.5 arcsec) and therefore allow a precise identification of multiwavelength counterparts without reliance on detection at 24 μm or radio wavelengths; we find that only 44 per cent of 450 μm sources and 60 per cent of 850 μm sources have 24 μm or radio counterparts. 450 μm selected galaxies peak at $\langle z \rangle = 1.95 \pm 0.19$ and 850 μm selected galaxies peak at $\langle z \rangle = 2.16 \pm 0.11$. The two samples occupy similar parameter space in redshift and luminosity, while their median SED peak wavelengths differ by ∼20–50 μm (translating to $\Delta T_{\rm dust} = 8$–12 K, where 450 μm selected galaxies are warmer). The similarities of the 450 μm and 850 μm populations, yet lack of direct overlap between them, suggests that submillimetre surveys conducted at any single far-infrared wavelength will be significantly incomplete ($\gtrsim$30 per cent) at censusing infrared-luminous star formation at high z.

Key words: galaxies: evolution – galaxies: high-redshift – galaxies: starbursts – infrared: galaxies.

1 INTRODUCTION

The arrival of the Submillimeter Common User Bolometer Array (SCUBA; Holland et al. 1999) on the James Clerk Maxwell Telescope (JCMT) 15 years ago ushered in a new age of galaxy evolution studies by highlighting the importance of distant infrared-bright, ultraluminous galaxies to the buildup of the Universe's stellar mass and the formation of massive, local elliptical galaxies. Submillimetre galaxies (SMGs; canonically selected at 850 μm with $S_{850} \gtrsim 2$–5 mJy; Smail, Ivison & Blain 1997; Barger et al. 1998; Hughes et al. 1998; Eales et al. 1999) have since been shown to have a peak volume density at $z \approx 2.2$–2.5 (Chapman et al. 2003, 2005; Yun et al. 2012). Follow-up studies of their molecular and ionized gas properties (Neri et al. 2003; Swinbank et al. 2004; Greve et al. 2005; Tacconi et al. 2006, 2008; Bothwell et al. 2010; Engel et al. 2010; Banerji et al. 2011; Alaghband-Zadeh et al. 2012) indicate that most star formation in bright SMGs is triggered by major mergers of gas-rich disc galaxies, similar to local (ultra-)

★ Hubble Fellow.
† E-mail: cmcasey@ifa.hawaii.edu

luminous infrared galaxies, (U)LIRGs (e.g. Sanders et al. 1988; Sanders & Mirabel 1996; Armus et al. 2009; U et al. 2012). Furthermore, several detailed studies of the X-ray and mid-infrared (MIR) properties of SMGs have led to the conclusion that the majority of the SMGs' bolometric energy is star formation dominated (Alexander et al. 2005; Coppin et al. 2008, 2010; Pope et al. 2008; Menéndez-Delmestre et al. 2009; Laird et al. 2010). However, several recent studies have pointed out that, despite their extreme star formation rates $\gtrsim$200 $M_\odot$ yr^{-1}, SMGs and high-z ULIRGs are not homogeneously described by major mergers (e.g. Daddi et al. 2009; Bothwell et al. 2010; Elbaz et al. 2011; Rodighiero et al. 2011; Targett 2011; Alaghband-Zadeh et al. 2012; Hayward et al. 2012). It is clear that the driving physical mechanisms for SMGs remain a puzzle at high z despite these detailed multiwavelength studies.

The limiting factors in the analysis and characterization of SMGs are small number statistics and the lack of secure counterpart identifications. The vast majority of the studies mentioned above – although thorough – are based on small samples of SMGs, anywhere from 2 to 75 galaxies (but mostly on samples with less than 10 sources). Some of these SMGs could have been mischaracterized due to incorrect counterpart identifications, which may be a consequence of the large beamsize of submm single-dish observations (the JCMT beamsize at 850 μm is ∼15 arcsec). The problem of limited statistics can be alleviated by wide-field submillimetre mapping. Mapping large regions of sky at long wavelengths is technically challenging, particularly if the maps are intended to be sufficiently deep and sensitive enough to detect unlensed galaxies in the early Universe. New submillimetre/far-infrared (FIR) facilities, such as AzTEC (Wilson et al. 2008) and primarily *Herschel Space Observatory* (Pilbratt et al. 2010), have mapped larger sky areas in recent years. *Herschel* has mapped hundreds of square degrees at 250–500 μm (Eales et al. 2010; Oliver et al. 2012). However, its surveys are more limited in sensitivity than SCUBA, primarily due to the smaller primary dish, which results in large beam sizes and much higher confusion limits.

The new Submillimeter Common User Bolometric Array-2 (Scuba-2; Holland et al. 2013) instrument on JCMT presents exciting new avenues to explore infrared-bright starbursts in the early Universe. Besides the four-fold increase in bolometer arrays and large field-of-view scans, which make 850 μm mapping more efficient than it was with Scuba, the Scuba-2 450 μm bolometers provide the first opportunity to identify 450 μm bright sources with remarkable resolution in the FIR; the JCMT beamsize at 450 μm is ∼7 arcsec, compared to ∼36 arcsec at 500 μm on *Herschel*. Direct detection in the FIR with a small beamsize is a large step forward, since multiwavelength counterpart identification has been a key limiting factor in the interpretation of submillimetre-bright sources over the past decade. Deep Scuba-2 maps, which are much less limited by confusion noise, are the scientific complement to the large-scale mapping done with *Herschel*.

This paper presents 450 μm and 850 μm observations from Scuba-2 in a central region of the Cosmic Evolution Survey (COSMOS) field (Scoville et al. 2007) surrounding the Cosmic Assembly Near-infrared Deep Extragalactic Legacy Survey (CANDELS) area. Recently, Geach et al. (2013) presented deep Scuba-2 450 μm observations in the central ∼100 arcmin^2 of this area. Our observations have a wider, more uniform coverage than the data presented in Geach et al. (2013), with the motivation of selecting a homogeneous sample, while the Geach et al. (2013) data are deeper and patterned to find fainter sources. The pointing on the CANDELS area is motivated by the perceived high correlation of submillimetre emission with near-infrared (NIR) emission (e.g. Wang, Cowie & Barger 2006; Serjeant et al. 2008) and the ability to morphologically characterize SMG counterparts using the *Hubble Space Telescope*'s high spatial resolution. However, we leave the detailed morphological analysis of these galaxies to a future work. This work is also complemented by the deeper, yet smaller area Scuba-2 coverage and analysis in the lensed cluster field A 370 by Chen et al. (2013), which currently provides the deepest 450 μm counts.

Section 2 describes our Scuba-2 observations and data reduction as well as ancillary data used, Section 3 discusses the identification and flux density measurements of point sources in the maps and differential and cumulative number counts, Section 4 describes the multiwavelength properties of the Scuba-2-selected galaxies and Section 5 discusses their implications, relation to similar starburst galaxy populations and implications for future, deeper Scuba-2 observations. Throughout we assume a Λcold dark matter cosmology with $H_0 = 71$ km s^{-1} Mpc^{-1} and $\Omega_m = 0.27$ (Hinshaw et al. 2009).

2 OBSERVATIONS AND DATA

Observations were taken with the Scuba-2 instrument on the JCMT on 2011-Dec-26, 2011-Dec-28, 2012-Feb-04, 2012-Feb-05, 2012-Feb-07, 2012-Apr-09, 2012-Apr-30, 2012-May-01, 2012-May-02, and 2012-Dec-21 under programs M11BH11A, M12AH11A and M12BH21A. Conditions were optimum, with the optical depth varying from $0.02 < \tau_{225\mathrm{GHz}} < 0.05$ and averaging $\tau_{225\,\mathrm{GHz}} \approx 0.04$. At the wavelengths of our observations, the optical depths were approximately $\tau_{450\,\mu\mathrm{m}} \approx 0.55$ and $\tau_{850\,\mu\mathrm{m}} \approx 0.16$. The integration times on-field per night were 3.5 h, 3.6 h, 3.1 h, 5.5 h, 5.5 h, 4.5 h, 2.9 h, 3.8 h, 0.6 h and 5.0 h, respectively, totalling 38.0 h on-field. We centred our map at position 10:00:28.0, +02:24:00. See Fig. 1 for a map of the galaxy density in the surrounding area along with areas

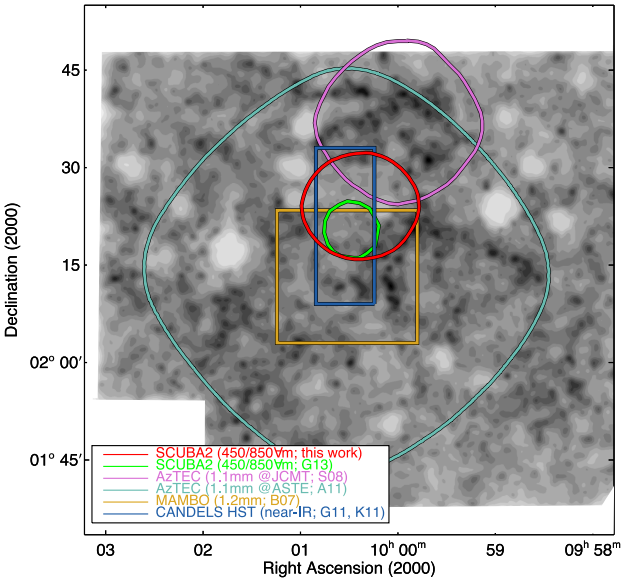

Figure 1. The surface density of galaxies showing large-scale structure in the COSMOS field (darker shades indicate the most dense areas). This uses the most recent compilation in Scoville et al. (2013). Overplotted are the areas surveyed in the submillimetre at 1.2 mm (with MAMBO, gold; Bertoldi et al. 2007), at 1.1mm (with AzTEC on JCMT, lavender; Scott et al. 2008), at 1.1 mm (with AzTEC on ASTE, teal; Aretxaga et al. 2011). Our 450/850 μm Scuba-2 coverage area is shown in red, and the Scuba-2 coverage of Geach et al. (2013) is shown in green. The CANDELS deep NIR *HST* coverage area is shown in blue.

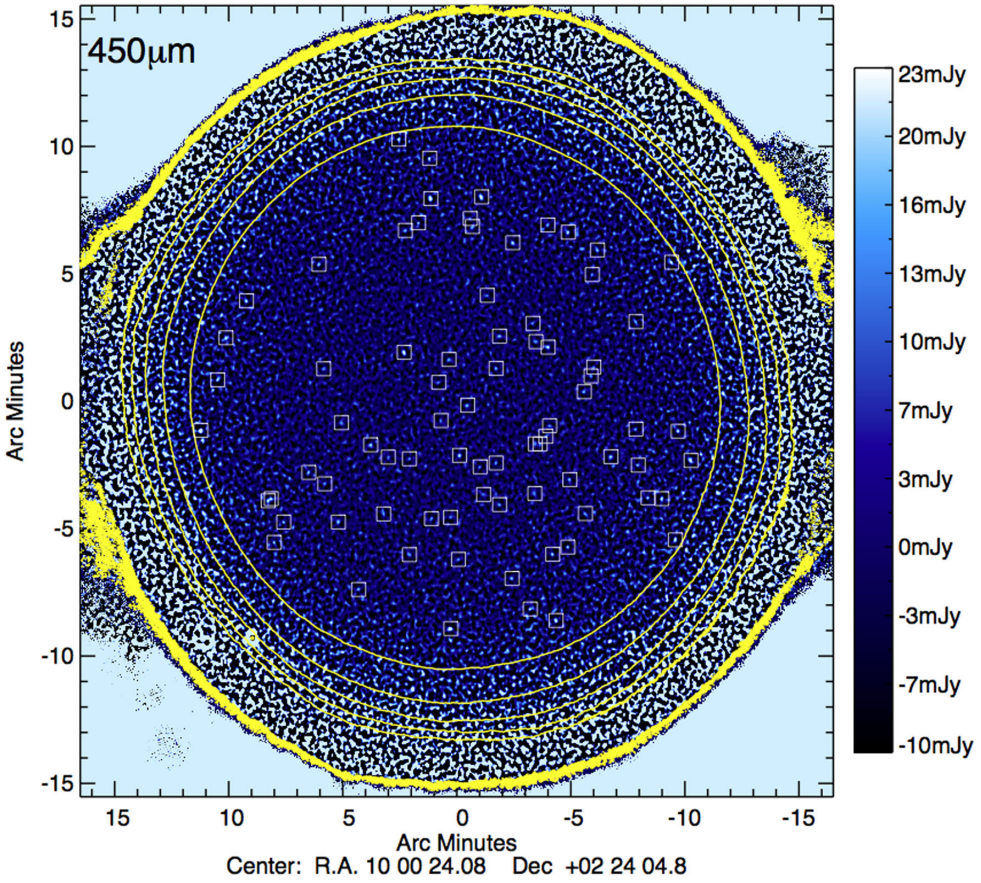

Figure 2. The COSMOS 450 μm SCUBA-2 map. The colour scale is linear with upper and lower ranges of $-10 < S_{450} < 23$ mJy beam^{-1}. Contours mark the 2, 3, 4, 5 and 6× the central rms value, measured to be 4.13 mJy beam^{-1} at 450 μm. We search for sources which are detected with rms less than double the central value (roughly corresponding to the innermost contour). The area probed by this cut has a radius ∼11.2 arcmin and an area ∼394 arcmin^2. The 450 μm identified $>3.6\sigma$ sources are identified with white boxes (a justification of the 3.6σ cut can be found in the text).

covered at other submm–mm wavelengths. The PONG-900 mapping pattern was used to achieve a uniform rms over a large area ≈15 × 15 arcmin in preference to the Daisy mapping which has substantial patterning and non-uniformity and covers a smaller area.

Raw data were downloaded via the Canadian Astronomy Data Centre (CADC) JCMT Science Archive and processed with the SCUBA-2 software packages SMURF, the Sub-Millimetre User Reduction Facility and PICARD, Pipeline for Combining and Analysing Reduced Data. Data were split up by night, wavelength and sub-array for processing. SMURF processing was first executed on each night's sub-array data [which is equivalent to combining each sub-array per Minimum Scheduable Block (MSB), and then combining all MSBs]. Partial maps were constructed using the MAKEMAP routine (Chapin et al. 2013) in SMURF with the default deep extragalactic configuration file optimising background subtraction. The MAKEMAP uncalibrated maps were combined at each stage (by sub-array, then nights) using the PICARD recipe MOSAIC_JCMT_IMAGES. Each of the four sub-arrays at 450 μm and 850 μm were combined for each night's worth of data, and then the nights were combined to produce the unprocessed, raw maps at 450 μm and 850 μm in units of pW.

We applied the matched-filter PICARD recipe to suppress pattern noise and increase the signal from individual sources, which are generally unresolved. At 450 μm, the map rms noise drops substantially from 14.08 to 4.13 mJy. A similar yet less dramatic drop is seen at 850 μm, from 2.18 mJy to 0.80 mJy. Flux calibration is done by applying the measured flux conversion factors (FCF) from the first eight months of calibrator data, primarily from Uranus and Mars ($\mathrm{FCF}_{850} = 556 \pm 45$ Jy pW^{-1} beam^{-1} and $\mathrm{FCF}_{450} = 606 \pm 55$ Jy pW^{-1} beam^{-1}). These flux conversions factors differ from the current canonical values (Dempsey et al. 2013) because we used an earlier version of PICARD. Calibration data taken during the observations for this project agree with these FCF values to ∼10 per cent. Final reduced maps, in units of mJy beam^{-1}, are shown in Figs 2 and 3. The units are such that the flux density, in mJy, for an unresolved source is simply the sources' peak value in the map. Signal-to-noise ratio (S/N) maps are constructed using the PICARD recipe MAKESNR; these are not shown here but are quite similar to the final reduced maps within the central area. We found no evidence for a systematic astrometric offset necessary after inspection of the radio data described in the next section (following the astrometric calibration procedure of Chen et al. 2013). S/N maps are used for the identification of point sources.

To avoid contamination from the less sensitive edges of the map in calculating an overall characteristic map noise, we first measured the effective area of the sensitive region of the map, where the rms was less than or equal to a factor of 2 times the rms in the centre. We determined this boundary by measuring the rms in concentric annuli 5 arcsec wide from a jackknife map, having subtracted out the signal from point sources. The jackknife map represents the instrumental noise of our observations with sources removed and is constructed by subtracting one half of our data from the other,

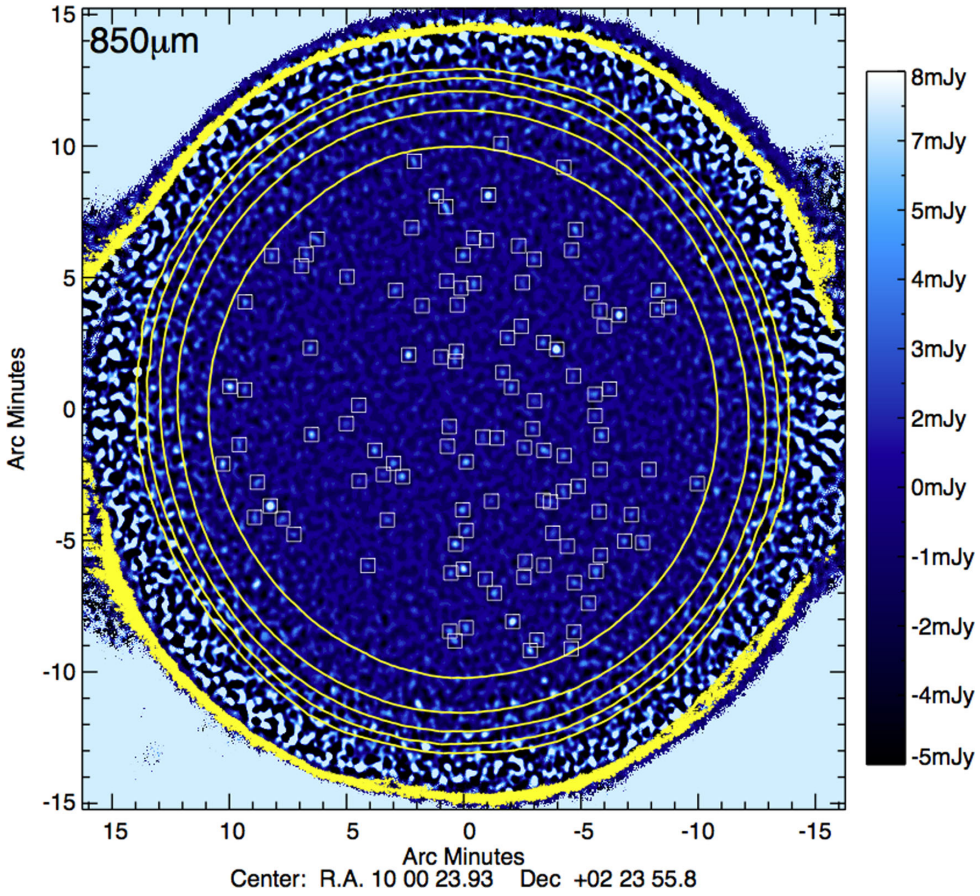

Figure 3. The COSMOS 850 μm SCUBA-2 map, plotted in the same fashion as Fig. 2. The colour scale is linear and runs from $-5 < S_{850} < 8$ mJy beam^{-1}, and the measured central rms is 0.80 mJy beam^{-1}. All $>3.6\sigma$ sources are marked with white boxes. Some sources appear outside the nominal 2×rms contour, but locally have noise that dips below the 2×rms threshold.

then scaling the noise by the square root of the integration time. This 2 × rms boundary lies ∼11.2 arcmin from the map centre in both the 450 μm and 850 μm maps, corresponding to an area of 394 arcmin^2, slightly larger than the anticipated 15 × 15 arcmin PONG-900 target area.

The pixel flux distributions for the ∼400 arcmin^2 central region are shown in Fig. 4 with the distributions of the jackknife pure-noise maps, in the same ∼400 arcmin^2 area, highlighted in grey. The positive excess above the jackknife noise map is attributed to the detection of real sources. The negative flux excesses (prominent at 850 μm) is due to troughs around high-S/N sources and is a characteristic of the removal of pattern noise and is exaggerated by the matched-filter technique. In other words, in order to boost the signal in real sources, especially at S/N > 5, matched-filter creates rings or troughs of negative flux surrounding the source. Since there are 44 850 μm sources at S/N > 5 and only 8 450 μm sources at S/N > 5, the effect of a negative excess is more pronounced at 850 μm.

2.1 COSMOS ancillary data

We use the vast ancillary data available in the COSMOS field (Scoville et al. 2007) to investigate the physical nature of the SCUBA-2 submillimetre-bright sources and compare with larger samples of submillimetre sources previously analysed in the literature. The imaging and associated data reduction for *Spitzer Space Telescope* InfraRed Array Camera (IRAC) and MIPS data is described in Sanders et al. (2007), Le Floc'h et al. (2009) and Frayer et al. (2009).

Photometric redshifts were fit using the LE PHARE[1] code (Ilbert et al. 2009, 2010) to multi-band ultraviolet, optical, near-infrared (NIR) and MIR photometry. Stellar population templates (Bruzual & Charlot 2003; Polletta et al. 2007) were assumed as input to LE PHARE. Extinction is a free parameter of the fit and is given a maximum value of $E(B-V) = 0.5$, where galaxies redder than Sb have no extinction (i.e. assuming older stellar populations rather than dustier systems). Not allowing a wider range of extinctions could impact the quality of photometric redshifts in our sample, despite the fact taht 30+ photometric bands are used to measure redshift; this is an issue we will investigate in a future work.

In this paper we quote the measured LE PHARE output parameters of stellar mass and star formation rate from the Ilbert et al. (2009) catalogue for contrast. Both are measured from stellar template matching to UV/optical/NIR photometry only, and in this paper, we refer to the template star formation rate as 'SFR_{UV}'. While this SED fitting method is widely used for large, catalogue-based approaches to galaxy characterization, we note that it differs from the method of using the ultraviolet slope, β, for measuring dust attenuation (and therefore dust-corrected total star formation rates). The latter method is used by Meurer, Heckman & Calzetti (1999)

[1] http://www.cfht.hawaii.edu/~arnouts/LEPHARE/cfht_lephare/lephare.html

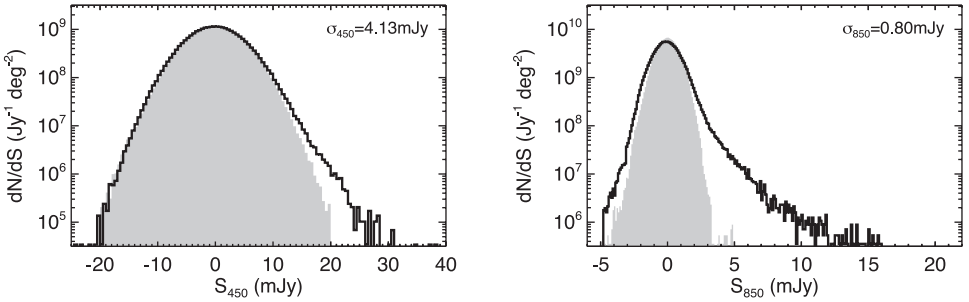

Figure 4. Pixel flux distributions (per unit area) within the central ∼400 arcmin^2 area at 450 μm and 850 μm. The solid black lines indicate the distributions of the data, showing excesses at high flux densities where point sources contribute to the distributions. At lower flux densities, the distributions are dominated by instrument noise. The negative excesses are due to residual troughs around bright sources (a characteristic of the matched filter technique). The grey shaded histograms show the pixel noise distributions within the same region for the jackknife maps. As discussed in the text, the jackknife maps were constructed by differencing two halves of the data, which removes point sources and leaves only residual noise.

and Reddy et al. (2012), among others, and is shown to more accurately predict dust attenuation in luminous infrared galaxies. We discuss the contrasting SFR measures later in Section 5.2.

3 IDENTIFICATION OF POINT SOURCES

Point sources are extracted in each map by isolating high S/N pixel groups (e.g. adjacent pixels) in the S/N maps. Within each pixel group, the highest S/N pixel marks the object centre and point at which the raw flux density is measured. The raw flux densities are measured as the peak flux density of the source in mJy beam^{-1}, assuming the sources are unresolved (a safe assumption for high-redshift infrared galaxies).

Here we describe our use of Monte Carlo simulations to determine an appropriate detection threshold for reporting detections, and for measuring number counts, boosting factors and completeness and contamination rates.

3.1 Monte Carlo simulations

The estimation of cumulative number counts at both 450 μm and 850 μm, along with the completeness and contamination rates of our samples, deboosting factors, and adequate detection thresholds requires the use of Monte Carlo simulations. This is an iterative process which sheds light on the observational impact and limitations on the true number counts (see Coppin et al. 2005, for a thorough description of the process). Monte Carlo testing is done by injecting fake sources into a pure-noise, or jackknife, map. Injecting sources into our map with known flux densities and positions, we can measure the accuracy by which we recover those sources using the above extraction method.

Injecting fake sources into a noise map requires an a priori assumption of intrinsic number counts; at 450 μm, we vary the fit parameters from Chen et al. (2013) and Geach et al. (2013), which use a double-power law and Schechter form, respectively, until our measured raw number counts match those found in our Monte Carlo simulations. At 850 μm, we vary the parameters around those used in Knudsen, van der Werf & Kneib (2008). We use the Knudsen et al. initial variables to take advantage of data at the faintest flux densities (which are in agreement with previous blank-field number counts work; Coppin et al. 2006). To generate substantial statistical samples of input and extracted sources, we generate 200 maps at both wavelengths (which generates ∼10 000 extracted sources). Boosting, positional offset, completeness and contamination are all estimated using the known input sample, position and flux density, and the measured output sample, position, flux density and S/N.

The flux densities of sources we measure from our maps need correction for flux boosting. Sources' flux densities are expected to be boosted from both Eddington boosting (Eddington 1913) and confusion boosting. We have estimated the magnitude of these two boosting factors together using our simulation results, which we show as a function of detection S/N in the top panels of Fig. 5. Fig. 5 also shows the median positional offset between the measured output position of a 450 μm – or 850 μm – source and its input position in the bottom panels (a maximum search radius of 7 and 14 arcsec were used, respectively.). The positional uncertainty quoted in Tables 1 and 2 is the 90 per cent confidence interval, which we then use for matching to radio, 24 μm, and optical counterparts as described in Section 3.4. Higher S/N detections can yield very small positional uncertainties.

Before measuring the cumulative number counts or deciding on an appropriate S/N detection threshold, it is essential to understand our sample's completeness and contamination rate. Completeness deteriorates at low flux densities. We estimate completeness from our Monte Carlo simulations as the fraction of sources recovered $>3\sigma$ or $>4\sigma$ in our simulated maps and is shown in Fig. 6. As is expected, a more conservative (4σ) cut on the sample results in a more incomplete sample at moderate flux densities than a more liberal cut (3σ). We will take these completeness curves into consideration with the calculation of the cumulative number counts.

Deciding on an appropriate detection threshold requires an understanding of our sample's contaminants. We measure contamination rate as a function of detection S/N. At a given detection S/N, the contaminating fraction is the number of sources which are generated by fluctuations in the map due to noise or from sources well below the nominal detection limit. Since our maps are roughly uniform, we fix this limiting flux density at the lowest deboosted flux density of our 3σ sample. Any source with input flux density below this threshold would not be expected to be measured in our data even after Eddington and confusion boosting, so here is considered a contaminant. The contamination rate as a function of both flux density and S/N is shown in Fig. 7.

Fig. 7 tells us the probability that a given source with a given S/N is spurious. Accordingly, we are able to assign a 'probability of contamination' ($p_{\rm contam}$) for each source. We use this source-by-source probability to estimate total contamination rates for samples defined by different S/N detection thresholds. In a sample-sized N, the probability of having no contaminants is equal to $\prod_{i=1}^{N}(1-p_i)$, the probability of having one contaminant is equal to

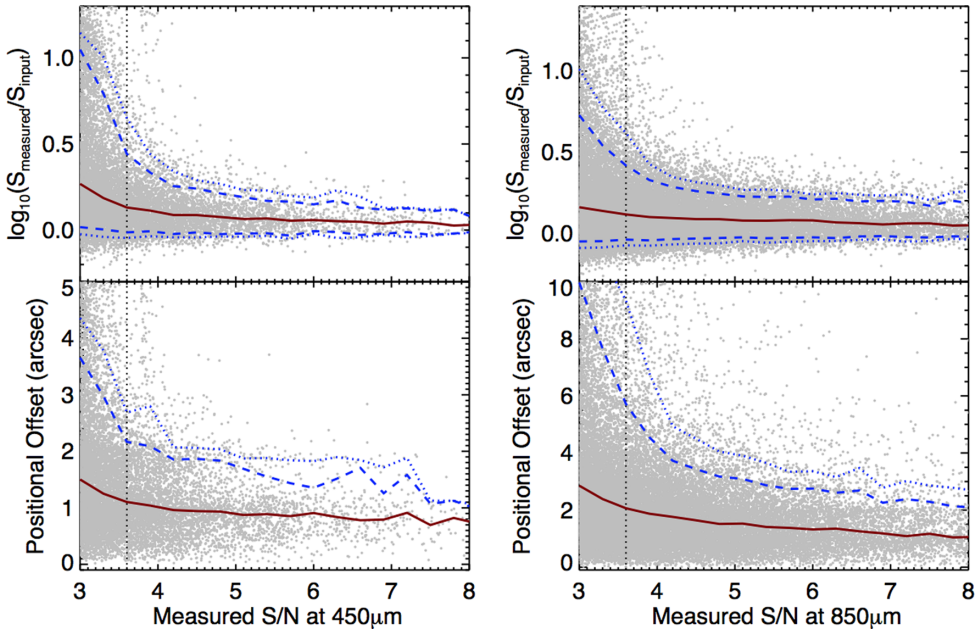

Figure 5. Our results from Monte Carlo simulations, showing more than 10000 source realizations and the measured boosting factor and positional offset for each source (grey points) at 450 μm (left) and 850 μm (right). The boosting factor is measured as the ratio of output measured flux density over input flux density. We deboost our sources' flux densities using the median boosting factors (red lines). The 90 per cent confidence intervals (dashed blue lines) and 95 per cent confidence intervals (dotted blue lines) are overplotted. We assign a positional uncertainty to sources according to the 90 per cent confidence interval. The 3.6σ S/N threshold is marked by dotted vertical lines.

Table 1. 450 μm identified >3.6σ point sources in COSMOS.

Name	Short name	RA_{450}	DEC_{450}	S/N	S_{450} Raw (mJy)	S_{450} Deboosted (mJy)	$\Delta(\alpha,\delta)$ (arcsec)	P_{contam}	850 μm Source	Offset (arcsec)	S_{850} Raw (mJy)	S_{850} Deboosted (mJy)
SMM J100028.6+023201...	450.00	10:00:28.6	02:32:01	7.80	40.58 ± 5.20	37.54 ± 6.58	1.06	<0.01	850.07	0.6	9.94 ± 1.06	9.21 ± 1.45
SMM J100033.3+022559...	450.01	10:00:33.3	02:25:59	6.89	28.43 ± 4.13	25.62 ± 4.96	1.51	<0.01	850.02	0.6	9.47 ± 0.80	8.22 ± 0.70
SMM J100109.0+022255...	450.02	10:01:09.0	02:22:55	6.15	47.20 ± 7.68	41.70 ± 9.00	1.48	<0.01			9.67 ± 1.71	
SMM J100008.0+022611...	450.03	10:00:08.0	02:26:11	5.73	23.47 ± 4.10	20.46 ± 4.78	1.45	<0.01	850.00	0.6	16.15 ± 0.80	10.86 ± 0.54
SMM J100019.7+023205...	450.04	10:00:19.7	02:32:05	5.62	29.15 ± 5.19	25.35 ± 6.04	1.48	<0.01	850.03	1.5	12.11 ± 1.03	10.54 ± 0.90
SMM J100023.6+022156...	450.05	10:00:23.6	02:21:56	5.62	23.14 ± 4.12	20.12 ± 4.80	1.48	<0.01	850.08	1.9	7.19 ± 0.80	6.60 ± 1.12
SMM J100039.2+022221...	450.06	10:00:39.2	02:22:21	5.43	22.29 ± 4.11	19.32 ± 4.76	1.55	<0.01	850.12	1.3	6.49 ± 0.80	5.83 ± 1.13
SMM J100014.2+023017...	450.07	10:00:14.2	02:30:17	5.32	23.94 ± 4.50	20.65 ± 5.19	1.59	<0.01			2.64 ± 0.89	
SMM J100025.1+021508...	450.08	10:00:25.1	02:15:08	5.15	31.25 ± 6.06	26.71 ± 6.93	1.67	<0.01	(850.46)		4.27 ± 1.15	
SMM J100016.6+022637...	450.09	10:00:16.6	02:26:37	4.94	20.41 ± 4.14	17.26 ± 4.68	1.75	<0.01	850.34	2.3	4.41 ± 0.80	3.68 ± 1.01
SMM J100022.2+022354...	450.10	10:00:22.2	02:23:54	4.85	20.09 ± 4.14	16.91 ± 4.67	1.78	<0.01	850.135	5.5	2.60 ± 0.80	1.87 ± 1.01
SMM J100025.4+022542...	450.11	10:00:25.4	02:25:42	4.77	19.57 ± 4.11	16.40 ± 4.62	1.80	<0.01	850.41	2.0	4.12 ± 0.80	3.43 ± 0.98
SMM J095957.0+022153...	450.12	09:59:57.0	02:21:53	4.76	22.03 ± 4.63	18.45 ± 5.21	1.81	<0.01			1.71 ± 0.89	
SMM J100001.7+022426...	450.13	10:00:01.7	02:24:26	4.75	19.96 ± 4.20	16.72 ± 4.73	1.81	<0.01	(850.32)		3.81 ± 0.82	
SMM J100044.9+021919...	450.14	10:00:44.9	02:19:19	4.74	21.73 ± 4.59	18.18 ± 5.17	1.81	<0.01			1.28 ± 0.91	
SMM J100004.2+022059...	450.15	10:00:04.2	02:20:59	4.60	19.92 ± 4.33	16.53 ± 4.88	1.83	<0.01	850.28	1.8	4.86 ± 0.84	4.07 ± 1.08
SMM J100057.2+022009...	450.16	10:00:57.2	02:20:09	4.59	25.18 ± 5.48	20.89 ± 6.19	1.84	<0.01	(850.05)		8.99 ± 1.14	
SMM J100017.2+022521...	450.17	10:00:17.2	02:25:21	4.59	19.01 ± 4.14	15.76 ± 4.67	1.84	<0.01	850.42	2.6	4.12 ± 0.80	3.43 ± 0.99
SMM J100007.2+021803...	450.18	10:00:07.2	02:18:03	4.49	22.63 ± 5.04	18.66 ± 5.68	1.85	<0.01			-0.76 ± 0.95	
SMM J095948.1+022014...	450.19	09:59:48.1	02:20:14	4.47	28.25 ± 6.33	23.24 ± 7.14	1.86	<0.01			0.77 ± 1.16	
SMM J100004.5+023042...	450.20	10:00:04.5	02:30:42	4.44	23.28 ± 5.24	19.11 ± 5.91	1.87	<0.01	(850.24)		4.62 ± 1.01	
SMM J100017.2+022138...	450.21	10:00:17.2	02:21:38	4.40	18.14 ± 4.12	14.83 ± 4.64	1.88	<0.01			0.72 ± 0.80	
SMM J100030.8+023104...	450.22	10:00:30.8	02:31:04	4.34	21.10 ± 4.86	17.15 ± 5.47	1.90	<0.01	850.149	4.1	3.04 ± 0.96	2.16 ± 1.21
SMM J100004.6+021820...	450.23	10:00:04.6	02:18:20	4.33	21.95 ± 5.07	17.81 ± 5.71	1.90	<0.01			-0.36 ± 0.96	
SMM J100050.1+022116...	450.24	10:00:50.1	02:21:16	4.30	19.72 ± 4.58	15.97 ± 5.16	1.91	<0.01			1.29 ± 0.91	
SMM J100028.5+021927...	450.25	10:00:28.5	02:19:27	4.30	18.04 ± 4.20	14.60 ± 4.73	1.91	<0.01			-0.82 ± 0.82	
SMM J100016.6+022000...	450.26	10:00:16.6	02:20:00	4.27	17.81 ± 4.17	14.38 ± 4.69	1.92	<0.01			-0.60 ± 0.81	
SMM J095942.9+022144...	450.27	09:59:42.9	02:21:44	4.26	29.66 ± 6.97	23.91 ± 7.84	1.92	<0.01	850.115	7.3	4.26 ± 1.26	3.14 ± 1.56
SMM J100056.7+022014...	450.28	10:00:56.7	02:20:14	4.24	22.76 ± 5.37	18.32 ± 6.04	1.93	<0.01	(850.05)		10.85 ± 1.12	
SMM J100000.5+022503...	450.29	10:00:00.5	02:25:03	4.22	18.01 ± 4.27	14.46 ± 4.80	1.93	<0.01			0.94 ± 0.83	
SMM J100048.3+022926...	450.30	10:00:48.3	02:29:26	4.16	20.99 ± 5.05	16.76 ± 5.69	1.95	<0.01			2.23 ± 1.04	
SMM J100008.4+022241...	450.31	10:00:08.4	02:22:41	4.11	16.96 ± 4.13	13.46 ± 4.69	1.97	0.02			1.17 ± 0.80	
SMM J100010.2+022624...	450.32	10:00:10.2	02:26:24	4.10	16.86 ± 4.11	13.37 ± 4.67	1.97	0.02	850.26	3.0	4.87 ± 0.80	4.12 ± 1.06
SMM J100021.3+023055...	450.33	10:00:21.3	02:30:55	4.04	18.93 ± 4.69	14.90 ± 5.36	1.99	0.03			0.59 ± 0.93	
SMM J095945.2+022253...	450.34	09:59:45.2	02:22:53	4.04	24.73 ± 6.13	19.46 ± 7.01	1.99	0.03			3.30 ± 1.13	

Table 1 – *continued*

Name	Short name	RA_{450}	DEC_{450}	S/N	S_{450} Raw (mJy)	S_{450} Deboosted (mJy)	$\Delta(\alpha,\delta)$ (arcsec)	P_{contam}	850 μm Source	Offset (arcsec)	S_{850} Raw (mJy)	S_{850} Deboosted (mJy)
SMM J100014.4+021706...	450.35	10:00:14.4	02:17:06	4.01	20.52 ± 5.12	16.10 ± 5.87	2.00	0.03			−0.55 ± 0.97	
SMM J100101.0+022800...	450.36	10:01:01.0	02:28:00	4.00	24.27 ± 6.07	19.03 ± 6.96	2.00	0.03	850.58	3.8	5.67 ± 1.31	4.60 ± 1.57
SMM J100001.5+021939...	450.37	10:00:01.5	02:19:39	4.00	19.20 ± 4.80	15.05 ± 5.51	2.00	0.03			−0.98 ± 0.91	
SMM J100010.3+022223...	450.38	10:00:10.3	02:22:23	4.00	16.47 ± 4.12	12.91 ± 4.73	2.01	0.03	850.14	2.8	6.25 ± 0.80	5.55 ± 1.11
SMM J100011.2+021554...	450.39	10:00:11.2	02:15:54	3.99	23.76 ± 5.96	18.60 ± 6.84	2.01	0.04			−0.70 ± 1.11	
SMM J100033.1+023046...	450.40	10:00:33.1	02:30:46	3.98	19.15 ± 4.81	14.98 ± 5.53	2.01	0.04	850.90	5.0	3.52 ± 0.96	2.71 ± 1.16
SMM J100006.6+021527...	450.41	10:00:06.6	02:15:27	3.96	26.42 ± 6.67	20.62 ± 7.67	2.02	0.04			1.39 ± 1.25	
SMM J100036.9+021938...	450.42	10:00:36.9	02:19:38	3.94	16.71 ± 4.24	13.01 ± 4.89	2.02	0.04	850.48	3.6	3.99 ± 0.83	3.30 ± 1.00
SMM J100028.8+023336...	450.43	10:00:28.8	02:33:36	3.88	24.62 ± 6.34	19.00 ± 7.36	2.06	0.05			1.62 ± 1.28	
SMM J100054.5+021919...	450.44	10:00:54.5	02:19:19	3.88	20.99 ± 5.41	16.18 ± 6.28	2.06	0.05			−0.15 ± 1.12	
SMM J100056.1+021831...	450.45	10:00:56.1	02:18:31	3.82	23.57 ± 6.16	17.92 ± 7.22	2.13	0.06			−1.21 ± 1.30	
SMM J100032.4+022148...	450.46	10:00:32.4	02:21:48	3.81	15.72 ± 4.13	11.90 ± 4.86	2.16	0.07			0.11 ± 0.80	
SMM J100025.2+021930...	450.47	10:00:25.2	02:19:30	3.80	15.90 ± 4.18	12.03 ± 4.91	2.16	0.07			1.60 ± 0.81	
SMM J100009.4+022223...	450.48	10:00:09.4	02:22:23	3.80	15.72 ± 4.13	11.89 ± 4.86	2.16	0.07			2.73 ± 0.80	
SMM J100000.0+022524...	450.49	10:00:00.0	02:25:24	3.79	16.29 ± 4.30	12.27 ± 5.07	2.18	0.07			−0.72 ± 0.84	
SMM J095952.2+022133...	450.50	09:59:52.2	02:21:33	3.78	19.82 ± 5.25	14.90 ± 6.19	2.19	0.07	850.47	3.6	4.74 ± 0.98	3.92 ± 1.19
SMM J100044.3+022313...	450.51	10:00:44.3	02:23:13	3.77	15.64 ± 4.15	11.74 ± 4.90	2.20	0.08			1.27 ± 0.81	
SMM J100007.8+022306...	450.52	10:00:07.8	02:23:06	3.77	15.57 ± 4.13	11.68 ± 4.88	2.20	0.08			−0.46 ± 0.80	
SMM J100010.4+022026...	450.53	10:00:10.4	02:20:26	3.74	15.69 ± 4.19	11.69 ± 4.97	2.23	0.08	850.109	0.6	2.84 ± 0.82	2.13 ± 1.00
SMM J100026.8+022318...	450.54	10:00:26.8	02:23:18	3.74	15.46 ± 4.13	11.51 ± 4.90	2.23	0.08	850.96	8.1	2.93 ± 0.80	2.24 ± 0.97
SMM J100023.8+021751...	450.55	10:00:23.8	02:17:51	3.74	17.06 ± 4.57	12.70 ± 5.42	2.24	0.08	850.06	3.1	9.30 ± 0.89	8.42 ± 0.92
SMM J095959.3+023000...	450.56	09:59:59.3	02:30:00	3.73	20.17 ± 5.40	14.98 ± 6.42	2.25	0.09			−0.89 ± 1.03	
SMM J100032.4+021802...	450.57	10:00:32.4	02:18:02	3.73	16.75 ± 4.49	12.44 ± 5.34	2.25	0.09			0.56 ± 0.88	
SMM J100036.1+022152...	450.58	10:00:36.1	02:21:52	3.72	15.32 ± 4.12	11.35 ± 4.90	2.26	0.09	850.21	3.6	5.29 ± 0.80	4.60 ± 1.08
SMM J100019.4+022024...	450.59	10:00:19.4	02:20:24	3.71	15.33 ± 4.13	11.33 ± 4.92	2.27	0.09	850.101	3.3	2.87 ± 0.80	2.19 ± 0.98
SMM J100008.1+023059...	450.60	10:00:08.1	02:30:59	3.71	18.82 ± 5.07	13.90 ± 6.04	2.27	0.09			1.81 ± 0.99	
SMM J100018.7+022813...	450.61	10:00:18.7	02:28:13	3.70	15.48 ± 4.18	11.42 ± 4.98	2.28	0.09			1.24 ± 0.81	
SMM J100047.3+022049...	450.62	10:00:47.3	02:20:49	3.70	16.48 ± 4.45	12.15 ± 5.30	2.28	0.09			−0.18 ± 0.89	
SMM J100020.0+022129...	450.63	10:00:20.0	02:21:29	3.70	15.23 ± 4.12	11.23 ± 4.90	2.29	0.09			0.05 ± 0.80	
SMM J100010.7+022707...	450.64	10:00:10.7	02:27:07	3.68	15.18 ± 4.12	11.14 ± 4.91	2.31	0.10			0.86 ± 0.80	
SMM J100027.2+022448...	450.65	10:00:27.2	02:24:48	3.68	15.13 ± 4.12	11.08 ± 4.92	2.32	0.10			0.00 ± 0.80	
SMM J100104.6+022633...	450.66	10:01:04.6	02:26:33	3.66	23.50 ± 6.42	17.15 ± 7.68	2.34	0.10	850.146	4.1	4.29 ± 1.36	3.06 ± 1.70
SMM J100000.3+022902...	450.67	10:00:00.3	02:29:02	3.65	17.79 ± 4.87	12.96 ± 5.83	2.34	0.10			1.08 ± 0.94	
SMM J095945.7+021837...	450.68	09:59:45.7	02:18:37	3.65	28.64 ± 7.84	20.86 ± 9.38	2.35	0.10			−0.56 ± 1.46	
SMM J100047.5+022520...	450.69	10:00:47.5	02:25:20	3.64	15.52 ± 4.26	11.27 ± 5.11	2.36	0.11			0.72 ± 0.84	
SMM J095952.6+022711...	450.70	09:59:52.6	02:27:11	3.64	18.86 ± 5.18	13.68 ± 6.21	2.36	0.11			1.28 ± 0.99	
SMM J095946.3+022931...	450.71	09:59:46.3	02:29:31	3.64	28.16 ± 7.74	20.42 ± 9.28	2.37	0.11			1.44 ± 1.45	
SMM J095950.5+022016...	450.72	09:59:50.5	02:20:16	3.63	21.50 ± 5.92	15.58 ± 7.09	2.37	0.11			0.12 ± 1.09	
SMM J100106.1+022454...	450.73	10:01:06.1	02:24:54	3.63	23.49 ± 6.48	17.00 ± 7.76	2.38	0.11			−1.96 ± 1.39	
SMM J100041.3+021640...	450.74	10:00:41.3	02:16:40	3.61	20.01 ± 5.54	14.44 ± 6.64	2.39	0.11			−0.38 ± 1.10	
SMM J100034.2+023421...	450.75	10:00:34.2	02:34:21	3.61	28.05 ± 7.76	20.23 ± 9.31	2.39	0.11			−1.80 ± 1.55	
SMM J100021.7+023114...	450.76	10:00:21.7	02:31:14	3.61	17.34 ± 4.80	12.50 ± 5.76	2.39	0.11			0.64 ± 0.95	
SMM J095952.6+022258...	450.77	09:59:52.6	02:22:58	3.61	17.85 ± 4.95	12.85 ± 5.94	2.40	0.11			0.11 ± 0.95	

Notes. The $>3.6\sigma$ 450 μm detected sources we extract within the central 394 arcmin^2 of our COSMOS map. The 3.6σ detection threshold is chosen based on an estimated 3–5 per cent contamination rate. The list is ordered by detection S/N. The '*Raw*' flux densities are those measured directly from our map. The 'DEBOOSTED' flux densities are those given after correction for confusion and Eddington boosting as a function of detection S/N, as described in Section 3.1. We also measure a 90 per cent confidence interval for positional uncertainties and estimated probability of contamination, P_{contam}, from the results of our Monte Carlo tests as functions of detection S/N. The last four columns contain details on the corresponding 850 μm counterparts if they exist (their short name, offset from 450 μm position, raw and deboosted flux densities). If a 450 μm source is not detected at 850 μm at $>3\sigma$ then the flux density is measured at the 450 μm position. Also see Table 2 for more details on 850 μm sources.

Table 2. 850 μm identified $>3.6\sigma$ point sources in COSMOS.

Name	Short name	RA_{850}	DEC_{850}	S/N	S_{850} Raw (mJy)	S_{850} Deboosted (mJy)	$\Delta(\alpha,\delta)$ (arcsec)	P_{contam}	450 μm Source	Offset (arcsec)	S_{450} Raw (mJy)	S_{450} Deboosted (mJy)
SMM J100008.0+022612...	850.00	10:00:08.0	02:26:12	20.1	16.15 ± 0.80	16.15 ± 0.80	1.19	<0.01	450.03	0.6	23.47 ± 4.10	20.46 ± 4.78
SMM J095957.3+022730...	850.01	09:59:57.3	02:27:30	13.0	11.98 ± 0.92	11.49 ± 1.10	1.65	<0.01	(450.168)		11.02 ± 4.75	
SMM J100033.3+022559...	850.02	10:00:33.3	02:25:59	11.8	9.47 ± 0.80	8.97 ± 1.04	1.78	<0.01	450.01	0.6	28.43 ± 4.13	25.62 ± 4.96
SMM J100019.7+023204...	850.03	10:00:19.7	02:32:04	11.7	12.11 ± 1.03	11.42 ± 1.38	1.77	<0.01	450.04	1.5	29.15 ± 5.19	25.35 ± 6.04
SMM J100015.5+021550...	850.04	10:00:15.5	02:15:50	10.8	11.80 ± 1.08	11.09 ± 1.56	1.85	<0.01			10.67 ± 5.79	
SMM J100057.0+022014...	850.05	10:00:57.0	02:20:14	10.8	12.24 ± 1.13	11.49 ± 1.62	1.85	<0.01	(450.28)		18.48 ± 5.43	
SMM J100024.0+021750...	850.06	10:00:24.0	02:17:50	10.4	9.30 ± 0.89	8.64 ± 1.24	1.88	<0.01	450.55	3.1	17.06 ± 4.57	12.70 ± 5.42
SMM J100028.6+023202...	850.07	10:00:28.6	02:32:02	9.41	9.94 ± 1.06	9.21 ± 1.45	2.18	<0.01	450.00	0.6	40.58 ± 5.20	37.54 ± 6.58
SMM J100023.5+022155...	850.08	10:00:23.5	02:21:55	8.98	7.19 ± 0.80	6.60 ± 1.12	2.10	<0.01	450.05	1.9	23.14 ± 4.12	20.12 ± 4.80
SMM J100025.3+021847...	850.09	10:00:25.3	02:18:47	8.89	7.47 ± 0.84	6.83 ± 1.17	2.10	<0.01	450.87	2.8	15.24 ± 4.30	10.74 ± 5.24

Table 2 – *continued*

Name	Short name	RA_{850}	DEC_{850}	S/N	S_{850} Raw (mJy)	S_{850} Deboosted (mJy)	$\Delta(\alpha,\delta)$ (arcsec)	P_{contam}	450 μm Source	Offset (arcsec)	S_{450} Raw (mJy)	S_{450} Deboosted (mJy)
SMM J100034.4+022121...	850.10	10:00:34.4	02:21:21	8.61	6.90 ± 0.80	6.24 ± 1.13	2.12	<0.01	450.81	0.8	14.71 ± 4.11	10.47 ± 4.98
SMM J100049.9+022257...	850.11	10:00:49.9	02:22:57	8.59	7.51 ± 0.87	6.79 ± 1.24	2.12	<0.01			5.94 ± 4.41	
SMM J100039.1+022221...	850.12	10:00:39.1	02:22:21	8.14	6.49 ± 0.80	5.83 ± 1.13	2.10	<0.01	450.06	1.3	22.29 ± 4.11	19.32 ± 4.76
SMM J100024.1+022005...	850.13	10:00:24.1	02:20:05	8.00	6.44 ± 0.80	5.76 ± 1.13	2.12	<0.01			8.53 ± 4.13	
SMM J100010.2+022221...	850.14	10:00:10.2	02:22:21	7.81	6.25 ± 0.80	5.55 ± 1.11	2.17	<0.01	450.38	2.8	16.47 ± 4.12	12.91 ± 4.73
SMM J100025.2+022607...	850.15	10:00:25.2	02:26:07	7.26	5.79 ± 0.80	5.08 ± 1.09	2.30	<0.01			11.51 ± 4.11	
SMM J100103.9+022447...	850.16	10:01:03.9	02:24:47	7.12	8.94 ± 1.25	7.82 ± 1.71	2.34	<0.01			14.52 ± 5.92	
SMM J100000.4+022256...	850.17	10:00:00.4	02:22:56	7.01	5.88 ± 0.84	5.14 ± 1.14	2.39	<0.01			8.96 ± 4.28	
SMM J100024.0+022947...	850.18	10:00:24.0	02:29:47	6.85	5.87 ± 0.86	5.13 ± 1.16	2.45	<0.01			6.37 ± 4.36	
SMM J100015.7+022445...	850.19	10:00:15.7	02:24:45	6.74	5.40 ± 0.80	4.71 ± 1.08	2.48	<0.01			2.13 ± 4.13	
SMM J100027.0+023137...	850.20	10:00:27.0	02:31:37	6.64	6.69 ± 1.01	5.83 ± 1.36	2.51	<0.01			3.93 ± 5.00	
SMM J100035.9+022151...	850.21	10:00:35.9	02:21:51	6.60	5.29 ± 0.80	4.60 ± 1.08	2.52	<0.01	450.58	3.6	15.32 ± 4.12	11.35 ± 4.90
SMM J100018.7+021655...	850.22	10:00:18.7	02:16:55	6.25	6.05 ± 0.97	5.15 ± 1.28	2.69	<0.01			10.34 ± 5.10	
SMM J100022.1+022842...	850.23	10:00:22.1	02:28:42	6.25	5.06 ± 0.81	4.31 ± 1.07	2.69	<0.01	450.94	0.6	14.67 ± 4.19	10.14 ± 5.17
SMM J100004.8+023045...	850.24	10:00:04.8	02:30:45	6.20	6.26 ± 1.01	5.32 ± 1.34	2.69	<0.01	(450.20)		11.37 ± 5.23	
SMM J100012.5+021444...	850.25	10:00:12.5	02:14:44	6.15	7.93 ± 1.29	6.72 ± 1.70	2.69	<0.01			14.85 ± 6.90	
SMM J100010.3+022627...	850.26	10:00:10.3	02:26:27	6.09	4.87 ± 0.80	4.12 ± 1.06	2.69	<0.01	450.32	3.0	16.86 ± 4.11	13.37 ± 4.67
SMM J100023.5+021918...	850.27	10:00:23.5	02:19:18	6.09	5.00 ± 0.82	4.23 ± 1.08	2.69	<0.01	450.215	2.7	13.05 ± 4.20	7.48 ± 5.28
SMM J100004.3+022059...	850.28	10:00:04.3	02:20:59	5.79	4.86 ± 0.84	4.07 ± 1.08	2.76	<0.01	450.15	1.8	19.92 ± 4.33	16.53 ± 4.88
SMM J100050.1+022615...	850.29	10:00:50.1	02:26:15	5.70	5.13 ± 0.90	4.28 ± 1.15	2.79	<0.01			10.89 ± 4.50	
SMM J100006.7+022209...	850.30	10:00:06.7	02:22:09	5.69	4.58 ± 0.80	3.82 ± 1.03	2.79	<0.01			3.90 ± 4.15	
SMM J100026.1+021741...	850.31	10:00:26.1	02:17:41	5.57	5.02 ± 0.90	4.19 ± 1.14	2.84	<0.01			12.34 ± 4.62	
SMM J100001.5+022429...	850.32	10:00:01.5	02:24:29	5.56	4.56 ± 0.82	3.81 ± 1.04	2.84	<0.01	(450.13)		13.33 ± 4.20	
SMM J095950.7+022827...	850.33	09:59:50.7	02:28:27	5.55	6.20 ± 1.12	5.18 ± 1.41	2.85	<0.01	450.99	3.7	20.15 ± 5.80	13.76 ± 7.20
SMM J100016.4+022638...	850.34	10:00:16.4	02:26:38	5.49	4.41 ± 0.80	3.68 ± 1.01	2.86	<0.01	450.09	2.3	20.41 ± 4.14	17.26 ± 4.68
SMM J100105.1+022150...	850.35	10:01:05.1	02:21:50	5.47	7.60 ± 1.39	6.35 ± 1.74	2.87	<0.01			0.38 ± 6.54	
SMM J100001.3+021745...	850.36	10:00:01.3	02:17:45	5.39	5.60 ± 1.04	4.68 ± 1.30	2.90	<0.01			0.09 ± 5.62	
SMM J100035.6+022826...	850.37	10:00:35.6	02:28:26	5.38	4.45 ± 0.83	3.72 ± 1.03	2.91	<0.01			1.74 ± 4.25	
SMM J100023.5+021536...	850.38	10:00:23.5	02:15:36	5.22	5.67 ± 1.09	4.72 ± 1.34	2.99	<0.01			13.39 ± 5.74	
SMM J100012.1+022310...	850.39	10:00:12.1	02:23:10	5.21	4.17 ± 0.80	3.47 ± 0.99	2.99	<0.01			10.53 ± 4.13	
SMM J100013.5+022227...	850.40	10:00:13.5	02:22:27	5.20	4.16 ± 0.80	3.47 ± 0.99	3.00	<0.01	450.252	3.7	12.57 ± 4.14	6.91 ± 5.15
SMM J100025.4+022544...	850.41	10:00:25.4	02:25:44	5.17	4.12 ± 0.80	3.43 ± 0.98	3.01	<0.01	450.11	2.0	19.57 ± 4.11	16.40 ± 4.62
SMM J100017.2+022519...	850.42	10:00:17.2	02:25:19	5.14	4.12 ± 0.80	3.43 ± 0.99	3.02	<0.01	450.17	2.6	19.01 ± 4.14	15.76 ± 4.67
SMM J100026.3+021528...	850.43	10:00:26.3	02:15:28	5.02	5.55 ± 1.11	4.60 ± 1.35	3.10	<0.01			2.32 ± 5.82	
SMM J100018.2+022249...	850.44	10:00:18.2	02:22:49	5.00	3.99 ± 0.80	3.31 ± 0.97	3.10	<0.01			3.93 ± 4.12	
SMM J100006.9+022047...	850.45	10:00:06.9	02:20:47	4.99	4.12 ± 0.83	3.42 ± 1.01	3.11	<0.01			3.79 ± 4.25	
SMM J100025.4+021506...	850.46	10:00:25.4	02:15:06	4.85	5.62 ± 1.16	4.64 ± 1.40	3.20	<0.01	(450.08)		21.40 ± 6.11	
SMM J095952.3+022137...	850.47	09:59:52.3	02:21:37	4.83	4.74 ± 0.98	3.92 ± 1.19	3.21	<0.01	450.50	3.6	19.82 ± 5.25	14.90 ± 6.19
SMM J100037.0+021942...	850.48	10:00:37.0	02:19:42	4.83	3.99 ± 0.83	3.30 ± 1.00	3.22	<0.01	450.42	3.6	16.71 ± 4.24	13.01 ± 4.89
SMM J100005.0+021719...	850.49	10:00:05.0	02:17:19	4.80	4.91 ± 1.02	4.05 ± 1.24	3.23	<0.01	450.193	0.6	17.40 ± 5.50	10.27 ± 6.95
SMM J100009.1+022023...	850.50	10:00:09.1	02:20:23	4.78	3.94 ± 0.82	3.25 ± 1.00	3.25	<0.01			4.68 ± 4.23	
SMM J095956.4+021854...	850.51	09:59:56.4	02:18:54	4.74	4.94 ± 1.04	4.06 ± 1.26	3.27	<0.01			9.29 ± 5.61	
SMM J100011.9+022937...	850.52	10:00:11.9	02:29:37	4.74	4.09 ± 0.86	3.37 ± 1.04	3.28	<0.01	450.134	1.7	14.45 ± 4.36	9.26 ± 5.50
SMM J100011.4+021508...	850.53	10:00:11.4	02:15:08	4.68	5.72 ± 1.22	4.70 ± 1.47	3.32	<0.01	450.206	4.8	20.69 ± 6.60	12.04 ± 8.32
SMM J095948.9+022748...	850.54	09:59:48.9	02:27:48	4.55	5.10 ± 1.12	4.17 ± 1.35	3.41	<0.01			0.47 ± 5.90	
SMM J095950.9+022742...	850.55	09:59:50.9	02:27:42	4.52	4.77 ± 1.06	3.89 ± 1.27	3.43	<0.01	450.86	3.6	19.80 ± 5.58	13.95 ± 6.80
SMM J100005.1+021526...	850.56	10:00:05.1	02:15:26	4.42	5.69 ± 1.29	4.63 ± 1.54	3.58	0.02			−4.70 ± 6.84	
SMM J100006.8+023307...	850.57	10:00:06.8	02:33:07	4.35	5.94 ± 1.36	4.82 ± 1.63	3.68	0.02			3.66 ± 7.17	
SMM J100101.3+022800...	850.58	10:01:01.3	02:28:00	4.33	5.67 ± 1.31	4.60 ± 1.57	3.71	0.03	450.36	3.8	24.27 ± 6.07	19.03 ± 6.96
SMM J100000.7+022001...	850.59	10:00:00.7	02:20:01	4.32	3.92 ± 0.91	3.18 ± 1.08	3.72	0.03			2.88 ± 4.76	
SMM J100000.7+022740...	850.60	10:00:00.7	02:27:40	4.32	3.79 ± 0.88	3.07 ± 1.05	3.73	0.03			11.26 ± 4.49	
SMM J100002.0+022820...	850.61	10:00:02.0	02:28:20	4.31	3.83 ± 0.89	3.10 ± 1.06	3.73	0.03			11.06 ± 4.53	
SMM J100031.0+022751...	850.62	10:00:31.0	02:27:51	4.29	3.46 ± 0.81	2.80 ± 0.96	3.76	0.03	450.78	0.9	14.94 ± 4.15	10.72 ± 4.99
SMM J095953.3+021850...	850.63	09:59:53.3	02:18:50	4.28	4.77 ± 1.11	3.86 ± 1.33	3.78	0.03			3.99 ± 6.07	
SMM J100000.6+022137...	850.64	10:00:00.6	02:21:37	4.18	3.59 ± 0.86	2.89 ± 1.02	3.95	0.04			4.27 ± 4.41	
SMM J100059.2+022108...	850.65	10:00:59.2	02:21:08	4.15	4.71 ± 1.14	3.79 ± 1.35	4.04	0.04			2.93 ± 5.46	
SMM J100024.4+022831...	850.66	10:00:24.4	02:28:31	4.09	3.30 ± 0.81	2.64 ± 0.96	4.19	0.05			8.36 ± 4.17	
SMM J100032.4+023321...	850.67	10:00:32.4	02:33:21	4.08	5.15 ± 1.26	4.12 ± 1.50	4.21	0.05	450.240	5.9	19.01 ± 6.21	10.61 ± 7.75
SMM J095955.3+021954...	850.68	09:59:55.3	02:19:54	4.06	4.05 ± 1.00	3.24 ± 1.19	4.27	0.05			11.46 ± 5.35	
SMM J100043.8+022857...	850.69	10:00:43.8	02:28:57	4.03	3.74 ± 0.93	2.98 ± 1.10	4.34	0.06			−2.18 ± 4.64	
SMM J100020.0+023020...	850.70	10:00:20.0	02:30:20	4.02	3.57 ± 0.89	2.85 ± 1.06	4.36	0.06			6.36 ± 4.49	
SMM J095944.0+022105...	850.71	09:59:44.0	02:21:05	4.01	5.07 ± 1.26	4.04 ± 1.50	4.38	0.06			6.21 ± 6.92	
SMM J100013.6+021731...	850.72	10:00:13.6	02:17:31	3.99	3.77 ± 0.95	3.00 ± 1.13	4.45	0.06			3.00 ± 4.96	
SMM J100020.6+022251...	850.73	10:00:20.6	02:22:51	3.89	3.11 ± 0.80	2.46 ± 0.95	4.69	0.07			−0.35 ± 4.11	
SMM J100005.5+021448...	850.74	10:00:05.5	02:14:48	3.88	5.50 ± 1.42	4.33 ± 1.69	4.77	0.08			−1.85 ± 7.61	
SMM J100026.7+022230...	850.75	10:00:26.7	02:22:30	3.83	3.08 ± 0.80	2.41 ± 0.96	4.95	0.09			1.12 ± 4.14	
SMM J100048.9+023023...	850.76	10:00:48.9	02:30:23	3.83	4.36 ± 1.14	3.42 ± 1.36	4.95	0.09			5.52 ± 5.43	
SMM J100005.5+022958...	850.77	10:00:05.5	02:29:58	3.83	3.58 ± 0.94	2.81 ± 1.12	4.97	0.09			0.41 ± 4.78	
SMM J100008.7+021912...	850.78	10:00:08.7	02:19:12	3.82	3.33 ± 0.87	2.60 ± 1.04	5.00	0.09			7.53 ± 4.52	
SMM J100102.2+022234...	850.79	10:01:02.2	02:22:34	3.82	4.57 ± 1.20	3.57 ± 1.43	5.04	0.10			16.35 ± 5.70	

Table 2 – *continued*

Name	Short name	RA_{850}	DEC_{850}	S/N	S_{850} Raw (mJy)	S_{850} Deboosted (mJy)	$\Delta(\alpha,\delta)$ (arcsec)	P_{contam}	450 μm Source	Offset (arcsec)	S_{450} Raw (mJy)	S_{450} Deboosted (mJy)
SMM J100014.1+022704...	850.80	10:00:14.1	02:27:04	3.81	3.06 ± 0.80	2.39 ± 0.96	5.06	0.10			0.71 ± 4.13	<12.40
SMM J095959.0+022441...	850.81	09:59:59.0	02:24:41	3.80	3.21 ± 0.84	2.51 ± 1.01	5.10	0.10			−1.34 ± 4.32	<12.97
SMM J100054.8+021945...	850.82	10:00:54.8	02:19:45	3.78	4.14 ± 1.09	3.22 ± 1.32	5.20	0.11			7.10 ± 5.30	<15.91
SMM J100010.2+021759...	850.83	10:00:10.2	02:17:59	3.77	3.52 ± 0.93	2.74 ± 1.12	5.22	0.11	450.166	1.8	15.87 ± 4.90	9.79 ± 6.20
SMM J100041.8+022111...	850.84	10:00:41.8	02:21:11	3.75	3.07 ± 0.82	2.39 ± 0.99	5.32	0.11			8.93 ± 4.19	<12.57
SMM J100025.0+022753...	850.85	10:00:25.0	02:27:53	3.73	2.99 ± 0.80	2.32 ± 0.97	5.40	0.12	450.105	4.5	14.24 ± 4.14	9.60 ± 5.16
SMM J100101.3+022439...	850.86	10:01:01.3	02:24:39	3.73	4.23 ± 1.13	3.28 ± 1.37	5.41	0.12			−0.42 ± 5.41	<16.22
SMM J100040.3+021758...	850.87	10:00:40.3	02:17:58	3.70	3.49 ± 0.94	2.70 ± 1.14	5.55	0.13			4.66 ± 4.74	<14.22
SMM J100022.2+023026...	850.88	10:00:22.2	02:30:26	3.70	3.31 ± 0.90	2.56 ± 1.08	5.56	0.13	450.179	6.8	14.51 ± 4.52	8.80 ± 5.73
SMM J100020.2+021727...	850.89	10:00:20.2	02:17:27	3.69	3.41 ± 0.92	2.63 ± 1.11	5.60	0.13			10.84 ± 4.77	<14.32
SMM J100032.8+023049...	850.90	10:00:32.8	02:30:49	3.68	3.52 ± 0.96	2.71 ± 1.16	5.64	0.13	450.40	5.0	19.15 ± 4.81	14.98 ± 5.53
SMM J100027.8+022554...	850.91	10:00:27.8	02:25:54	3.67	2.93 ± 0.80	2.26 ± 0.96	5.66	0.13			6.82 ± 4.10	<12.30
SMM J100041.8+022404...	850.92	10:00:41.8	02:24:04	3.67	2.94 ± 0.80	2.27 ± 0.97	5.66	0.13	450.106	5.6	14.19 ± 4.13	9.57 ± 5.15
SMM J100056.7+022945...	850.93	10:00:56.7	02:29:45	3.67	4.80 ± 1.31	3.69 ± 1.58	5.68	0.14			2.09 ± 6.13	<18.38
SMM J100002.6+021632...	850.94	10:00:02.6	02:16:32	3.65	4.21 ± 1.15	3.23 ± 1.39	5.77	0.14			−1.62 ± 6.22	<18.67
SMM J095959.9+022705...	850.95	09:59:59.9	02:27:05	3.65	3.18 ± 0.87	2.44 ± 1.05	5.77	0.14			6.96 ± 4.46	<13.38
SMM J100026.4+022315...	850.96	10:00:26.4	02:23:15	3.64	2.93 ± 0.80	2.24 ± 0.97	5.81	0.14	450.54	8.1	15.46 ± 4.13	11.51 ± 4.90
SMM J100013.4+021807...	850.97	10:00:13.4	02:18:07	3.61	3.27 ± 0.90	2.50 ± 1.09	5.91	0.15			5.64 ± 4.69	<14.08
SMM J100014.5+023008...	850.98	10:00:14.5	02:30:08	3.61	3.18 ± 0.88	2.43 ± 1.07	5.95	0.15			−6.89 ± 4.43	<13.30

Notes. The >3.6σ 850 μm detected sources we extract within the central 394 arcmin^2 of our COSMOS map. The 3.6σ detection threshold is chosen based on an estimated 3–5 per cent contamination rate. The list is ordered by detection S/N. The '*Raw*' flux densities are those measured directly from our map. The 'DEBOOSTED' flux densities are those given after correction for confusion and Eddington boosting as a function of detection S/N, as described in Section 3.1. We also measure a 90 per cent confidence interval for positional uncertainties and estimated probability of contamination, P_{contam}, from the results of our Monte Carlo tests as functions of detection S/N. The last four columns give details on the corresponding 450 μm counterparts, similar to the 850 μm counterparts for 450 μm sources given in Table 1.

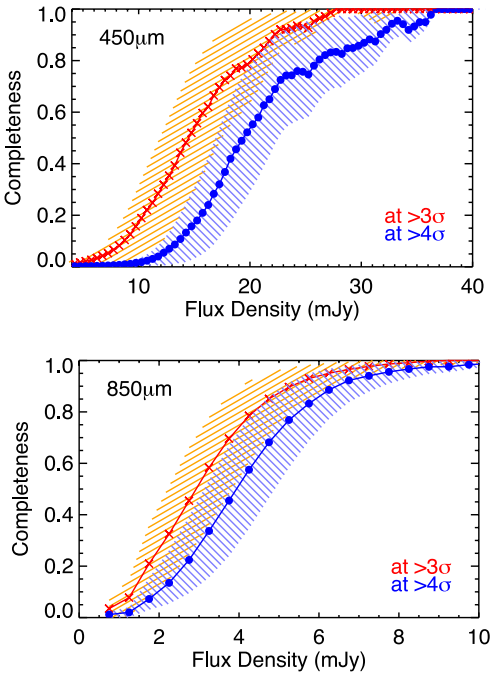

Figure 6. The completeness curves at 450 μm and 850 μm. Completeness is measured as a function of input flux density as the number of sources in a given flux bin which are recovered at the S/N threshold (3σ and 4σ are plotted here). The uncertainty on the completeness curve is generated from a bimodal uncertainty.

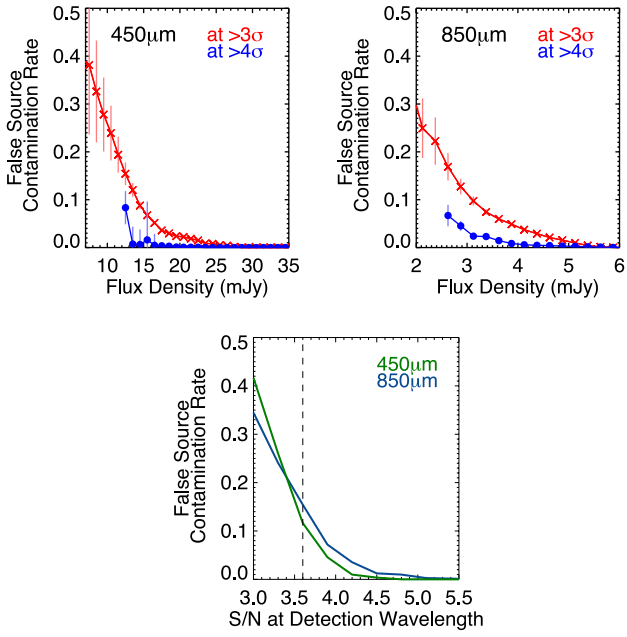

Figure 7. The contamination rates at 450 μm and 850 μm as a function of flux density (top two panels) and S/N (bottom panel). The contamination rate is computed as the number of sources which are extracted from Monte Carlo simulations which are (a) truly spurious, caused by noise fluctuations, or (b) at flux densities lower than the nominal 3σ detection limit, after correction for deboosting. The sharp upturn in contamination at ∼12 mJy at 450 μm is due to small number counts in our simulations (despite >10K realizations, there are very few >4σ sources at ∼12 mJy). We use the measured contamination rate curves in the bottom panel, as a function of S/N, to infer the likelihood that a source of a given S/N is a contaminant. We plot our final S/N threshold of 3.6σ on the bottom panel, which shows that the maximum individual source contamination likelihood is ∼15 per cent in both 450 μm (green) and 850 μm (blue) samples.

$\sum_{i=1}^{N} p_i \prod_{k\neq i}^{N}(1-p_k)$, and so on. For example, there are 37 sources in a 4σ cut in our 450 μm map. We estimate that the 4σ sample has a 76 per cent likelihood of having *no* contaminants, and a 97 per cent chance of having a contamination rate of <3 per cent. This cut is

quite conservative, so we push the detection threshold lower until we estimate contamination rates of 3–5 per cent. This is our target contamination rate since it is low enough not to significantly impact the global properties of the sample, while it allows for a far larger sample size strengthening the analysis of the population. At both 450 μm and 850 μm, we estimate that a 3.6σ detection threshold will yield a 3–5 per cent contamination rate. As is seen in Fig. 7, these limits correspond to similar 'worst' individual source contamination rates of ∼0.14 at 450 μm and ∼0.17 at 850 μm (i.e. the lowest S/N sources in the 3.6σ samples have a ≈14 or 17 per cent likelihood of being spurious.).

3.2 Number counts

We calculate the cumulative number counts (as has been done at different wavelengths in the literature: Barger et al. 1999; Cowie, Barger & Kneib 2002; Scott et al. 2002; Smail et al. 2002; Borys et al. 2003; Webb et al. 2003; Barnard et al. 2004; Coppin et al. 2006; Knudsen et al. 2008; Oliver et al. 2010; Chen et al. 2013) for our sample in three stages and plot the results in Fig. 8. The first is straightforward, as it is the cumulative number counts of the raw flux densities measured from our maps above >3.6σ at 450 μm and above >3.6σ at 850 μm (first panel in Fig. 8, labelled '*raw*'). The second calculation incorporates the correction for flux boosting, as shown in Fig. 5. Here we correct the flux density of each individual source according to its detection S/N. The uncertainty in the deboosting factor is propagated to the new uncertainty in the sources' deboosted flux density. As a result, the sources' ratio of deboosted flux density to its uncertainty is lower than the sources' measured S/N. The net effect of deboosting is a shift towards lower flux densities (in the x-direction on the number counts plot), seen in the middle panels of Fig. 8.

The final effect which needs to be accounted for in our computation of the cumulative number counts is incompleteness and contamination in our samples. As shown in Figs 6 and 7, our samples are not complete down to our nominal ∼15 mJy ≈3.6σ_{450} or ∼2.9 mJy ≈3.6σ_{850} detection threshold. Furthermore, 3–5 per cent of our sources are likely contaminants. To correct for sources missing and contaminant sources we construct a correction factor, c_i, for each source, based on its flux density and S/N, such that $c_i = (1 - f_{\rm contam})/f_{\rm complete}$. We correct the number counts accordingly. Not surprisingly, this correction for incompleteness and contamination has an effect on the low flux density bins and a minimal effect on the high flux density bins. Our deboosted and corrected number counts are given in Table 3.

In functional form, we can assume that the differential number counts follow a few different forms. The types we adopt in this paper are a broken double power law (as most recently used in Chen et al. 2013), taking the form:

$$\frac{{\rm d}N}{{\rm d}S} = \begin{cases} \frac{N_0}{S_0}\left(\frac{S}{S_0}\right)^{-\alpha} & : S \leq S_0 \\ \frac{N_0}{S_0}\left(\frac{S}{S_0}\right)^{-\beta} & : S > S_0 \end{cases} \quad (1)$$

where S_0 represents the turnover flux density, N_0 a normalization for the function in source density per mJy, α is the faint end slope and β is the bright end slope (presumed to be steeper). Alternatively we can assume the number counts follow a Schechter function, as used in Geach et al. (2013):[2]

$$\frac{{\rm d}N}{{\rm d}S} = \frac{N_0}{S_0}\left(\frac{S}{S_0}\right)^{-\alpha} e^{-\left(\frac{S}{S_0}\right)}. \quad (2)$$

We perform a χ^2 optimization to determine best-fitting parameter values at 450 μm and 850 μm, respectively, in equations (1) and (2), which are given in Table 3. These best-fitting parameter values are tested for consistency with the Monte Carlo simulations; in other words, we adjust the fit parameters, populate the jackknife maps accordingly, then extract sources and re-measure the raw number counts. The parameters which reproduce the raw number counts most accurately are used in the Monte Carlo tests for boosting factor, positional uncertainty and estimating contamination and completeness rates, as given in the previous section. Once we arrive at the *corrected* number counts, we then remeasure our best-fitting parameters with a χ^2 test which agrees with our initial injected counts within uncertainty. We find the power-law fit produces a better fit than a Schechter fit to both data sets (with marginally better reduced χ^2, 7 versus 12 at 450 μm and 3 versus 5 at 850 μm), so we use the double power-law Monte Carlo predictions throughout.

Noting a deficit in our 850 μm number counts relative to many literature measurements (Cowie et al. 2002; Scott et al. 2002; Smail et al. 2002; Borys et al. 2003; Webb et al. 2003; Knudsen et al. 2008; Chen et al. 2013), we investigate the strength of this deficit. To do this we compare our best-fitting double power-law function to the Knudsen et al. double power law, integrated over the flux density range where our survey is sensitive (2.5–18 mJy). This comparison indicates that our survey is $2.1^{+1.0}_{-0.6}$ times less dense than the nominal 850 μm source density. We also test to see if the deficit exists at 450 μm, but we find our 450 μm source density is consistent with the only other independent measurement at this wavelength from Chen et al. (2013).

3.3 Source lists

The 450 μm sources detected >3.6σ are summarized in Table 1 and the 850 μm sources detected at >3.6σ are summarized in Table 2 (given at the end of the paper due to its length). Both raw and deboosted flux densities are given in the tables, along with a 90 per cent confidence interval on positional uncertainty, $\Delta(\alpha, \delta)$, the probability of contamination or spuriousness for that source ($P_{\rm contam}$), and the corresponding source detected at the opposite wavelength if it exists. The search for counterparts at the opposite wavelength is done within a radius corresponding to the sum in quadrature of the positional uncertainties, $\Delta(\alpha, \delta)$, at both 450 μm and 850 μm (a function of the detection S/N for each source). If no counterpart is found, the measured flux density at the opposite wavelength is extracted at the detected source's position and quoted as a 3σ upper limit. Its flux density is not deboosted.

Of the 78 450 μm sources, 19 have 850 μm counterparts detected above 3.6σ (a further six sources are detected at 850 μm above 3σ, and five others are close (<12 arcsec) but not formally matched). Such a low fraction of 450 μm corresponding to 850 μm sources ($\lesssim$(19–30)/78 ≈ 24–38 per cent) suggests that indeed, the 450 μm

[2] Note that equation (1) of Geach et al. should be written as ${\rm d}N/{\rm d}S = (N'/S')(S/S')^{1-\alpha}\exp(-S/S')$, and the best-fitting parameter N' from their paper should be quoted as $N' = 4900 \pm 1040\,{\rm deg}^{-2}\,{\rm mJy}^{-1}$ rather than $N' = 490 \pm 104\,{\rm deg}^{-2}$. Also note we use an exponent of $-\alpha$ instead of $1 - \alpha$. By our equation, the parameters of the Geach et al. data are: $N_0 = 4900\,{\rm deg}^{-2}\,{\rm mJy}^{-1}$, $S_0 = 10$ mJy and $\alpha = 2.0$.

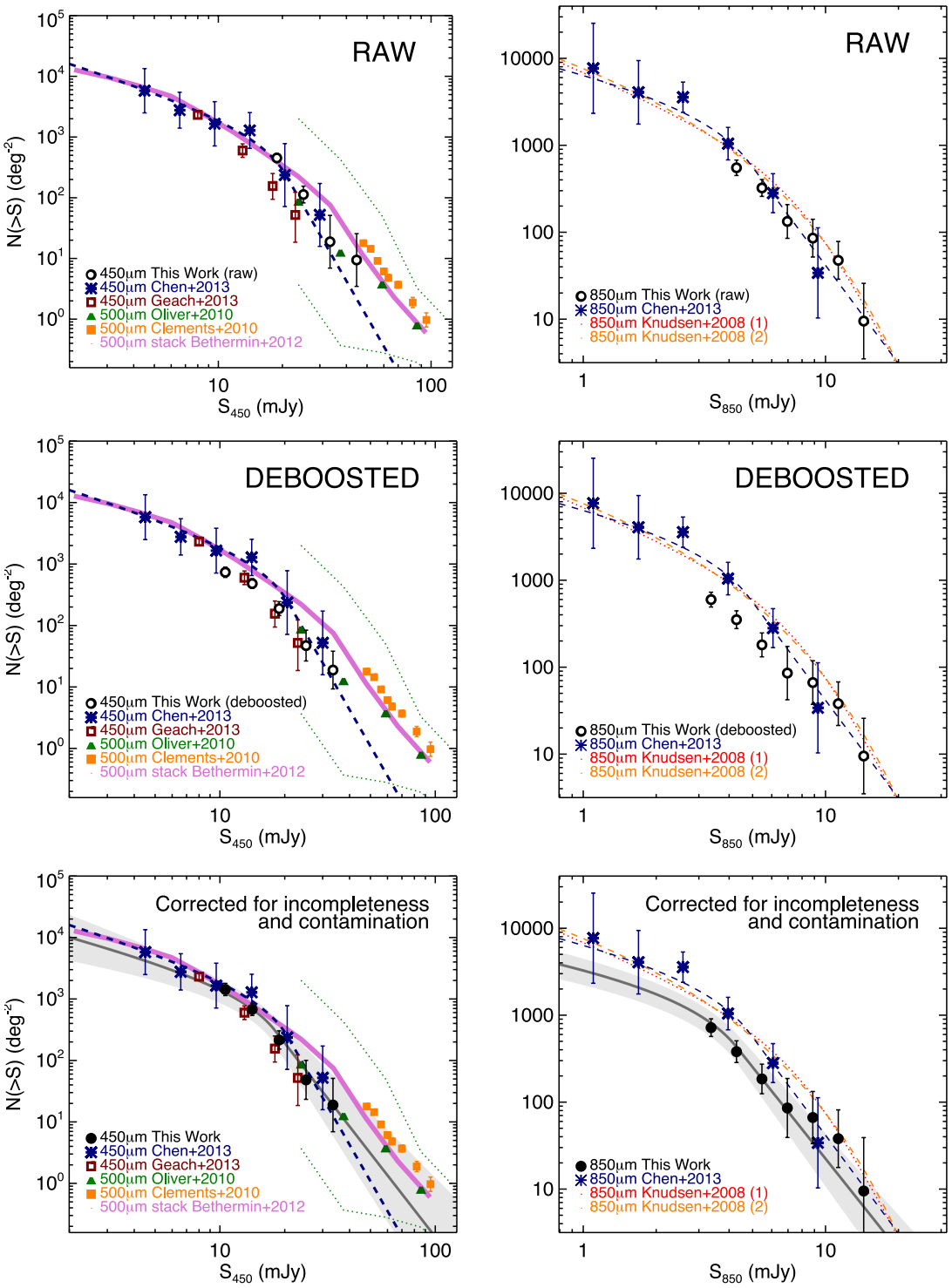

Figure 8. The cumulative number counts at 450 μm (left column) and 850 μm (right column) from our COSMOS data. The top row shows the raw number counts, with extracted flux densities from our map, the middle row corrects the sources' flux densities for confusion and Eddington boosting, and the bottom row corrects the deboosted number counts for incompleteness and contamination (as discussed in the text). The best-fitting double power-law parametrization of the number counts is shown in grey in both bottom panels, with associated light grey uncertainties. We compare our measured counts (black open and closed circles) to those in the literature, all corrected for incompleteness and contamination. At 450 μm, we compare to the recent results of Chen et al. (2013) (blue asterisks, blue dashed line) and Geach et al. (2013) (red squares), and we note that the latter work is data taken in the same sky region as our COSMOS map although covering only ∼1/4 of the area. We also compare 450 μm data to 500 μm data from the *Herschel*-SPIRE instrument from Oliver et al. (2010) (green triangles) and Clements et al. (2010) (orange squares). The Béthermin et al. (2012) (pink curve) work is not from direct 500 μm extractions but rather stacks on 24 μm sources at 500 μm. At 850 μm, we overplot the Chen et al. (2013) results and the best-fitting models from equations (3) and (4) in Knudsen et al. (2008) (red-orange curves), called (1) and (2) here, respectively; we omit many data measurements taken at 850 μm to avoid clutter on the plot.

Table 3. True number counts at 450 μm, 850 μm and best-fitting double power-law/Schechter function parameters.

450 μm number counts				850 μm number counts			
S_{450} (mJy)	N	dN/dS (mJy^{-1} deg^{-2})	$N(>S)$ (deg^{-2})	S_{850} (mJy)	N	dN/dS (mJy^{-1} deg^{-2})	$N(>S)$ (deg^{-2})
10.59	15	154^{+51}_{-38}	1430^{+370}_{-290}	2.65	20	579^{+157}_{-124}	1040^{+300}_{-230}
14.13	27	129^{+31}_{-25}	679^{+175}_{-139}	3.37	23	412^{+104}_{-83}	719^{+189}_{-150}
18.84	29	$66.1^{+15.0}_{-12.2}$	215^{+88}_{-62}	4.29	27	306^{+70}_{-57}	380^{+127}_{-95}
25.12	5	$6.87^{+4.13}_{-2.58}$	48^{+52}_{-25}	5.46	19	$78.2^{+31.0}_{-22.2}$	185^{+88}_{-60}
33.50	1	$0.97^{+1.80}_{-0.63}$	18^{+32}_{-12}	6.96	7	$40.4^{+19.7}_{-13.2}$	$85.6^{+101.5}_{-46.4}$
				8.86	3	$13.3^{+11.1}_{-6.0}$	$66.5^{+66.1}_{-33.2}$
				11.28	4	$13.9^{+9.6}_{-5.7}$	$38.0^{+43.6}_{-20.3}$
				14.37	1	$2.7^{+5.1}_{-1.8}$	$9.5^{+29.6}_{-7.2}$

Best-fitting parameters to equation (1)

	450 μm parameters	850 μm parameters
$N_0 =$	$(1.4 \pm 0.4) \times 10^3$	$(1.5 \pm 0.4) \times 10^3$
$S_0 =$	18 ± 8	4.3 ± 1.8
$\alpha =$	1.91 ± 0.40	1.34 ± 0.09
$\beta =$	5.5 ± 1.0	4.50 ± 0.38

Best-fitting parameters to equation (2)

	450 μm parameters	850 μm parameters
$N_0 =$	$(1.1 \pm 0.4) \times 10^4$	$(3.3 \pm 1.4) \times 10^3$
$S_0 =$	6.1 ± 1.0	3.7 ± 1.1
$\alpha =$	0.5 ± 1.3	1.4 ± 1.1

Notes. Number counts are given in differential and cumulative form. The number of sources contributing to each bin is given as the number 'N'. The best-fitting parameters to the number counts are given at bottom and are fit to the differential counts.

population is intrinsically different than the 850 μm population, either probing a different redshift regime, luminosity regime or temperature regime than the 850 μm population. Similarly, only 19 of 99 850 μm sources are 450 μm detected $>3.6\sigma$, with an additional 16 which are marginal $>3\sigma$ detections and four nearby sources (<12 arcsec) which are not formally matched. This translates to a 450 μm detection rate of 850 μm sources of 19–39 per cent. We investigate the reasons for such little overlap in the next section.

Chen et al. (2013) showed that sources detected at both 450 μm and 850 μm at low-S/N (e.g. 3–4σ) have effective S/N higher than the individual S/N in either band, in other words, that a source which is 3σ at 450 μm and 3σ at 850 μm is effectively a 4σ detection. We use this technique to extract 450 μm sources below our nominal detection threshold. The additional $3<\sigma<3.6$ 450 μm sources we detect with 850 μm counterparts are given in Table 4. We exclude these sources from our 450 μm number count computation due to the unquantified bias which requiring a 850 μm counterpart enforces on the sample, but we can use this sample for comparisons to the independently detected $>3.6\sigma$ 450 μm sample in redshift, luminosity and temperature space.

3.4 Counterpart matching

Determining the optical/NIR counterparts to submillimetre sources is complex, but thanks to the low positional uncertainty on our 450 μm sources, it is a much more straightforward process than in other submillimetre maps. A handful of sources in our sample (five sources at 450 μm, eight at 850 μm) have interferometric observations either with the SMA (Younger et al. 2007, 2009) or the Plateau de Bure Interferometer (Smolčić et al. 2012) where the counterparts to submm observations are known, but the rest of the sample needs careful counterpart analysis. Our counterpart matching procedure at 450 μm and 850 μm is the same at both wavelengths, but we note that the added uncertainty at 850 μm generates many more potential counterparts and is, therefore, naturally more uncertain.

All optical (i-band), NIR (3.6 μm), 24 μm and 1.4 GHz radio sources which fall within the 90 per cent confidence positional uncertainty are considered as possible counterparts. Optical sources are taken from the Ilbert et al. catalogue, which identifies individual sources down to $i \sim 27$. Although we consider sources within the nominal positional uncertainty found by our simulations (as shown in Fig. 5), additional accommodation must be made for uncertainty in the positions measured at other wavelengths or source size. Since SCUBA-2 450 μm positional uncertainties are of the order of 1–2 arcsec, a source's size or positional uncertainty at other wavelengths is not negligible. At optical and NIR wavelengths we are able to estimate sources' 'positional uncertainty' by considering its measured size; we fix the positional uncertainty for each source individually by taking the area (measured in arcsec squared) and elongation (both measured using SEXTRACTOR[3]) to convert to a semi-major axis. Most optical/NIR sources have approximated semi-major axes ∼0.5 arcsec, with 90 per cent of sources being <1 arcsec. Therefore, when seeking potential matches to 450 μm sources, we search within a radius which is the 450 μm source's positional uncertainty and the optical/NIR sources' approximated semi-major axis summed in quadrature.

The positional uncertainty of 24 μm and 1.4 GHz sources is estimated with a more statistical method (since the resolution is not adequate to resolve source sizes) by measuring the global offset of 24 μm and 1.4 GHz sources to K-band and i-band positions. We find that 90 per cent of 24 μm sources lie within 1.05 arcsec of their associated optical/NIR counterpart and 90 per cent of 1.4 GHz sources lie within 0.85 arcsec. Therefore, we add 1.05 arcsec and 0.85 arcsec (in quadrature) to our search radius for 24 μm and 1.4 GHz counterparts, respectively. We observe many instances where 24 μm and 1.4 GHz counterparts fall outside the 450 μm positional uncertainty but lie <1 arcsec beyond the positional uncertainty (e.g. 450.01). The median search radii at 450 μm and 850 μm were 2.2 arcsec and 4.2 arcsec, respectively.

The advantage of identifying radio counterparts comes from the well-known FIR/radio correlation for starburst galaxies (Helou, Soifer & Rowan-Robinson 1985; Condon 1992), whereby a radio-detected galaxy is likely to be FIR-bright, and thus correspond to the source generating the FIR emission detected in our SCUBA-2 maps (Barger, Cowie & Richards 2000; Chapman et al. 2003, 2005). MIPS 24 μm emission also correlates with FIR emission since both are seen in dusty galaxies, although the relationship is more complex due to the variation of SED types in the MIR (PAH emission features drifting in and out of the band, and AGN generated power-law emission; Le Floc'h et al. 2005; Lee et al. 2010). The existence of a MIR or radio counterpart within the beamsize of 450 μm observations can help distinguish that source from others as the likely counterpart, since the likelihood of random coincidence is quite low (this likelihood is often called the p-value; Downes et al. 1986).[4]

[3] SEXTRACTOR: a Source Extractor program developed in Bertin & Arnouts (1996).

[4] We calculate the p-value (defined by $p = 1 - \exp(-\pi n \theta^2)$ where n is the source density, θ the angular offset or search area) by assuming the following source densities which we measure in this area of the COSMOS field: 885 900 deg^{-2} at i band; 151 900 deg^{-2} at 3.6 μm; 19 400 deg^{-2} at 24 μm; and 2300 deg^{-2} at 1.4 GHz.

Table 4. Marginal $3 < \sigma < 3.6$ 450 μm identified sources with 850 μm $>3\sigma$ counterparts.

Name	850 μm short name	450 μm short name	Offset (arcsec)	RA_{450}	DEC_{450}	S/N_{850}	S/N_{450}	S_{450} Raw (mJy)	S_{450} Deboosted (mJy)	S_{850} Raw (mJy)	S_{850} Deboosted (mJy)	$\Delta(\alpha,\delta)$ (arcsec)
SMM J100031.0+022751...	850.62	450.78	0.9	10:00:31.0	+02:27:51	4.29	3.60	14.94 ± 4.15	10.72 ± 4.99	3.46 ± 0.81	2.80 ± 0.96	2.42
SMM J100034.3+022121...	850.10	450.81	0.8	10:00:34.3	+02:21:21	8.60	3.58	14.71 ± 4.11	10.47 ± 4.98	6.90 ± 0.80	6.24 ± 1.13	2.45
SMM J095950.8+022745...	850.55	450.86	3.6	09:59:50.8	+02:27:45	4.51	3.55	19.80 ± 5.58	13.95 ± 6.80	4.77 ± 1.06	3.89 ± 1.27	2.50
SMM J100025.1+021847...	850.09	450.87	2.8	10:00:25.1	+02:18:47	8.89	3.55	15.24 ± 4.30	10.74 ± 5.24	7.47 ± 0.84	6.83 ± 1.17	2.50
SMM J100022.2+022842...	850.23	450.94	0.6	10:00:22.2	+02:28:42	6.24	3.50	14.67 ± 4.19	10.14 ± 5.17	5.06 ± 0.81	4.31 ± 1.07	2.58
SMM J100052.8+021906...	850.103	450.95	3.1	10:00:52.8	+02:19:06	3.54	3.50	18.59 ± 5.31	12.83 ± 6.56	3.88 ± 1.10	2.94 ± 1.34	2.59
SMM J100049.8+022448...	850.133	450.96	8.2	10:00:49.8	+02:24:48	3.25	3.49	15.25 ± 4.36	10.50 ± 5.39	2.85 ± 0.88	2.06 ± 1.09	2.60
SMM J095950.7+022823...	850.33	450.99	3.7	09:59:50.7	+02:28:23	5.54	3.47	20.15 ± 5.80	13.76 ± 7.20	6.20 ± 1.12	5.18 ± 1.41	2.63
SMM J100025.0+022757...	850.85	450.105	4.5	10:00:25.0	+02:27:57	3.73	3.44	14.24 ± 4.14	9.60 ± 5.16	2.99 ± 0.80	2.32 ± 0.97	2.69
SMM J100041.8+022358...	850.92	450.106	5.6	10:00:41.8	+02:23:58	3.67	3.44	14.19 ± 4.13	9.57 ± 5.15	2.94 ± 0.80	2.27 ± 0.97	2.69
SMM J100025.6+023051...	850.159	450.126	12.3	10:00:25.6	+02:30:51	3.05	3.36	15.79 ± 4.70	10.32 ± 5.91	2.89 ± 0.95	2.02 ± 1.19	2.83
SMM J100029.5+022131...	850.131	450.133	2.6	10:00:29.5	+02:21:31	3.27	3.32	13.67 ± 4.12	8.78 ± 5.19	2.64 ± 0.81	1.91 ± 1.00	2.90
SMM J100011.8+022935...	850.52	450.134	1.7	10:00:11.8	+02:29:35	4.73	3.31	14.45 ± 4.36	9.26 ± 5.50	4.09 ± 0.86	3.37 ± 1.04	2.91
SMM J095953.0+022641...	850.163	450.135	3.5	09:59:53.0	+02:26:41	3.00	3.31	16.78 ± 5.07	10.76 ± 6.39	2.91 ± 0.97	2.02 ± 1.22	2.91
SMM J100010.1+021758...	850.83	450.166	1.8	10:00:10.1	+02:17:58	3.77	3.24	15.87 ± 4.90	9.79 ± 6.20	3.52 ± 0.93	2.74 ± 1.12	3.08
SMM J100005.4+022516...	850.104	450.173	6.4	10:00:05.4	+02:25:16	3.51	3.22	13.31 ± 4.13	8.11 ± 5.23	2.82 ± 0.80	2.12 ± 0.98	3.13
SMM J100022.6+023023...	850.88	450.179	6.8	10:00:22.6	+02:30:23	3.69	3.21	14.51 ± 4.52	8.80 ± 5.73	3.31 ± 0.90	2.56 ± 1.08	3.15
SMM J100014.1+022836...	850.114	450.189	8.2	10:00:14.1	+02:28:36	3.40	3.17	13.37 ± 4.22	7.92 ± 5.33	2.81 ± 0.83	2.08 ± 1.02	3.25
SMM J100005.0+021718...	850.49	450.193	0.6	10:00:05.0	+02:17:18	4.79	3.16	17.40 ± 5.50	10.27 ± 6.95	4.91 ± 1.02	4.05 ± 1.24	3.27
SMM J100011.1+021507...	850.53	450.206	4.8	10:00:11.1	+02:15:07	4.68	3.14	20.69 ± 6.60	12.04 ± 8.32	5.72 ± 1.22	4.70 ± 1.47	3.33
SMM J100023.6+021916...	850.27	450.215	2.7	10:00:23.6	+02:19:16	6.08	3.11	13.05 ± 4.20	7.48 ± 5.28	5.00 ± 0.82	4.23 ± 1.08	3.39
SMM J100032.0+023324...	850.67	450.240	5.9	10:00:32.0	+02:33:24	4.07	3.06	19.01 ± 6.21	10.61 ± 7.75	5.15 ± 1.26	4.12 ± 1.50	3.51
SMM J100041.3+022534...	850.151	450.247	11.5	10:00:41.3	+02:25:34	3.12	3.05	12.58 ± 4.13	6.97 ± 5.14	2.52 ± 0.81	1.79 ± 1.02	3.54
SMM J100013.4+022224...	850.40	450.252	3.7	10:00:13.4	+02:22:24	5.20	3.04	12.57 ± 4.14	6.91 ± 5.15	4.16 ± 0.80	3.47 ± 0.99	3.57

Notes. Sources extracted down to 3σ in the 450 μm map using 850 μm $>3\sigma$ positional priors. The 450 μm $>3\sigma$ list (with 274 sources) was checked against the 850 μm $>3\sigma$ list (with 164 sources) and 25 sources were found. The positions here are given by their 450 μm detection with associated positional uncertainty and the Offset is the offset between 450 μm and 850 μm centroid. The short names are numbered in order of decreasing S/N for all sources extracted in the map, e.g. from 450.00 at S/N = 7.80 to 450.273 with S/N = 3.00, hence the high, non-sequential numbers given at both 450 μm and 850 μm.

A summary of counterparts is found in Table 5 for 450 μm sources, Table 6 for marginal 450 μm sources and Table 7 for 850 μm sources which are not 450 μm detected. Photometric redshifts (Ilbert et al. 2010) are quoted where available. Also, the handful of sources which have interferometric observations have their known counterparts in bold in Tables 5–7. The interferometrically observed subset of SCUBA-2 sources (along with all SCUBA-2 sources which were detected with other submillimetre instruments) is given in Table 8. The best-guess counterpart is the source with the lowest *p*-value; generally, a *p*-value <0.05 can be regarded as confident, while larger *p*-values are more tentative. Sources with *p*-values >0.5 are removed from Tables 6–7 since they are more likely not truly associated counterparts. Fig. 9 shows 12 × 12 arcsec^2 postage stamp cut-outs of the 450 μm sources in the optical (*Biz* tricolour) and NIR (IRAC 3.6 μm) with radio and 24 μm counterparts identified for reference.

A significant fraction of sources, both at 450 μm and at 850 μm, lack 24 μm or radio counterparts. At 450 μm, only 44 per cent (=34/78) of sources have 24 μm or radio counterparts and at 850 μm, only 60 per cent (=59/99, which is consistent with previous rates at 850 μm; Coppin et al. 2005). These fractions should improve with deeper radio data (e.g. as in Barger et al. 2012), which should be available in the coming years in the COSMOS field, but it would not fix the bias introduced in submillimetre samples which are reliant on these counterparts. Studies which are reliant on multiwavelength counterpart identification, yet which have a significant number of galaxies lacking counterparts, will be biased. However, note that the majority of sources without 24 μm or radio counterparts *do* have IRAC NIR counterparts (∼33/44 = 75 per cent), and of those that do not, seven sources have no counterparts at all (i.e. also lack any optical counterparts). This leaves only four objects (in both 450 μm and 850 μm samples) which rely on matching directly to optical counterparts – the most uncertain method generating the highest *p*-values. The median *p*-values for the different counterpart matching methods at 450 μm are the following: 0.0009 (1.4 GHz, 16 galaxies), 0.02 (24 μm, 18 galaxies), 0.09 (3.6 μm, 33 galaxies) and 0.30 (optical/*i* band, four galaxies).

3.5 Reliability of counterpart identifications

Identifying the correct multiwavelength counterpart(s) for each submillimetre source is the most important, but also the most difficult aspect of characterizing the SMG population. Recently, it has become clear that direct, FIR interferometry is the only guaranteed method of identifying counterparts correctly (e.g. recent results from SMA, PdBI and ALMA targeting 850 μm–1.1 mm sources; Younger et al. 2008; Wang et al. 2011; Barger et al. 2012; Smolčić et al. 2012; Karim et al. 2013; Hodge et al. 2013). For 850 μm sources detected with a ∼15 arcsec beamsize, interferometric work suggests that best-guess counterpart matching to radio and/or 24 μm counterparts will fail ∼30 per cent of the time (Hodge et al. 2013, and Smail, private communication), dependent on ancillary field depth and robustness of FIR/radio and FIR/MIR correlations. This provides a good estimate to the accuracy of the counterparts given for our 850 μm sample, but what is the reliability of our 450 μm source counterparts?

For the five 450 μm sources which have interferometric observations, four would have been traditionally matched with their truthful counterpart using our method; two of those sit within the 450 μm positional uncertainty <1.5 arcsec, two are outside but still <2 arcsec away, and one source, 450.08, is 6.8 arcsec away from our

Table 5. Counterpart identifications and multiwavelength properties for SCUBA-2 450 μm detected sources.

Name	Counterpart no.	*p*-*val*	RA_{24}	DEC_{24}	δ_{24} (arcsec)	S_{24} (μJy)	$RA_{1.4}$	$DEC_{1.4}$	$\delta_{1.4}$ (arcsec)	$S_{1.4}$ (μJy)	RA_{opt}	DEC_{opt}	δ_{opt} (arcsec)	*i* (AB-mag)	3.6 μm (AB-mag)	z_{phot}
450.00	1/2	0.09									10:00:28.66	+02:32:03.3	1.58	26.78	23.01	2.86
	2/2	0.09									10:00:28.58	+02:32:02.0	1.59	24.01	22.70	0.75
450.01	1/1	0.01	10:00:33.35	+02:26:01.6	1.87	297 ± 16					**10:00:33.38**	**+02:26:01.4**	1.73	26.09	21.30	2.88
	2/2	0.15									10:00:33.49	+02:26:00.1	2.11	26.94	23.84	2.10
450.02	1/3	0.03									10:01:09.00	+02:22:56.1	0.87	24.89	20.85	2.16
	2/3	0.03	10:01:09.15	+02:22:55.0	1.70	1492 ± 248					10:01:09.19	+02:22:54.1	2.67	–	–	–
	3/3	0.11									10:01:08.95	+02:22:54.6	1.81	25.75	20.32	2.18
450.03	1/1	0.0009	10:00:08.01	+02:26:11.0	1.13	287 ± 15	10:00:08.02	+02:26:12.1	0.83	76 ± 14	**10:00:08.04**	**+02:26:10.7**	1.29	22.09⋆	21.83⋆	–
450.04	1/2	0.0009	10:00:19.76	+02:32:03.9	1.87	189 ± 13	10:00:19.75	+02:32:04.3	1.42	126 ± 15	**10:00:19.75**	**+02:32:04.5**	1.24	25.83	22.42	3.82
	2/2	0.16									10:00:19.73	+02:32:06.6	0.89	26.56	–	1.13
450.05	1/1	0.001	10:00:23.65	+02:21:55.3	1.54	236 ± 16	10:00:23.67	+02:21:55.3	1.68	43 ± 11	**10:00:23.67**	**+02:21:55.5**	1.55	27.23	21.01	3.99
450.06	1/2	0.0004	10:00:39.25	+02:22:21.1	0.69	544 ± 17	10:00:39.24	+02:22:21.0	0.77	138 ± 15	10:00:39.23	+02:22:20.9	0.87	23.62	20.47	2.08
	2/2	0.11									10:00:39.18	+02:22:23.4	1.82	29.93	23.20	2.27
450.07	1/1	0.002	10:00:14.25	+02:30:19.0	1.26	467 ± 100	10:00:14.20	+02:30:19.1	1.70	200 ± 13	–	–	–	–	–	–
450.08	1/2	0.03									**10:00:25.55**	**+02:15:08.4**	6.76	–	–	–
	2/2	0.11									10:00:25.24	+02:15:09.8	1.79	24.69	22.85	1.86
450.09	1/3	0.0005	10:00:16.59	+02:26:38.4	0.72	890 ± 17	10:00:16.57	+02:26:38.4	0.92	5716 ± 73	10:00:16.56	+02:26:39.8	2.25	24.39	21.42	1.90
	2/3	0.13									10:00:16.70	+02:26:36.3	1.98	25.02	22.87	1.72
	2/3	0.16									10:00:16.71	+02:26:39.3	2.18	26.47	23.47	1.98
450.10	1/1	0.01	10:00:22.27	+02:23:53.5	1.46	95 ± 18					10:00:22.28	+02:23:54.1	1.13	25.23	21.35	–
	2/2	0.14									10:00:22.14	+02:23:56.5	2.06	24.64	21.55	–
450.11	1/2	0.01	10:00:25.45	+02:25:44.2	1.53	116 ± 15					–	–	–	–	–	–
	2/2	0.19									10:00:25.42	+02:25:40.5	2.37	24.60	23.37	–
450.12	1/1	0.13									09:59:57.09	+02:21:51.9	1.91	22.67	19.82	0.93
450.13	1/1	0.002	10:00:01.66	+02:24:27.9	1.47	287 ± 12	10:00:01.66	+02:24:28.2	1.80	90 ± 14	10:00:01.61	+02:24:28.0	2.11	26.39	21.32	2.87
450.14	1/2	0.02	10:00:45.01	+02:19:21.0	2.15	228 ± 20					10:00:45.02	+02:19:21.1	2.37	23.88	19.39	1.47
	2/2	0.06									10:00:44.93	+02:19:20.0	0.54	–	–	–
450.15	1/1	0.001	10:00:04.36	+02:20:59.6	1.50	402 ± 14	10:00:04.37	+02:20:59.7	1.62	56 ± 12	10:00:04.33	+02:20:59.7	1.10	26.23	22.51	2.79
	2/2	0.01									10:00:04.23	+02:20:59.5	0.50	26.97	23.18	2.62
450.16	1/2	0.004	10:00:57.28	+02:20:12.0	2.37	132 ± 16	10:00:57.26	+02:20:12.2	2.54	81 ± 15	10:00:57.46	+02:20:11.0	3.58	24.87	20.50	2.32
	2/2	0.11									10:00:57.13	+02:20:08.9	1.79	26.44	22.76	2.22
450.17	1/4	0.05									10:00:17.29	+02:25:21.4	1.23	26.19	24.85	1.23
	2/4	0.14									10:00:17.24	+02:25:23.7	2.02	25.56	24.99	–
	3/4	0.14									10:00:17.16	+02:25:23.7	2.09	25.38	24.73	–
	5/4	0.19									10:00:17.10	+02:25:20.0	2.40	24.78	22.64	–
450.18	1/1	0.09									10:00:07.22	+02:18:03.9	0.67	27.59	–	–
450.19	1/2	0.14									09:59:48.13	+02:20:12.6	2.06	24.25	21.33	1.11
	2/2	0.28									09:59:48.08	+02:20:17.7	3.01	23.75	20.68	1.32
450.20	1/1	0.12									10:00:04.65	+02:30:42.2	1.87	24.31	23.33	0.76
450.21	1/1	0.005	10:00:17.23	+02:21:39.7	0.99	333 ± 21					10:00:17.22	+02:21:39.8	1.08	21.40	19.38	0.84
450.22	1/2	0.02									10:00:30.80	+02:31:05.4	0.75	26.40	24.03	2.11
	2/2	0.13									10:00:30.70	+02:31:03.9	1.96	25.68	23.85	2.11
450.23	1/1	0.15									10:00:04.51	+02:18:22.3	2.09	24.85	23.09	0.97
450.24	1/2	0.03	10:00:50.23	+02:21:18.1	2.36	1421 ± 216					10:00:50.29	+02:21:19.0	3.58	–	17.50	0.16
	2/2	0.09									10:00:50.09	+02:21:15.1	1.64	24.46	22.93	0.60
450.25	1/1	8×10^{-5}	10:00:28.55	+02:19:28.2	0.49	243 ± 16	10:00:28.57	+02:19:28.0	0.39	78 ± 10	10:00:28.58	+02:19:28.3	0.76	20.54	18.74	0.61
450.26	1/2	0.04									10:00:16.59	+02:20:01.7	1.03	24.76	23.06	2.68
	2/2	0.19									10:00:16.52	+02:20:02.8	2.42	25.26	23.17	2.37
450.27	1/1	0.0002	09:59:42.98	+02:21:44.9	0.19	401 ± 13	09:59:42.94	+02:21:45.0	0.59	153 ± 12	09:59:42.92	+02:21:45.1	0.93	23.42	19.20	–
450.28	1/4	0.02	10:00:56.78	+02:20:12.9	2.17	90 ± 27					10:00:56.83	+02:20:13.3	2.26	24.03	21.39	1.98
	2/4	0.14									10:00:56.77	+02:20:16.5	1.99	25.32	23.44	–

Table 5 – *continued*

Name	counter-part no.	*p-val*	RA_{24}	DEC_{24}	δ_{24} (arcsec)	S_{24} (μJy)	$RA_{1.4}$	$DEC_{1.4}$	$\delta_{1.4}$ (arcsec)	$S_{1.4}$ (μJy)	RA_{opt}	DEC_{opt}	δ_{opt} (arcsec)	i (AB-mag)	3.6 μm (AB-mag)	z_{phot}
	3/4	0.19									10:00:56.56	+02:20:15.7	2.40	25.96	24.74	1.46
	4/4	0.30									10:00:56.65	+02:20:13.8	1.28	26.69	–	1.61
450.29	1/2	0.16									10:00:00.58	+02:25:03.5	0.90	28.57	–	–
	2/2	0.34									10:00:00.48	+02:25:04.9	1.40	27.28	–	2.49
450.30	1/1	0.002	10:00:48.33	+02:29:26.3	0.63	185 ± 14					10:00:48.35	+02:29:26.0	1.04	26.93	21.83	2.81
450.31	1/2	0.09									10:00:08.36	+02:22:42.3	1.61	25.32	21.45	–
	2/2	0.11									10:00:08.58	+02:22:42.4	1.79	25.15	23.71	–
450.32	1/2	0.008	10:00:10.27	+02:26:25.4	1.29	143 ± 13					10:00:10.22	+02:26:25.2	0.53	26.15	20.43	1.72
	2/2	0.20									10:00:10.36	+02:26:24.0	2.46	26.53	22.62	2.71
450.33	1/3	0.02	10:00:21.19	+02:30:55.5	2.32	255 ± 18					10:00:21.19	+02:30:55.4	2.38	22.17	19.70	0.84
	2/3	0.11									10:00:21.46	+02:30:55.5	1.77	26.86	22.90	2.16
	3/3	0.16									10:00:21.29	+02:30:57.7	2.15	26.74	23.23	5.62
450.34	1/2	0.004	09:59:45.11	+02:22:55.1	2.50	726 ± 14	09:59:45.10	+02:22:55.1	2.67	89 ± 11	09:59:45.06	+02:22:55.0	3.04	–	–	–
	2/2	0.02									09:59:45.30	+02:22:53.6	0.76	24.77	23.10	–
450.35	NA															
450.36	1/2	0.04	10:01:01.24	+02:28:00.6	2.88	104 ± 15					10:01:01.26	+02:28:00.5	3.21	–	–	–
	2/2	0.10									10:01:01.00	+02:28:01.0	0.70	27.10	–	–
450.37	1/1	0.002									10:00:01.54	+02:19:39.9	0.22	24.21	22.97	2.17
450.38	1/4	0.0007	10:00:10.38	+02:22:24.4	0.98	381 ± 14	10:00:10.36	+02:22:24.8	1.14	100 ± 13	10:00:10.38	+02:22:24.4	1.03	25.78	20.61	–
	2/4	0.04									10:00:10.31	+02:22:22.7	1.06	26.59	22.22	–
	3/4	0.19									10:00:10.28	+02:22:21.5	2.41	26.43	23.81	–
	4/4	0.21									10:00:10.43	+02:22:21.7	2.53	26.84	23.73	–
450.39	1/1	0.22									10:00:11.37	+02:15:55.3	2.58	23.29	22.29	0.61
450.40	NA															
450.41	1/1	0.20									10:00:06.77	+02:15:29.7	2.43	27.31	24.76	3.46
450.42	1/3	0.04	10:00:36.88	+02:19:41.3	2.85	87 ± 15					10:00:36.89	+02:19:40.5	2.07	26.89	22.03	4.81
	2/3	0.09									10:00:37.06	+02:19:39.0	1.60	26.23	24.17	2.72
	3/3	0.19									10:00:36.88	+02:19:36.7	2.36	23.91	23.35	0.44
450.43	1/2	0.16									10:00:28.79	+02:33:38.3	2.18	24.91	23.92	0.36
	2/2	0.23									10:00:29.03	+02:33:35.2	2.64	25.39	22.99	2.19
450.44	1/3	0.02									10:00:54.54	+02:19:19.2	0.70	26.38	24.91	1.75
	2/3	0.08									10:00:54.43	+02:19:20.7	1.55	26.06	24.33	2.25
	3/3	0.16									10:00:54.44	+02:19:17.9	2.14	25.15	24.11	0.92
450.45	1/1	0.18									10:00:56.16	+02:18:29.4	2.29	26.97	24.17	2.01
450.46	1/2	0.02									10:00:32.46	+02:21:49.1	0.74	24.77	22.16	3.06
	2/2	0.14									10:00:32.29	+02:21:49.0	2.01	24.69	22.49	2.73
450.47	1/3	0.02	10:00:25.24	+02:19:32.9	2.24	84 ± 15					10:00:25.26	+02:19:33.1	2.47	–	–	–
	2/3	0.02									10:00:25.21	+02:19:30.1	0.68	28.22	24.39	2.77
	3/3	0.19									10:00:25.07	+02:19:29.7	2.36	25.87	24.60	3.03
450.48	1/3	0.09									10:00:09.37	+02:22:24.3	1.62	–	24.43	–
	2/3	0.11									10:00:09.57	+02:22:24.6	1.75	27.38	23.47	–
	3/3	0.23									10:00:09.60	+02:22:21.8	2.68	27.17	23.17	–
450.49	1/2	0.17									09:59:59.98	+02:25:22.7	2.28	25.41	24.16	1.70
	2/2	0.23									10:00:00.20	+02:25:23.0	2.68	26.21	–	2.55
450.50	1/2	0.40									09:59:52.33	+02:21:32.7	1.53	27.79	–	–
	2/2	0.48									09:59:52.21	+02:21:35.3	1.75	–	–	–
450.51	1/3	0.13									10:00:44.41	+02:23:11.9	1.95	25.56	23.87	1.58
	2/3	0.21									10:00:44.20	+02:23:13.7	2.50	26.22	22.57	2.58
	3/3	0.25									10:00:44.32	+02:23:16.4	2.77	23.29	21.72	0.97
450.52	NA															
450.53	1/1	0.007	10:00:10.33	+02:20:27.1	1.19	413 ± 15					10:00:10.32	+02:20:27.4	1.36	22.95	19.03	1.01

Table 5 – *continued*

Name	counter-part no.	*p*-*val*	RA_{24}	DEC_{24}	δ_{24} (arcsec)	S_{24} (μJy)	$RA_{1.4}$	$DEC_{1.4}$	$\delta_{1.4}$ (arcsec)	$S_{1.4}$ (μJy)	RA_{opt}	DEC_{opt}	δ_{opt} (arcsec)	*i* (AB-mag)	3.6 μm (AB-mag)	z_{phot}
450.54	1/2	0.006									10:00:26.86	+02:23:18.5	0.40	24.82	22.74	1.90
	2/2	0.24									10:00:27.01	+02:23:20.7	2.73	27.04	24.52	2.01
450.55	1/2	0.04	10:00:23.96	+02:17:50.1	2.78	162 ± 17					10:00:24.01	+02:17:50.3	3.26	–	–	–
	2/2	0.22									10:00:23.81	+02:17:54.3	2.60	24.73	22.64	2.60
450.56	1/3	0.30									09:59:59.40	+02:30:02.0	1.29	26.49	–	2.82
	2/3	0.40									09:59:59.34	+02:29:59.4	1.54	26.06	–	3.18
	3/3	0.46									09:59:59.50	+02:30:00.2	1.69	26.82	–	1.94
450.57	1/1	0.11									10:00:32.46	+02:18:04.4	1.79	28.59	21.85	3.48
450.58	1/1	0.02	10:00:36.05	+02:21:51.1	2.28	194 ± 17					10:00:36.03	+02:21:51.1	2.53	24.47	20.79	–
450.59	1/2	0.005	10:00:19.35	+02:20:24.2	1.08	197 ± 52					10:00:19.44	+02:20:24.5	0.61	20.61	19.60	0.47
	2/2	0.04	10:00:19.61	+02:20:24.3	3.05	86 ± 15					–	–	–	–	–	–
450.60	NA															
450.61	1/1	2×10^{-5}	10:00:18.76	+02:28:13.5	0.32	136 ± 13	10:00:18.76	+02:28:13.7	0.20	92 ± 11	10:00:18.81	+02:28:14.1	1.11	25.04	21.88	4.58
450.62	1/1	0.47									10:00:47.23	+02:20:48.4	1.71	27.78	–	1.95
450.63	1/3	0.05									10:00:19.94	+02:21:29.2	1.20	25.09	24.02	2.36
	2/3	0.17									10:00:20.07	+02:21:31.8	2.25	24.40	23.74	2.84
	3/3	0.22									10:00:19.87	+02:21:28.1	2.58	25.19	24.42	1.56
450.64	NA															
450.65	1/1	0.30									10:00:27.23	+02:24:49.8	1.29	25.42	–	0.70
450.66	1/4	8×10^{-5}	10:01:04.63	+02:26:34.0	0.47	586 ± 24	10:01:04.64	+02:26:34.0	0.38	86 ± 11	10:01:04.63	+02:26:33.2	0.51	23.20	20.54	–
	2/4	0.07									10:01:04.70	+02:26:34.9	1.45	22.59	20.44	–
	3/4	0.22									10:01:04.53	+02:26:35.5	2.60	25.94	22.14	–
	4/4	0.23									10:01:04.56	+02:26:31.4	2.64	21.86	20.50	–
450.67	1/2	0.002	10:00:00.37	+02:29:03.9	1.43	538 ± 15	10:00:00.35	+02:29:04.4	1.76	114 ± 14	10:00:00.35	+02:29:04.1	1.47	21.37	19.06	0.93
	2/2	0.23									10:00:00.42	+02:29:00.5	2.64	25.83	23.47	1.67
450.68	NA															
450.69	1/2	0.05									10:00:47.55	+02:25:21.6	1.16	26.82	23.67	2.04
	2/2	0.05	10:00:47.29	+02:25:20.7	3.20	251 ± 14					10:00:47.27	+02:25:20.3	3.45	22.28	19.36	0.95
450.70	1/2	0.006	09:59:52.66	+02:27:12.8	1.13	263 ± 15					09:59:52.66	+02:27:14.0	2.30	23.77	21.06	3.03
	2/2	0.10									09:59:52.59	+02:27:10.3	1.67	26.17	22.47	2.89
450.71	1/1	0.006									09:59:46.40	+02:29:32.0	0.42	26.81	24.22	1.95
450.72	1/2	0.20									09:59:50.44	+02:20:18.9	2.48	25.61	22.92	1.43
	2/2	0.26									09:59:50.54	+02:20:19.6	2.87	24.92	23.11	1.72
450.73	NA															
450.74	1/2	0.13									10:00:41.26	+02:16:42.1	1.96	22.79	21.36	0.75
	2/2	0.19									10:00:41.39	+02:16:39.9	0.99	26.45	–	0.96
450.75	1/2	0.08									10:00:34.20	+02:34:22.4	1.48	26.81	24.79	2.26
	2/2	0.18									10:00:34.33	+02:34:24.0	2.32	–	23.01	–
450.76	1/2	0.02									10:00:21.76	+02:31:14.0	0.77	31.02	24.83	1.96
	2/2	0.27									10:00:21.93	+02:31:15.7	2.92	25.27	23.61	0.73
450.77	1/2	0.03									09:59:52.65	+02:22:57.8	0.92	25.12	21.05	1.43
	2/2	0.07									09:59:52.62	+02:23:00.0	1.41	25.64	22.35	1.65

Notes. All possible counterparts (24 μm, radio and optical/near-IR) for SCUBA-2 450 μm identified $>3.6\sigma$ sources. The best-guess counterpart is the source with the lowest *p*-value of any within the search radius (see text for details). Sources with a *p*-value >0.50 are excluded from this table since they are more likely a random coincident source than a true counterpart. Counterparts with optical/near-IR positions in bold are submillimetre sources which have been observed interferometrically in the literature, therefore the correct counterpart is known as the source at the given position. See the text (Section 3.5) for details on reliability of counterpart identifications. All positional offsets, δ_{24}, $\delta_{1.4}$ and δ_{opt} are measured with respect to the SCUBA-2 450 μm position. *The *i*-band and 3.6 μm magnitudes for 450.03/850.00 is measured from the *HST* imaging, where it can be decoupled from the bright elliptical nearby (1.6 arcsec). ‡The 24 μm flux density for 450.07 is originally measured as 1.3 mJy; this is an obvious blend with a nearby bright source. We have approximated the contribution from 450.07 to be ∼38 per cent, thus we arrive at 467μJy. Sources whose optical magnitudes are given as '−' are dropouts and the position is measured from the *Spitzer*-IRAC 3.6 μm.

Table 6. Counterpart identifications and Multiwavelength Properties for marginal SCUBA-2 450 μm and 850 μm detected sources.

Name	Counter-part no.	*p*-val	RA_{24}	DEC_{24}	δ_{24} (arcsec)	S_{24} (μJy)	$RA_{1.4}$	$DEC_{1.4}$	$\delta_{1.4}$ (arcsec)	$S_{1.4}$ (μJy)	RA_{opt}	DEC_{opt}	δ_{opt} (arcsec)	*i* (AB-mag)	3.6 μm (AB-mag)	z_{phot}
450.78/850.62	1/2	0.006									10:00:31.05	+02:27:51.8	0.40	27.35	22.40	–
	2/2	0.21									10:00:31.05	+02:27:54.2	2.55	26.26	24.53	–
450.81/850.10	1/3	2×10^{-5}	10:00:34.33	+02:21:21.4	0.53	130 ± 17	10:00:34.37	+02:21:21.6	0.21	517 ± 23	10:00:34.33	+02:21:21.0	0.76	25.34	21.78	1.75
	2/3	0.19									10:00:34.43	+02:21:19.6	2.36	25.18	23.21	1.66
	3/3	0.27									10:00:34.53	+02:21:20.2	2.94	25.61	23.80	1.95
450.86/850.55	1/2	0.06									09:59:50.90	+02:27:44.6	1.34	25.86	23.56	3.59
	2/2	0.15									09:59:50.97	+02:27:46.7	2.07	26.80	24.16	3.69
450.87/850.09	1/2	0.004	10:00:25.29	+02:18:45.9	2.76	204 ± 29	10:00:25.28	+02:18:46.2	2.53	58 ± 12	10:00:25.32	+02:18:46.3	2.98	26.22	21.45	2.71
	2/2	0.12									10:00:25.20	+02:18:46.0	1.90	26.82	21.87	4.85
450.94/850.23	1/3	0.03									10:00:22.26	+02:28:43.2	0.83	21.82	20.20	0.71
	2/3	0.03	10:00:22.12	+02:28:44.8	2.50	128 ± 15					10:00:22.04	+02:28:43.9	2.92	24.18	20.44	3.34
	3/3	0.27									10:00:22.32	+02:28:45.2	2.95	24.83	24.95	0.52
450.96/850.133	1/1	0.26									10:00:49.95	+02:24:51.0	2.85	26.67	22.93	2.34
450.99/850.33	1/4	0.02	09:59:50.90	+02:28:22.5	2.19	217 ± 15					09:59:50.86	+02:28:22.4	1.77	26.18	21.21	2.16
	2/4	0.06									09:59:50.69	+02:28:23.8	1.30	27.43	22.86	2.15
	3/4	0.19									09:59:50.64	+02:28:22.5	2.38	26.51	23.82	1.82
	4/4	0.29									09:59:50.78	+02:28:26.7	3.03	26.75	24.02	2.33
450.103/850.128	1/1	0.42									10:00:18.42	+02:23:59.3	3.87	23.82	21.86	1.54
450.105/850.85	1/1	0.03	10:00:25.19	+02:27:55.8	2.58	173 ± 13					10:00:25.17	+02:27:56.0	2.20	22.82	19.21	–
450.106/850.92	1/1	0.44									10:00:42.08	+02:23:59.8	3.95	23.33	20.67	1.00
450.126/850.159	1/1	0.32									10:00:25.70	+02:30:51.2	1.33	26.35	–	2.04
450.133/850.131	1/4	0.03	10:00:29.67	+02:21:29.6	2.74	518 ± 16					10:00:29.68	+02:21:29.8	2.68	20.30	18.51	0.93
	2/4	0.16									10:00:29.60	+02:21:33.8	2.14	26.21	23.39	2.61
	3/4	0.22									10:00:29.68	+02:21:33.5	2.61	26.63	23.34	1.43
	4/4	0.36									10:00:29.46	+02:21:35.0	3.49	25.41	24.20	0.46
450.134/850.52	1/1	0.0002	10:00:11.87	+02:29:35.9	0.20	110 ± 16					10:00:11.82	+02:29:35.3	0.77	–	–	–
	2/4	0.19									10:00:11.82	+02:29:33.5	2.36	25.99	22.11	2.89
	3/4	0.21									10:00:12.02	+02:29:34.7	2.51	27.82	23.50	2.54
	4/4	0.30									10:00:11.86	+02:29:38.9	3.14	28.49	23.70	4.60
450.135/850.163	1/4	0.01	09:59:52.96	+02:26:42.7	1.64	340 ± 14					09:59:52.95	+02:26:42.8	1.83	24.45	21.04	1.68
	2/4	0.05									09:59:52.92	+02:26:40.3	2.46	25.88	23.47	3.06
	3/4	0.08									09:59:53.12	+02:26:40.7	1.46	26.10	24.50	1.11
	4/4	0.20									09:59:53.18	+02:26:42.6	2.10	25.67	24.00	0.66
450.166/850.83	1/2	0.14									10:00:10.34	+02:17:57.3	3.31	23.38	22.20	0.93
	2/2	0.33									10:00:10.17	+02:17:59.7	1.12	26.71	21.35	3.25
450.173/850.104	1/1	0.002	10:00:05.38	+02:25:16.1	0.67	260 ± 20					10:00:05.31	+02:25:15.7	1.67	21.55	19.92	1.01
	2/3	0.27									10:00:05.23	+02:25:18.2	2.93	24.67	22.75	1.09
	3/3	0.33									10:00:05.61	+02:25:17.4	3.28	23.95	20.04	1.19
450.179/850.88	1/4	0.02	10:00:22.77	+02:30:25.3	2.02	103 ± 14					10:00:22.78	+02:30:25.2	2.06	22.06	20.69	0.66
	2/4	0.06									10:00:22.65	+02:30:22.5	1.33	25.78	24.99	0.55
	3/4	0.13									10:00:22.76	+02:30:22.2	1.93	25.06	24.54	0.65
	4/4	0.13									10:00:22.55	+02:30:24.0	1.96	25.68	23.31	2.48
450.189/850.114	1/2	0.003	10:00:14.10	+02:28:38.6	1.94	1345 ± 17	10:00:14.07	+02:28:38.8	2.30	146 ± 11	10:00:14.08	+02:28:38.7	2.16	–	18.34	–
	2/2	0.14									10:00:14.25	+02:28:35.6	1.99	26.30	22.83	–
450.193/850.49	1/6	0.05									10:00:05.13	+02:17:19.4	1.14	24.62	21.16	3.08
	2/6	0.08	10:00:05.09	+02:17:14.6	4.08	159 ± 28					10:00:05.06	+02:17:14.1	4.63	22.61	20.15	1.15
	3/6	0.14									10:00:04.94	+02:17:19.3	2.03	26.59	22.68	3.06
	4/6	0.29									10:00:04.91	+02:17:16.7	3.06	24.95	22.08	2.00

Table 6 – *continued*

Name	Counter-part no.	*p*-val	RA_{24}	DEC_{24}	δ_{24} (arcsec)	S_{24} (μJy)	$RA_{1.4}$	$DEC_{1.4}$	$\delta_{1.4}$ (arcsec)	$S_{1.4}$ (μJy)	RA_{opt}	DEC_{opt}	δ_{opt} (arcsec)	i (AB-mag)	3.6 μm (AB-mag)	z_{phot}
	5/6	0.30									10:00:04.96	+02:17:21.4	3.13	26.57	23.26	3.15
	6/6	0.33									10:00:05.26	+02:17:17.2	3.31	23.99	22.50	3.09
450.206/850.53	1/4	0.08									10:00:11.10	+02:15:06.4	1.47	25.86	24.67	1.70
	2/4	0.22									10:00:11.24	+02:15:05.6	2.58	25.27	23.60	1.65
	3/4	0.31									10:00:11.07	+02:15:04.7	3.15	25.49	23.45	1.88
	4/4	0.41									10:00:10.89	+02:15:07.1	3.80	26.08	22.93	1.44
450.215/850.27	1/2	0.01	10:00:23.69	+02:19:15.0	1.69	119 ± 17					10:00:23.67	+02:19:15.1	1.67	25.19	21.73	2.76
	3/3	0.38									10:00:23.66	+02:19:13.1	3.62	26.62	22.74	2.87
450.240/850.67	1/2	0.37									10:00:32.03	+02:33:28.1	3.53	28.88	23.08	2.73
	2/2	0.40									10:00:32.23	+02:33:27.8	3.72	25.63	22.48	2.64
450.247/850.151	1/2	0.15									10:00:41.42	+02:25:33.7	2.10	26.92	25.04	1.78
	2/2	0.18									10:00:41.35	+02:25:34.4	0.95	26.95	–	1.74
450.252/850.40	1/5	0.003	10:00:13.58	+02:22:25.6	2.78	605 ± 14	10:00:13.55	+02:22:25.7	2.43	88 ± 15	10:00:13.57	+02:22:25.4	2.52	23.10	19.95	–
	2/5	0.30									10:00:13.21	+02:22:23.6	3.11	25.70	23.68	–
	3/5	0.34									10:00:13.41	+02:22:21.4	3.33	23.81	23.66	–
	4/5	0.37									10:00:13.21	+02:22:26.7	3.55	24.31	23.57	–
	5/5	0.44									10:00:13.31	+02:22:21.1	3.94	26.19	24.18	–

Notes. All quantities are measured and given as in Table 5.

Scuba-2 position. Unfortunately, small number statistics on interferometric observations limit interpretation.

In the absence of interferometry, we can speculate that the reduced beamsize with respect to 850 μm would see a reduction in counterpart contamination proportional to the reduction in sky area searched for potential counterparts. The positional uncertainties of 450 μm range from 1.0 to 2.4 arcsec at $>3.6\sigma$ (with a median of ∼2.1 arcsec), while 850 μm positional uncertainties vary from 2 to 6 arcsec at $>3.6\sigma$ (median of 3.6 arcsec). This suggests the same counterpart identification strategy (when applied to 450 μm samples) should fail only ∼5 per cent of the time.

While this thought experiment gives a good ballpark figure for counterpart correctness, we can also use the individual source probabilities of correctness, given by the *p*-value to compute the likely number of incorrect counterparts. The likelihood of all 71 450 μm counterparts being correct (note that seven sources lack any counterparts) is ∼0.4 per cent, the probability of one contaminant is 2.7 per cent, the probability of two is 8 per cent, three is 15 per cent, four is 20 per cent, five is 20 per cent, six is 15 per cent, seven is 8 per cent, and higher than seven contaminants is 11 per cent likely. Therefore, we anticipate that 5–10 per cent of our 450 μm sample has incorrect counterpart matches; it is most likely the sources with incorrect counterparts are those with the highest *p*-values. While this emphasizes the importance of securing the correct counterparts for detailed follow-up on individual sources, this will not impact the bulk result of our analysis on the 450 μm population (in terms of redshift distribution, luminosities, etc.) significantly.

3.6 Multiplicity

The improved resolution from interferometry makes it clear that a potentially large fraction (20–50 per cent) of bright (>10 mJy) SMGs are actually multiples (Wang et al. 2011; Barger et al. 2012; Hodge et al. 2013). Although Scuba-2 is a bolometer array and not an interferometer, the high resolution at 450 μm can detect multiple sources when longer-wavelength observations only detect one SMG. This phenomenon is found once at high S/N in our sample, surrounding sources 450.16 and 450.28; the system is illustrated in Fig. 10. There is only one long-wavelength submillimetre source detected in this area: 850.05 in our sample, as well as COSBO3, detected at 1.2 mm (Bertoldi et al. 2007), and AzTEC/C6, detected at 1.1 mm (Aretxaga et al. 2011). However, we find two 450 μm sources within the Scuba-2 850 μm beam: 450.16 with a S/N of ∼4.6 and 450.28 with a S/N of ∼4.2. This is the best unequivocal identification of a multiple at 450 μm in our sample.

This demonstrates that shorter-wavelength, smaller beamsize bolometers can be used to probe SMG multiplicity in blank-field surveys at potentially lower observational cost than interferometric follow-up (e.g. future large-field surveys from LMT and CCAT).

4 DERIVED SOURCE CHARACTERISTICS

4.1 Redshift distributions

Fig. 11 shows the distributions of optical/NIR photometric redshifts (Ilbert et al. 2010) for the best-guess counterparts identified in Tables 5 and 7. Photometric redshifts span $0 < z < 5.1$, with most sources at $z < 3$. The median redshift for the 450 μm sample is $z = 1.95 \pm 0.19$ while the median for the 850 μm population is $z = 2.16 \pm 0.11$, in agreement with previous work at 850 μm (Chapman et al. 2005; Wardlow et al. 2011).

Table 7. Counterpart identifications and multiwavelength properties for SCUBA-2 850 μm detected sources.

Name	Counter-part no.	*p*-val	RA_{24}	DEC_{24}	δ_{24} (arcsec)	S_{24} (μJy)	$RA_{1.4}$	$DEC_{1.4}$	$\delta_{1.4}$ (arcsec)	$S_{1.4}$ (μJy)	RA_{opt}	DEC_{opt}	δ_{opt} (arcsec)	*i* (AB-mag)	3.6 μm (AB-mag)	z_{phot}
850.01	1/1	0.0008					09:59:57.30	+02:27:30.5	1.20	68 ± 13	**09:59:57.29**	**+02:27:30.1**	1.23	25.67	23.22	1.45
850.04	1/1	0.01	10:00:15.47	+02:15:50.5	1.78	123 ± 18					10:00:15.49	+02:15:50.2	1.43	23.83	20.72	1.39
850.05	1/2	0.02									10:00:57.02	+02:20:14.0	0.31	24.59	–	2.76
	2/2	0.19									10:00:57.01	+02:20:12.0	2.32	27.03	22.18	2.48
850.11	1/2	0.10									10:00:49.90	+02:22:58.8	1.71	25.83	22.08	2.77
	2/2	0.11									10:00:49.94	+02:22:55.4	1.82	27.02	24.07	2.68
850.13	1/3	0.002									10:00:24.12	+02:20:05.0	0.28	–	24.09	0.86
	2/3	0.21									10:00:24.27	+02:20:03.8	2.55	26.14	24.71	1.03
	3/3	0.22									10:00:24.08	+02:20:02.8	2.58	24.63	23.81	0.94
850.15	1/1	0.08									10:00:25.25	+02:26:05.9	1.50	21.70	20.25	–
850.16	1/1	0.002	10:01:03.92	+02:24:48.2	1.08	229 ± 18	10:01:03.91	+02:24:48.9	1.69	57 ± 10	10:01:03.92	+02:24:48.0	0.89	24.95	20.82	–
	2/2	0.18									10:01:03.83	+02:24:45.1	2.32	23.15	20.70	–
850.17	1/1	0.29									10:00:00.36	+02:22:56.3	1.26	26.09	–	–
850.18	1/2	0.01									10:00:24.02	+02:29:47.3	0.62	25.67	23.71	3.01
	2/2	0.27									10:00:24.04	+02:29:50.1	2.90	26.81	23.61	2.83
850.19	1/2	0.11									10:00:15.67	+02:24:45.5	1.76	26.87	24.99	2.24
	2/2	0.21									10:00:15.92	+02:24:46.8	2.51	27.43	23.17	3.61
850.20	1/1	0.18									10:00:27.13	+02:31:38.5	2.32	24.77	22.22	2.80
850.22	1/2	0.05	10:00:18.69	+02:16:51.9	3.38	300 ± 17					10:00:18.70	+02:16:52.5	2.72	25.50	20.40	2.06
	2/2	0.26									10:00:18.77	+02:16:58.0	2.83	27.05	24.11	2.29
850.24	1/1	0.0002	10:00:04.82	+02:30:45.3	0.51	321 ± 14	10:00:04.81	+02:30:45.2	0.55	96 ± 15	10:00:04.78	+02:30:45.2	1.00	27.21	20.82	3.51
850.25	1/5	0.0002	10:00:12.59	+02:14:44.1	0.20	331 ± 15					**10:00:12.58**	**+02:14:44.0**	0.20	24.09	20.31	2.33
	2/5	0.08									10:00:12.57	+02:14:42.7	1.52	23.67	20.79	2.78
	3/5	0.18									10:00:12.71	+02:14:45.6	2.30	26.28	22.99	2.61
	4/5	0.20									10:00:12.75	+02:14:43.9	2.44	26.27	23.01	2.32
	5/5	0.20									10:00:12.44	+02:14:43.1	2.45	25.83	22.14	2.75
850.29	1/2	0.03	10:00:50.18	+02:26:17.8	2.57	155 ± 18					10:00:50.15	+02:26:18.3	3.10	–	21.12	–
	2/2	0.02									10:00:50.15	+02:26:14.4	0.77	25.86	23.42	–
850.30	1/1	0.02	10:00:06.82	+02:22:07.4	1.89	186 ± 14					10:00:06.80	+02:22:07.5	1.71	20.94	20.61	0.23
	2/2	0.10									10:00:06.86	+02:22:11.6	2.64	25.36	23.80	–
850.31	1/1	0.02	10:00:26.17	+02:17:39.0	2.27	296 ± 44					10:00:26.18	+02:17:39.5	1.89	24.43	20.46	1.80
850.32	1/2	0.004	10:00:01.67	+02:24:27.9	2.73	287 ± 12	10:00:01.67	+02:24:28.3	2.52	90 ± 14	10:00:01.62	+02:24:28.0	2.02	27.53	21.71	1.95
	2/2	0.34									10:00:01.44	+02:24:28.4	1.40	25.07	–	1.58
850.35	1/2	0.06									10:01:05.07	+02:21:51.5	1.35	25.59	23.02	2.36
	2/2	0.23									10:01:05.15	+02:21:52.7	2.65	25.08	22.90	2.63
850.36	1/3	0.04	10:00:01.23	+02:17:42.4	3.08	127 ± 49					10:00:01.38	+02:17:42.4	2.96	24.20	20.42	2.05
	2/3	0.13									10:00:01.21	+02:17:43.9	1.94	20.88	21.44	0.22
	3/3	0.13									10:00:01.44	+02:17:45.2	1.97	24.09	21.70	2.04
850.37	1/3	0.12									10:00:35.70	+02:28:27.4	1.84	28.03	23.31	4.57
	2/3	0.15									10:00:35.68	+02:28:28.0	2.08	27.96	23.31	3.99
	3/3	0.27									10:00:35.54	+02:28:29.0	2.92	28.41	23.98	3.53
850.38	1/4	0.07									10:00:23.45	+02:15:35.5	1.39	24.90	22.75	2.04
	2/4	0.08									10:00:23.58	+02:15:37.5	1.50	26.39	23.01	2.72
	3/4	0.14									10:00:23.63	+02:15:35.0	1.99	27.04	24.92	2.58
	4/4	0.22									10:00:23.36	+02:15:36.4	2.60	26.60	23.31	2.43
850.39	1/2	0.01									10:00:12.21	+02:23:09.8	0.62	26.48	24.32	–
	2/2	0.18									10:00:12.16	+02:23:07.9	2.31	24.76	23.20	–
850.43	1/1	0.12									10:00:26.31	+02:15:29.0	0.77	–	–	0.84
850.44	1/3	0.007	10:00:18.32	+02:22:50.0	1.24	128 ± 16					10:00:18.29	+02:22:51.0	1.81	25.03	22.78	2.48
	2/3	0.11									10:00:18.16	+02:22:50.3	1.79	23.27	21.41	2.56
	3/3	0.14									10:00:18.33	+02:22:47.5	2.06	27.58	23.56	2.03

Table 7 – *continued*

Name	Counter-part no.	*p-val*	RA_{24}	DEC_{24}	δ_{24} (arcsec)	S_{24} (μJy)	$RA_{1.4}$	$DEC_{1.4}$	$\delta_{1.4}$ (arcsec)	$S_{1.4}$ (μJy)	RA_{opt}	DEC_{opt}	δ_{opt} (arcsec)	*i* (AB-mag)	3.6 μm (AB-mag)	z_{phot}
850.45	1/1	0.06	10:00:06.75	+02:20:44.7	3.52	105 ± 33					10:00:06.78	+02:20:44.8	3.07	24.22	21.03	1.32
850.46	1/1	0.0006	10:00:25.54	+02:15:05.9	1.12	560 ± 17	10:00:25.52	+02:15:05.8	1.01	112 ± 10	10:00:25.51	+02:15:06.1	0.65	26.03	20.78	3.04
850.50	1/3	0.009					10:00:08.97	+02:20:26.5	3.92	62 ± 12	10:00:09.11	+02:20:26.4	3.20	26.07	23.73	2.38
	2/3	0.02									10:00:09.17	+02:20:23.2	0.78	25.06	22.90	1.97
	3/3	0.24									10:00:08.96	+02:20:24.7	2.71	26.43	23.47	2.87
850.51	1/4	0.007	09:59:56.41	+02:18:53.0	1.23	193 ± 15					09:59:56.39	+02:18:52.7	1.66	24.39	20.82	1.11
	2/4	0.23									09:59:56.32	+02:18:56.2	2.64	25.18	22.04	1.09
	3/4	0.26									09:59:56.56	+02:18:56.5	2.89	21.06	19.07	0.66
	4/4	0.29									09:59:56.63	+02:18:53.3	3.04	25.46	22.37	1.02
850.54	1/1	0.02									09:59:48.89	+02:27:48.9	0.71	26.82	23.91	3.07
850.56	NA															
850.57	1/4	0.0003	10:00:06.90	+02:33:08.1	1.20	592 ± 184	10:00:06.82	+02:33:07.9	0.75	82 ± 14	–	–	–	–	–	–
	2/4	0.13									10:00:06.81	+02:33:05.4	1.94	23.93	22.89	0.50
	3/4	0.20									10:00:06.68	+02:33:07.2	2.49	20.13	18.28	0.74
	4/4	0.21									10:00:07.01	+02:33:07.2	2.51	24.78	21.95	1.51
850.59	1/4	0.007	10:00:00.80	+02:20:02.4	1.21	85 ± 13					10:00:00.84	+02:20:02.4	1.60	26.08	24.06	3.15
	2/4	0.15									10:00:00.92	+02:20:01.2	2.13	26.18	24.01	2.64
	3/4	0.16									10:00:00.77	+02:20:03.4	2.15	24.22	21.79	2.97
	4/4	0.23									10:00:00.60	+02:20:00.8	2.69	24.59	22.85	0.97
850.60	1/2	0.03	10:00:00.86	+02:27:41.2	2.54	239 ± 14					10:00:00.82	+02:27:41.3	2.03	24.38	19.74	1.44
	2/2	0.10									10:00:00.81	+02:27:39.6	1.69	26.20	22.12	2.75
850.61	1/1	0.06									10:00:01.96	+02:28:20.8	1.34	23.88	22.16	0.53
850.63	1/3	0.08									09:59:53.47	+02:18:50.6	1.55	25.87	23.90	1.89
	2/3	0.30									09:59:53.36	+02:18:48.9	1.27	25.40	–	2.35
	3/3	0.36									09:59:53.32	+02:18:51.4	1.43	–	–	–
850.64	1/3	0.04									10:00:00.72	+02:21:37.5	1.10	26.44	24.01	3.39
	2/3	0.05									10:00:00.66	+02:21:36.1	1.19	24.90	23.58	2.53
	3/3	0.28									10:00:00.84	+02:21:36.6	3.01	27.94	23.18	4.12
850.65	1/2	0.06	10:00:59.10	+02:21:11.4	3.68	172 ± 15					10:00:59.04	+02:21:11.1	4.09	23.33	21.76	0.48
	2/2	0.13									10:00:59.13	+02:21:09.6	1.97	23.02	21.30	1.27
850.66	1/5	0.09									10:00:24.46	+02:28:30.0	1.60	24.98	23.96	0.94
	2/5	0.19									10:00:24.44	+02:28:33.5	2.36	25.76	23.26	2.47
	3/5	0.21									10:00:24.56	+02:28:30.6	2.56	23.58	23.62	0.36
	4/5	0.21									10:00:24.23	+02:28:31.7	2.54	26.76	24.77	1.52
	5/5	0.31									10:00:24.32	+02:28:34.2	3.16	26.58	23.31	2.26
850.68	1/4	0.05	09:59:55.30	+02:19:51.1	3.13	218 ± 14					09:59:55.26	+02:19:51.2	3.09	25.31	20.47	1.95
	2/4	0.02									09:59:55.31	+02:19:53.5	0.71	26.22	21.78	2.04
	3/4	0.11									09:59:55.31	+02:19:56.0	1.78	24.09	22.27	0.93
	4/4	0.30									09:59:55.10	+02:19:53.4	3.14	27.59	23.11	2.30
850.69	1/1	0.06	10:00:43.66	+02:28:55.6	3.66	142 ± 15					10:00:43.64	+02:28:55.3	4.15	25.60	21.28	1.80
850.70	1/1	0.005	10:00:20.01	+02:30:19.5	1.00	119 ± 15					10:00:20.07	+02:30:19.3	0.96	23.46	20.56	0.78
	2/2	0.29									10:00:20.24	+02:30:21.5	3.03	26.66	23.75	2.46
850.71	1/2	0.24									09:59:44.05	+02:21:06.3	1.12	27.01	–	2.17
	2/2	0.08									09:59:43.99	+02:21:03.8	1.51	24.55	24.13	0.90
850.72	1/4	0.04	10:00:13.69	+02:17:34.2	3.06	150 ± 13					10:00:13.70	+02:17:34.8	3.62	–	–	–
	2/4	0.21									10:00:13.73	+02:17:28.9	2.55	–	24.84	0.93
	3/4	0.23									10:00:13.81	+02:17:32.6	2.67	25.64	23.40	2.08
	4/4	0.26									10:00:13.47	+02:17:32.2	2.88	25.48	24.22	1.82
850.73	1/5	0.04	10:00:20.52	+02:22:49.2	2.93	112 ± 26					10:00:20.48	+02:22:48.6	3.80	26.48	22.48	3.91
	2/5	0.005									10:00:20.63	+02:22:51.2	0.38	25.75	22.90	1.82
	3/5	0.02									10:00:20.70	+02:22:51.3	0.67	25.07	23.14	1.65

Table 7 – *continued*

Name	Counter-part no.	*p-val*	RA_{24}	DEC_{24}	δ_{24} (arcsec)	S_{24} (μJy)	$RA_{1.4}$	$DEC_{1.4}$	$\delta_{1.4}$ (arcsec)	$S_{1.4}$ (μJy)	RA_{opt}	DEC_{opt}	δ_{opt} (arcsec)	*i* (AB-mag)	3.6 μm (AB-mag)	z_{phot}
	4/5	0.14									10:00:20.69	+02:22:53.2	1.99	25.59	22.43	2.50
	5/5	0.15									10:00:20.69	+02:22:49.1	2.16	25.13	23.59	1.67
850.74	1/1	0.25									10:00:05.41	+02:14:47.1	2.78	27.42	23.87	2.76
850.75	1/4	0.007					10:00:26.97	+02:22:30.5	3.64	82 ± 16	10:00:26.96	+02:22:30.8	3.40	25.86	21.91	–
	2/4	0.05									10:00:26.79	+02:22:31.1	1.20	26.69	23.28	–
	3/4	0.25									10:00:26.91	+02:22:29.3	2.81	25.99	23.05	–
	4/4	0.34									10:00:26.52	+02:22:29.4	3.34	25.59	23.43	–
850.76	1/2	0.08									10:00:48.95	+02:30:24.88	1.62	24.31	22.94	1.06
	2/2	0.31									10:00:48.82	+02:30:21.00	3.08	23.22	22.61	0.86
850.77	1/1	0.12	10:00:05.47	+02:29:53.1	5.17	441 ± 178					–	–	–	–	–	–
850.78	1/6	0.08	10:00:08.77	+02:19:16.2	4.11	207 ± 14					10:00:08.93	+02:19:16.2	5.07	22.89	21.18	0.94
	2/6	0.11									10:00:08.78	+02:19:13.8	1.82	25.98	24.27	2.39
	3/6	0.22									10:00:08.88	+02:19:11.4	2.58	29.41	–	3.24
	4/6	0.29									10:00:08.66	+02:19:13.2	1.26	–	–	0.71
	5/6	0.31									10:00:08.73	+02:19:15.4	3.19	26.46	22.75	4.35
	6/6	0.32									10:00:08.67	+02:19:09.0	3.26	27.65	23.83	2.94
850.79	1/3	0.001									10:01:02.28	+02:22:34.1	0.20	21.39	20.55	–
	2/3	0.18									10:01:02.14	+02:22:34.1	2.29	23.34	22.20	–
	3/3	0.26									10:01:02.27	+02:22:37.0	2.83	23.99	23.40	–
850.80	1/3	0.16									10:00:14.13	+02:27:02.1	2.15	25.23	22.72	3.54
	2/3	0.17									10:00:14.26	+02:27:03.3	2.28	24.07	23.74	2.40
	3/3	0.31									10:00:13.99	+02:27:01.7	3.19	26.74	23.94	3.87
850.81	1/2	0.06									09:59:59.12	+02:24:41.9	1.35	24.11	23.58	0.40
	2/2	0.47									09:59:58.97	+02:24:39.8	1.73	26.81	–	2.81
850.82	1/1	0.03	10:00:54.96	+02:19:47.4	2.46	203 ± 17					10:00:54.95	+02:19:47.1	2.09	26.03	21.11	2.87
850.84	1/1	0.22									10:00:41.67	+02:21:12.7	2.58	26.85	24.03	2.42
850.86	1/2	0.005	10:01:01.30	+02:24:39.4	1.04	299 ± 19					10:01:01.27	+02:24:39.9	1.51	23.28	20.03	–
	2/2	0.10									10:01:01.31	+02:24:37.6	1.73	21.73	19.55	–
850.87	1/2	0.05	10:00:40.23	+02:17:55.5	3.18	284 ± 15					10:00:40.26	+02:17:55.7	2.85	26.99	20.78	2.24
	2/2	0.11									10:00:40.33	+02:18:00.0	1.75	26.48	22.91	1.45
850.89	1/4	0.02	10:00:20.26	+02:17:25.1	2.12	401 ± 16					10:00:20.25	+02:17:25.7	1.53	22.53	19.94	–
	2/4	0.04									10:00:20.19	+02:17:27.0	1.00	25.42	22.16	1.87
	3/4	0.11									10:00:20.24	+02:17:29.0	1.79	25.72	23.02	1.72
	4/4	0.20									10:00:20.37	+02:17:28.9	2.43	24.88	23.21	0.92
850.91	1/3	0.18									10:00:27.85	+02:25:51.9	2.30	26.95	23.91	2.71
	2/3	0.26									10:00:27.94	+02:25:51.6	2.84	26.73	24.91	2.21
	3/3	0.46									10:00:27.76	+02:25:55.1	1.69	25.95	–	2.68
850.93	1/3	0.01					10:00:57.06	+02:29:42.9	4.97	123 ± 10	10:00:57.06	+02:29:42.8	5.08	24.47	20.88	–
	2/3	0.09									10:00:56.66	+02:29:44.7	1.59	25.82	24.76	–
	3/3	0.32									10:00:56.69	+02:29:48.3	3.23	21.25	20.79	0.37
850.94	1/2	0.002	10:00:02.62	+02:16:34.0	1.84	393 ± 16	10:00:02.61	+02:16:33.8	1.65	72 ± 11	10:00:02.61	+02:16:34.2	2.03	24.62	20.29	2.04
	2/2	0.006									10:00:02.62	+02:16:32.1	0.39	25.70	22.38	4.16
850.95	1/3	0.02	09:59:59.82	+02:27:06.6	1.88	387 ± 67					09:59:59.80	+02:27:07.4	2.74	22.78	19.60	1.55
	2/3	0.13									09:59:59.82	+02:27:03.7	1.94	–	19.82	0.74
	3/3	0.32									09:59:59.93	+02:27:02.0	3.21	–	21.05	–
850.97	1/3	0.005					10:00:13.57	+02:18:05.0	2.87	148 ± 15	10:00:13.59	+02:18:05.1	3.00	20.46	18.63	0.73
	2/3	0.03	10:00:13.60	+02:18:08.6	2.62	349 ± 15					10:00:13.59	+02:18:08.5	2.40	24.02	21.12	1.48
	3/3	0.25									10:00:13.29	+02:18:08.7	2.82	25.22	22.91	1.80
850.98	1/1	0.19									10:00:14.49	+02:30:10.1	2.37	–	19.02	–

Notes. All quantities are measured and given as in Table 5. Sources which have 450 μm counterparts are excluded from this table as their 450 μm positional uncertainty is smaller than their 850 μm uncertainty; the former is used to determine their counterparts which are given in either Table 5 or Table 6. Source 850.22 is in bold text in this table to indicate it was interferometrically observed by Smolčić et al. (2012); however no source was detected; it is likely that the reason for this is that the submillimetre emission emanates from multiple possible counterparts.

Table 8. Identification of SCUBA-2 sources at 870 μm–1.2 mm.

450 μm name	850 μm name	Alternate name	λ_{obs} (mm)	S_λ (mJy)	Interferometric?	Inst./ Tel	Reference
450.00	850.07	AzTEC J100028.94+023200.3	1.1	3.8 ± 0.9		AzTEC	Scott et al. (2008)
450.01	850.02	AzTEC/C80	1.1	4.1 ± 0.9		AzTEC	Aretxaga et al. (2011)
		COSLA-47	0.87	9.0 ± 2.8		LABOCA	Navarette et al. in prep
		COSLA-47	1.3	3.11 ± 0.59	Y	PdBI	Smolčić et al. (2012)
450.03	850.00	AzTEC J100008.03+022612.1	1.1	8.3 ± 1.1		AzTEC	Scott et al. (2008)
		AzTEC-2	0.89	12.4 ± 1.0	Y	SMA	Younger et al. (2007, 2009)
		AzTEC/C3	1.1	10.5 ± 1.0		AzTEC	Aretxaga et al. (2011)
450.04	850.03	AzTEC J100019.73+023206.0	1.1	6.5 ± 1.3		AzTEC	Scott et al. (2008)
		AzTEC-5	0.89	9.3 ± 1.3	Y	SMA	Younger et al. (2007, 2009)
		AzTEC/C42	1.1	4.8 ± 1.1		AzTEC	Aretxaga et al. (2011)
450.05	850.08	AzTEC/C38	1.1	5.1 ± 1.0		AzTEC	Aretxaga et al. (2011)
		COSLA-35	0.87	8.2 ± 2.2		LABOCA	Navarette et al. in prep
		COSLA-35	1.3	2.15 ± 0.51	Y	PdBI	Smolčić et al. (2012)
450.07	850.98	AzTEC/C169	1.1	3.1 ± 0.8		AzTEC	Aretxaga et al. (2011)
450.08	850.46	COSLA-8	0.87	6.9 ± 1.6		LABOCA	Navarette et al. in prep
		COSLA-8	1.3	2.65 ± 0.62	Y	PdBI	Smolčić et al. (2012)
450.16		COSBO3**	1.2	7.4 ± 1.1		MAMBO	Bertoldi et al. (2007)
		AzTEC/C6**	1.1	9.6 ± 1.0		AzTEC	Aretxaga et al. (2011)
450.20	850.24	AzTEC J100004.54+023040.1	1.1	3.3 ± 0.8		AzTEC	Scott et al. (2008)
		AzTEC/C150	1.1	3.3 ± 1.2		AzTEC	Aretxaga et al. (2011)
450.27	850.115	AzTEC/C65	1.1	4.4 ± 1.0		AzTEC	Aretxaga et al. (2011)
450.28	850.05	COSBO3**	1.2	7.4 ± 1.1		MAMBO	Bertoldi et al. (2007)
		AzTEC/C6**	1.1	9.6 ± 1.0		AzTEC	Aretxaga et al. (2011)
450.38	850.14	AzTEC/C24	1.1	5.7 ± 1.0		AzTEC	Aretxaga et al. (2011)
450.55	850.06	COSBO7	1.2	5.0 ± 0.9		MAMBO	Bertoldi et al. (2007)
		AzTEC/C160	1.1	3.1 ± 1.2		AzTEC	Aretxaga et al. (2011)
450.66	850.146	AzTEC/C66	1.1	4.3 ± 0.9		AzTEC	Aretxaga et al. (2011)
	850.01	AzTEC J095957.22+022729.3	1.1	5.8 ± 1.0		AzTEC	Scott et al. (2008)
		AzTEC-9	0.89	13.5 ± 1.8	Y	SMA	Younger et al. (2007, 2009)
		AzTEC/C18	1.1	7.9 ± 1.5		AzTEC	Aretxaga et al. (2011)
	850.04	COSBO1	1.2	6.2 ± 0.9		MAMBO	Bertoldi et al. (2007)
		AzTEC/C7	1.1	8.9 ± 1.1		AzTEC	Aretxaga et al. (2011)
	850.13	AzTEC/C114	1.1	3.7 ± 0.9		AzTEC	Aretxaga et al. (2011)
	850.15	AzTEC J100025.23+022608.0	1.1	1.9 ± 0.6		AzTEC	Scott et al. (2008)
		AzTEC/C30	1.1	5.5 ± 1.1		AzTEC	Aretxaga et al. (2011)
	850.18	AzTEC J100023.98+022950.0	1.1	2.6 ± 0.7		AzTEC	Scott et al. (2008)
	850.20	AzTEC J100026.68+023128.1	1.1	2.8 ± 0.8		AzTEC	Scott et al. (2008)
	850.22	COSLA-50	0.87	5.6 ± 1.6		LABOCA	Navarette et al. in prep
		COSLA-50	1.3	...	Y	PdBI	Smolčić et al. (2012)
		AzTEC/C33	1.1	5.3 ± 1.1		AzTEC	Aretxaga et al. (2011)
	850.25	COSBO19	1.2	3.0 ± 0.8		MAMBO	Bertoldi et al. (2007)
		COSLA-38	0.87	5.8 ± 1.6		LABOCA	Navarette et al. in prep
		COSLA-38	1.3	8.19 ± 1.85	Y	PdBI	Smolčić et al. (2012)
450.99	850.33	AzTEC J095950.69+022829.5	1.1	3.6 ± 0.9		AzTEC	Scott et al. (2008)
	850.35	AzTEC/C74	1.1	4.2 ± 0.9		AzTEC	Aretxaga et al. (2011)
	850.50	AzTEC/C35	1.1	5.2 ± 1.0		AzTEC	Aretxaga et al. (2011)
	850.57	AzTEC/C45	1.1	4.8 ± 1.0		AzTEC	Aretxaga et al. (2011)
450.78	850.62	AzTEC J100031.06+022751.5	1.1	2.7 ± 0.8		AzTEC	Scott et al. (2008)
	850.63	COSBO36	1.2	5.7 ± 1.3		MAMBO	Bertoldi et al. (2007)
		AzTEC/C71	1.1	4.3 ± 1.1		AzTEC	Aretxaga et al. (2011)
	850.94	COSBO29	1.2	3.1 ± 1.0		MAMBO	Bertoldi et al. (2007)
		AzTEC/C162	1.1	3.1 ± 1.2		AzTEC	Aretxaga et al. (2011)

Notes. Counterparts of SCUBA-2 sources at 870 μm–1.2 mm as identified by LABOCA, PdBI, AzTEC, SMA and MAMBO with given references. Sources are divided into 450 μm $>3.6\sigma$ and 850 μm $>3.6\sigma$ samples. None of the marginal $3 < \sigma < 3.6$ 450 μm/850 μm sources was reported as detections in the given references. Sources are searched within a 10 arcsec (450 μm sources) or 12 arcsec (850 μm sources) search radius; this is approximately one beamsize at ∼850 μm–1.2 mm and represents a regime where chance coincidence between submm sources is very low ($p - value < 0.01$). Flux densities (S_λ) are deboosted and not raw. Sources marked with ** correspond to multiple SCUBA-2 sources in the table, i.e. 450.16, 450.28 and 850.05 all correspond to COSBO3/AzTEC/C6.

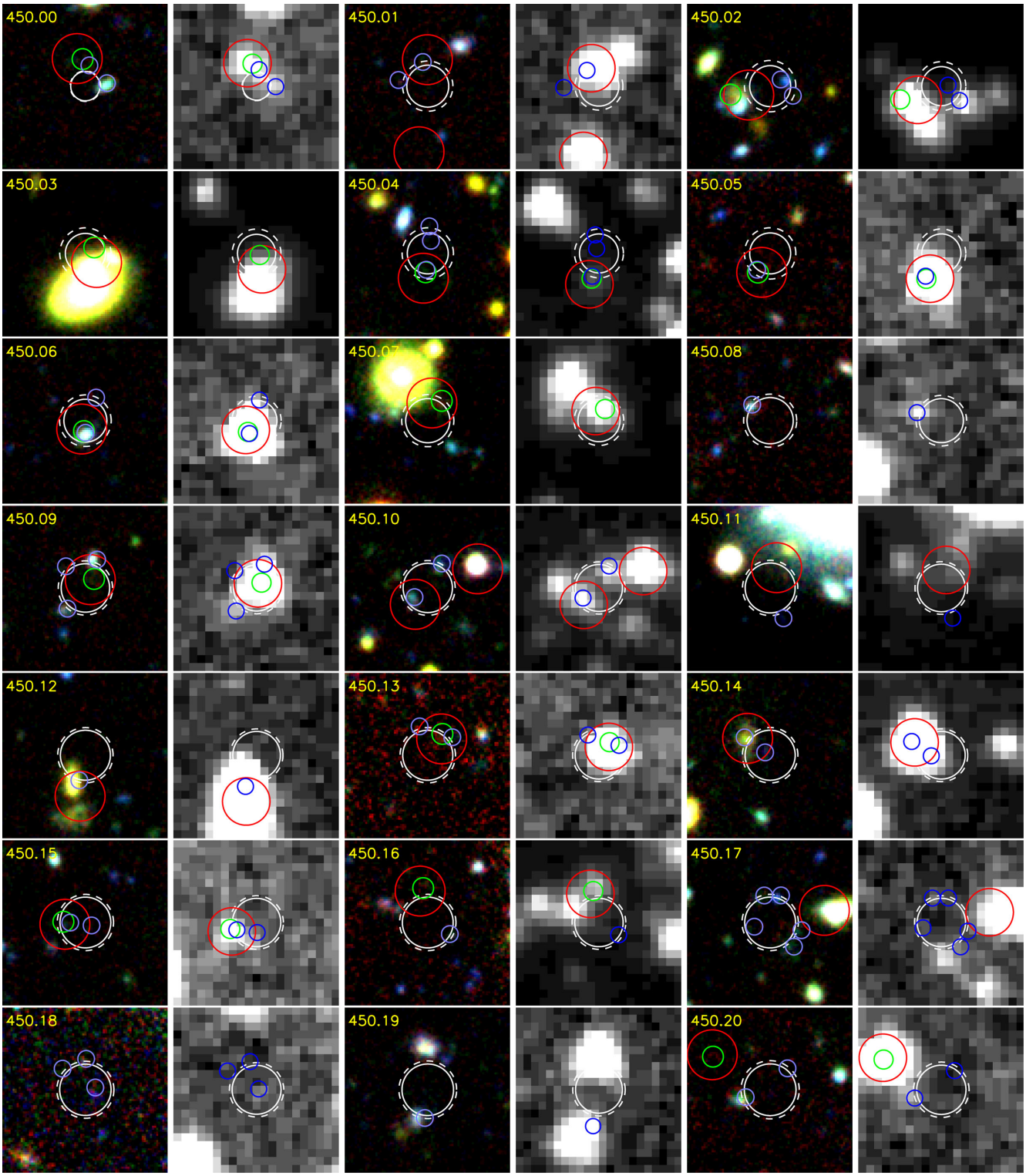

Figure 9. 12 × 12 arcsec^2 cutouts for 450 μm detected sources in optical tri-colour (SUBARU B, I and Z) and *Spitzer*-IRAC 3.6 μm. White solid circles indicate the position of the 450 μm source with associated positional uncertainty, varying 1.5–3 arcsec. The outer ring (white dashed circle) corresponds to the 95 per cent confidence interval on position, while the inner is the 90 per cent interval. *Spitzer*-MIPS 24 μm source positions are marked with red circles and 1.4 GHz source positions are marked with green circles. Optical counterparts are marked with blue circles.

The uncertainties on the median are generated via bootstraping methods.

At 850 μm, we split our sample by its potential biases. The increased beamsize of 850 μm observations means that 850 μm sources which lack 24 μm or radio identifications have more uncertain counterparts. We illustrate the distribution of redshifts for the 24 μm/radio identified subset, then those without (dashed area) and finally those from the $3 < \sigma < 3.6$ marginal catalogue. Note that

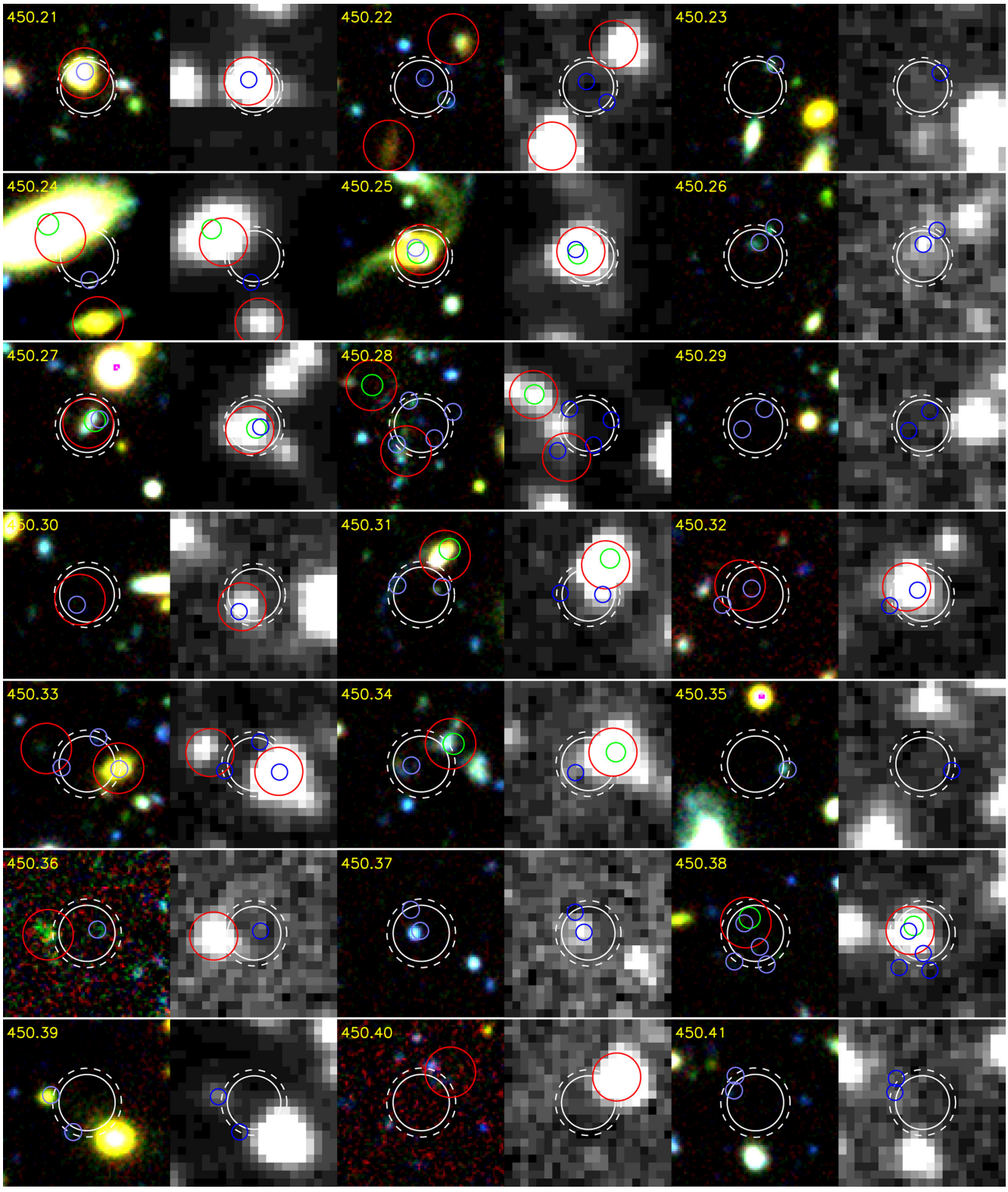

Figure 9 – *continued*

the number of sources lacking redshift identifications is ≈18–21 (amounting to 21–23 per cent) of either sample.

Are those sources without photometric redshifts intrinsically different from those with photometric redshifts? We investigate this by seeing if the FIR properties, i.e. S_{850} to S_{450} colour, (a) evolves with redshift, or (b) differs between the sample of galaxies with photometric redshifts and without. Fig. 12 plots the FIR colour of both $>3.6\sigma$ samples against photometric redshift and in histogram

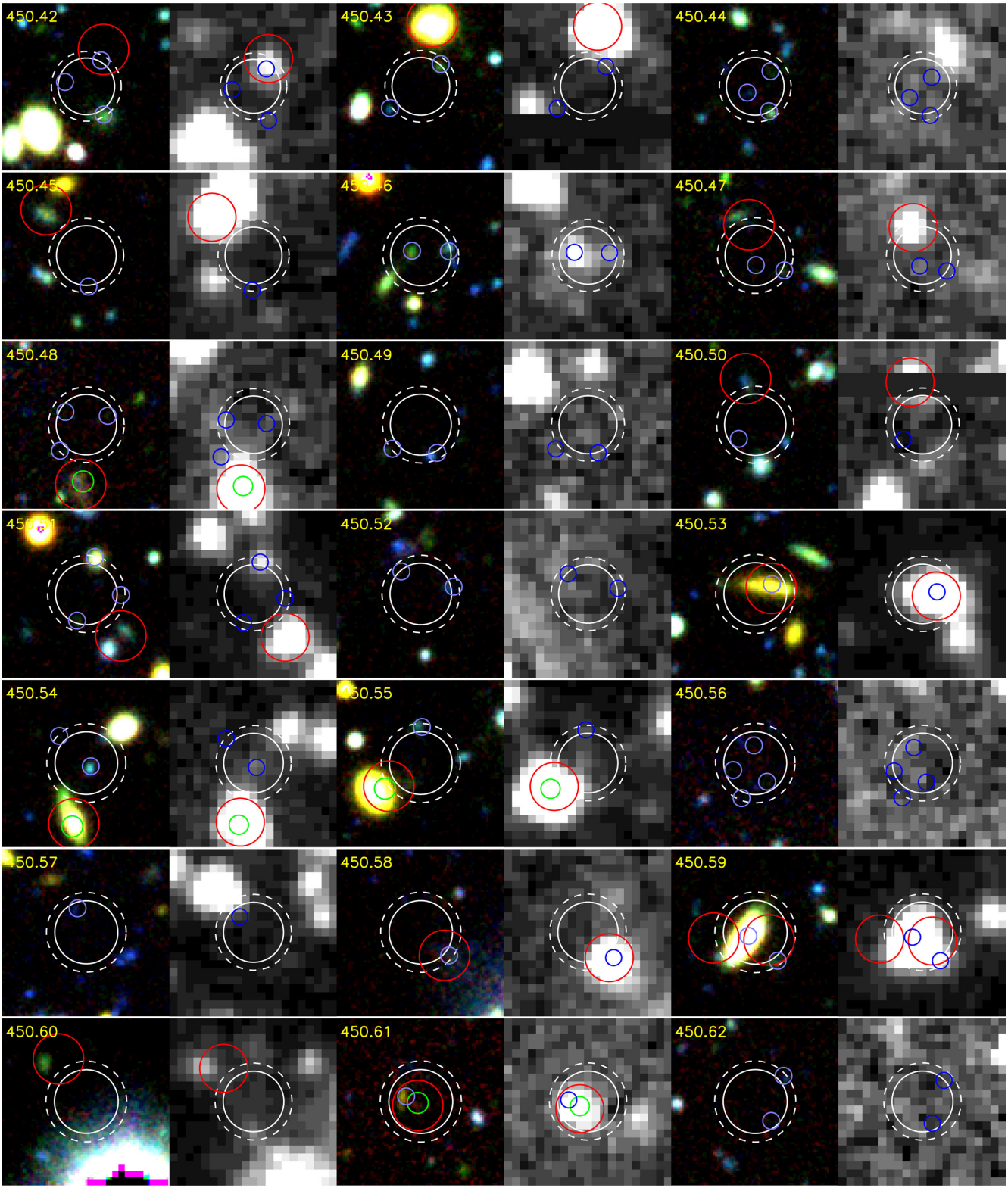

Figure 9 – *continued*

form. As expected, 450 μm sources are much brighter at 450 μm than 850 μm and vice versa. There is some shallow evolution of the log (S_{850}/S_{450}) colour with redshift, although the statistical variation within subsamples dominates. As we find that sources display a wide range of FIR properties irrespective of redshift, this does not necessarily bode well for work which makes use of FIR photometric redshifts which assume a certain FIR template with fixed temperature and use FIR photometry to estimate the redshift more precisely

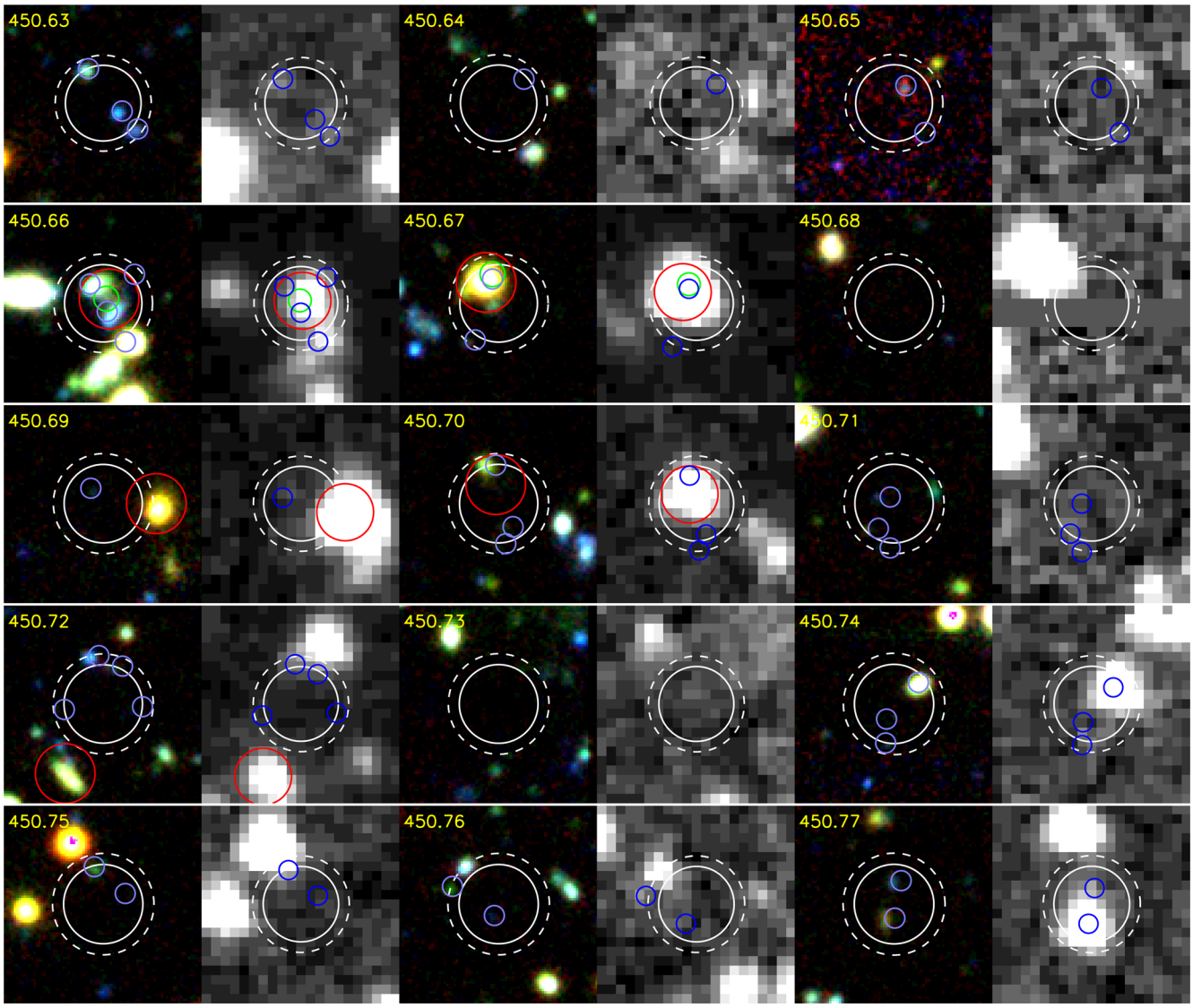

Figure 9 – *continued*

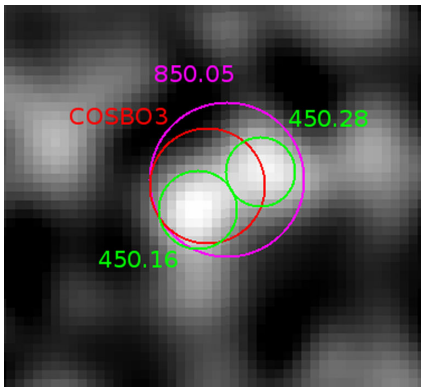

Figure 10. A 35 × 40 arcsec 450 μm S/N map cutout of 450.16 and 450.28. The 450 μm sources are circled and labelled in green, while COSBO3, the MAMBO-detected 1.2 mm source is shown in red and the 850 μm SCUBA-2 source, 850.05, is shown in magenta. The beamsizes at 450 μm, 850 μm and 1.2 mm are 7 arcsec, 15 arcsec and 11 arcsec, respectively.

than $\Delta z \sim 2$ (some work using this technique include Barger et al. 2012; Roseboom et al. 2012; Chen et al. 2013, but often under specific luminosity restrictions, not broadly applicable to a wide range of high-z ULIRGs). Furthermore, sources which do not have photometric redshifts show roughly the same distribution in FIR colour as the parent population of galaxies they are selected from. This suggests that the systems lacking photometric redshifts are not intrinsically biased with FIR properties. While there is significant variation in SED shape, the differences between the measured medians for 450 μm and 850 μm samples (measured by uncertainty of the median) are statistically significant at $>5\sigma$ at $z \lesssim 2$ and $\sim 3\sigma$ at $z \sim 3$.

It is difficult to say if sources without photometric redshifts differ significantly from those with redshift estimates. Wardlow et al. (2011) estimate the redshift distribution of 870 μm sources in CDFS without photometric redshifts using the density of IRAC 3.6 μm emitters, and guess that they largely sit at $z \sim 2.5$, near the expected peak of the whole population. The SCUBA2 population is likely similar to the 870 μm galaxies from Wardlow et al. (2011), although

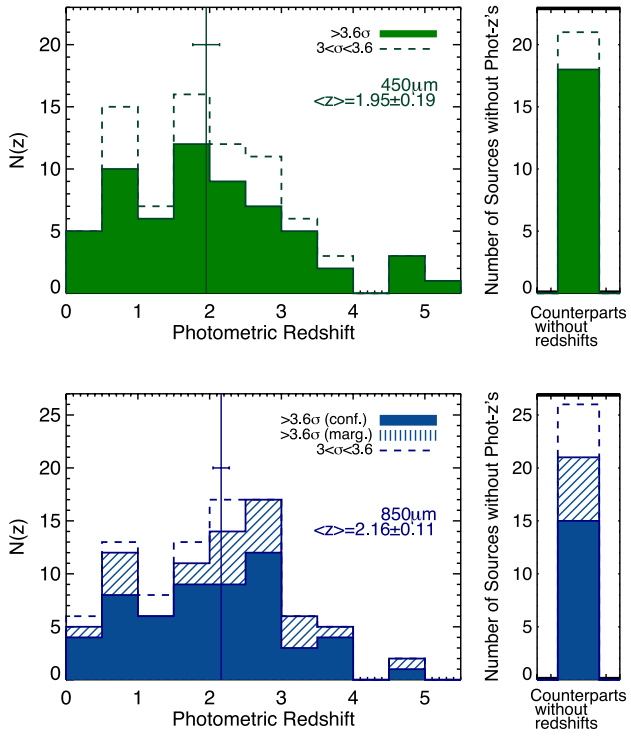

Figure 11. The distribution in photometric redshift for SCUBA-2 sources identified at 450 μm (green) and 850 μm (blue). The median redshifts of the two samples are $\langle z \rangle = 1.95$ and $\langle z \rangle = 2.16$, respectively. At 450 μm, we illustrate two distributions, the first consisting of just $>3.6\sigma$ 450 μm sources (solid green shaded region), and the second of the $3<\sigma<3.6$ sample (dashed green line). We also indicate the number of sources without photometric redshifts at right. Due to the larger beamsize at 850 μm, our counterpart matching is done first using 24 μm, radio or 450 μm identification (solid blue shaded region). The remaining 850 μm SMGs without 24 μm/radio/450 μm counterparts are shown in the hashed region. The dashed blue line corresponds to the $3 < \sigma < 3.6$ sample. The median redshifts are marked with vertical lines and 1σ bootstrap uncertainty on the median.

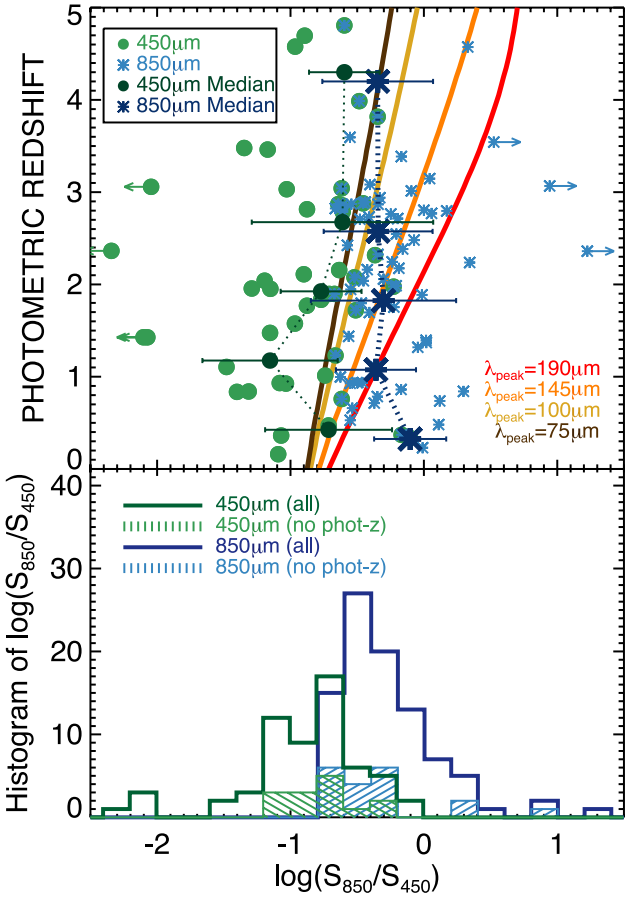

Figure 12. The FIR colour properties of the SCUBA-2 sample, measured as $\log(S_{850}/S_{450})$. At top, we plot against the optical/NIR photometric redshift. Sources with arrows represent galaxies which have flux densities close to zero in one band or the other; sources with negative flux densities are not included here. The 450 μm sample (green) has, on average, 450 μm flux densities which exceed 850 μm flux densities by a factor of 5, while the 850 μm sample (blue) has naturally 'redder' colours. Median values, binned by redshift, are shown in dark green/blue with deviations in the population indicated by error bars (the uncertainties in the median are much smaller ∼0.05–0.08 dex). Slight redshift evolution is seen in the median. We overplot evolution of constant temperature (or constant SED peak wavelength) and note that our samples are inconsistent with non-evolving SED shape (i.e. the dust temperatures of high redshift, more luminous sources are much higher than they are at low redshift). At bottom, we plot the distribution in FIR colour for both samples with the subset of the samples which do not have any photometric redshift. The distribution of colours for the samples without redshifts resembles the parent population, indicating no obvious redshift–colour bias.

only spectroscopic confirmation will unequivocally reveal their true nature.

4.2 Infrared luminosities and dust properties

We can go beyond basic FIR colour comparisons with our SCUBA-2 data and use SED fits to measure infrared luminosities, temperatures and in some cases dust masses. Simple greybody SED fitting combined with a MIR power law gives us this information with a minimum number of free parameters or model assumptions. We fit all available infrared photometry, from 24 μm MIPS, 70 μm MIPS, 450 μm SCUBA-2, 850 μm SCUBA-2, 870 μm LABOCA, 1.1 mm AzTEC, 1.2 mm MAMBO and 1.3 mm PdBI.

The combination of a greybody and MIR power law accounts for both galaxy-wide cold dust emission and smaller-scale warm dust emission (Blain, Barnard & Chapman 2003; Kovács et al. 2006). The fitting method is described in full in Casey (2012) and is represented by the equation

$$S_\nu = N_{\rm bb}\frac{(1-e^{-(\nu/\nu^0)^\beta})\nu^3}{e^{h\nu/kT}-1} + N_{\rm pl}(c/\nu)^\alpha e^{-(\nu_c/\nu)^2} \quad (3)$$

where S_ν is flux density (in units of mJy), T is greybody dust temperature, β is the emissivity index of the greybody, α is the MIR power-law slope, and $N_{\rm bb}$ and $N_{\rm pl}$ are the normalizations of the greybody and power law, respectively ($N_{\rm pl}$ is a fixed function of $N_{\rm bb}$, T and α). Note, however, that in this work we do not quote our best-fitting temperatures since they are heavily dependent on the assumed opacity and emissivity model. For example, an SED peaking at 100 μm can be described as 29 K (blackbody), 31 K (optically thin greybody), 44 K (greybody with $\tau = 1$ at 100 μm), or 46 K (greybody with $\tau = 1$ at 200 μm). All of these models have been used in the literature to derive dust temperature despite the fact that they are not directly comparable (e.g. Blain et al. 2003; Coppin et al. 2008; Casey et al. 2009a; Hwang et al. 2010; Kovács et al. 2010); see Casey (2012), fig. 2, for more details on the impact of model assumption on measured dust temperature. Instead of estimating temperatures, we estimate the rest-frame SED peak

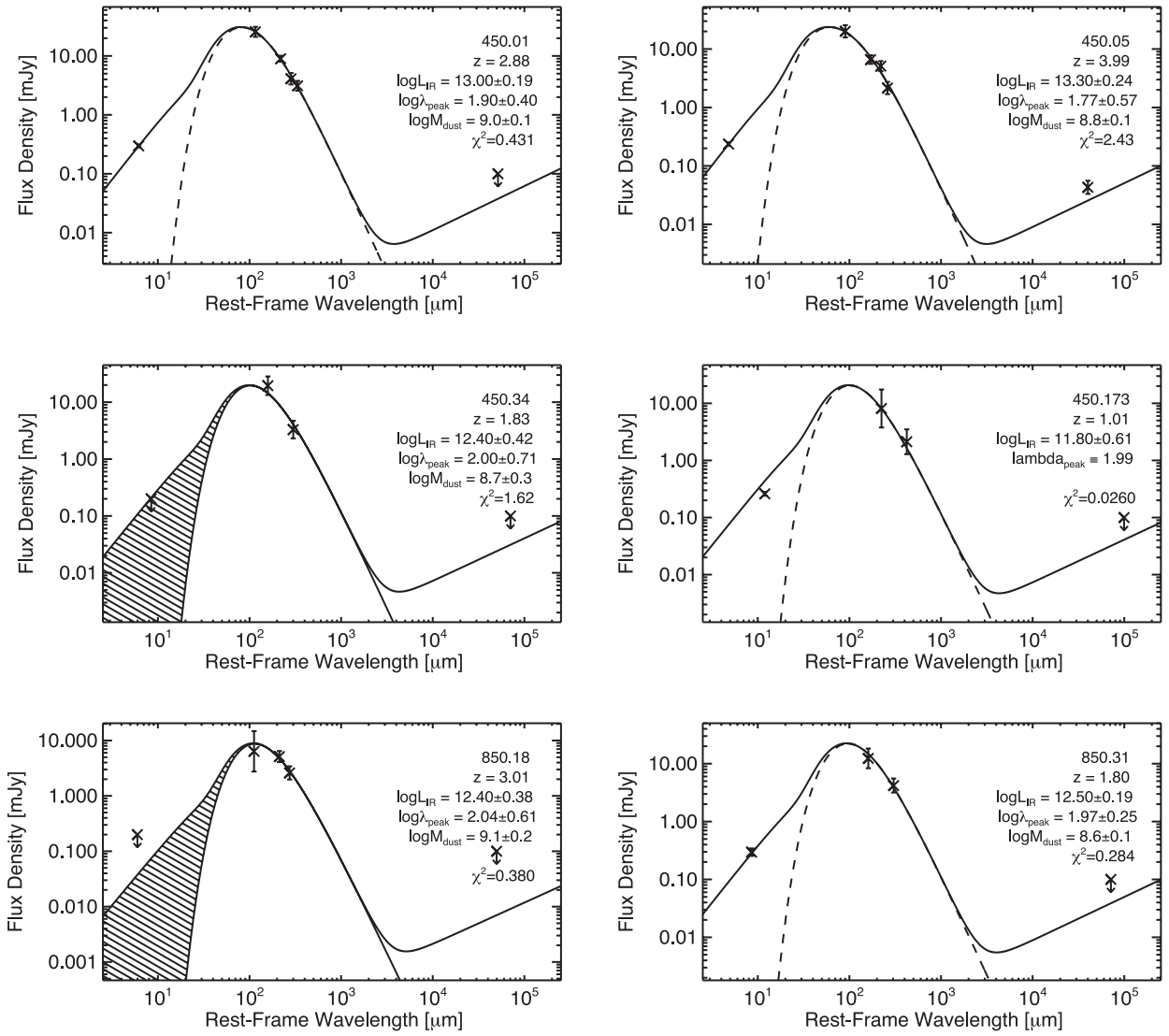

Figure 13. Example FIR SEDs for select SCUBA-2 sources, some 450 μm selected and some 850 μm selected. The assumed optical/NIR photometric redshift is specified in the upper right corner of each panel, as well as the measured $L_{\rm IR}$, $\lambda_{\rm peak}$, $M_{\rm dust}$ and χ^2 goodness of fit. If the SED fit used a fixed temperature due to a lack of >2 infrared photometric detections, then no dust mass is measured. In cases where there is no 24 μm detection, the MIR portion of the SED is shaded to indicate its uncertainty. The uncertainty in $L_{\rm IR}$ reflects this uncertainty. The radio portion of the SEDs is extrapolated from assuming the FIR/radio correlation holds (and evolves as measured in Ivison et al. 2010a,b) and are not fit to the radio data.

wavelength of S_ν called $\lambda_{\rm peak}$ ($\propto 1/T_{\rm dust}$), which is much more easily constrained by the data.

Since the number of FIR photometric data points is limited to 2–5 (from *Spitzer*-MIPS, SCUBA-2, AzTEC and MAMBO measurements), we only fit SEDs with two free parameters, $L_{\rm IR}$, and $\lambda_{\rm peak}$ and do not attempt to constrain emissivity or MIR power-law index.[5] The emissivity index, $\beta = 1.5$, is fixed (e.g. Pope et al. 2008; Younger et al. 2009; Chapin et al. 2011), as is the MIR power-law index, $\alpha = 2.0$ (e.g. Blain et al. 2003; Casey 2012). A representative sample of best-fitting SEDs, including both high and low S/N sources, is illustrated in Fig. 13.

Table 9 gives the basic derived properties from the SED fits, including χ^2 goodness of fit, $L_{\rm IR}$, the implied SFR from $L_{\rm IR}$ to one significant figure,[6] and the SED peak wavelength and dust masses, $\lambda_{\rm peak}$ and $M_{\rm dust}$. Note that all of the flux densities used in the fits do factor into χ^2, even non-detections; instead of treating non-detections as upper limits, we treat them as flux density measurements with very low significance (given by the extracted flux density from the map at the extracted position). The uncertainties on $L_{\rm IR}$, $\lambda_{\rm peak}$ and $M_{\rm dust}$ are derived from the photometric uncertainties in the FIR data and average ∼0.2–0.4 dex, ∼0.2–0.4 dex and ∼0.4–0.5 dex, respectively. These uncertainties *do not* account for uncertainty in the IMF or dust absorption coefficient which impact the SFR and $M_{\rm dust}$, respectively. Sources with just two FIR photometric points (and upper limits at other bands) have SEDs fixed to the mean dust $\lambda_{\rm peak}$ of their parent sample, either 450 μm selected galaxies or 850 μm selected galaxies. In the next section we measure these peak wavelengths as $\log \lambda_{\rm peak} = 2.05 \pm 0.04$ and

[5] Although for sources with ≥4 photometric points at >3σ, we allow variation in α; this removes some reliance on the 24 μm flux to map directly to the FIR peak.

[6] Assuming the Kennicutt (1998b) $L_{\rm IR}$-SFR scaling and a Salpeter IMF.

Table 9. Physical characteristics of Scuba-2 selected galaxies.

Short 450 μm name	Short 850 μm name	z_{phot}	χ^2_{fit}	Estimates from infrared SED fitting (Section 4.2) L_{IR} ($L_\odot$)	log SFR_{IR} ($M_\odot$ yr^{-1})	log λ_{peak} (μm)	M_{dust} ($M_\odot$)	Le Phare properties log SFR_{UV} ($M_\odot$ yr^{-1})	$M_\star$ ($M_\odot$)
450.00	850.07	$2.86^{+0.21}_{-0.26}$	0.4	$(5.1^{+7.4}_{-3.5})\times 10^{13}$	3.9 ± 0.2	1.6 ± 0.4	$(5^{+6}_{-4})\times 10^{8}$	$1.71^{+0.13}_{-0.33}$	$(2^{+3}_{-1})\times 10^{10}$
450.01	850.02	$2.88^{+0.09}_{-0.18}$	0.4	$(1.1^{+1.7}_{-0.7})\times 10^{13}$	3.3 ± 0.2	1.9 ± 0.4	$(1^{+2}_{-1})\times 10^{9}$	$1.86^{+0.29}_{-0.15}$	$(2^{+2}_{-1})\times 10^{11}$
450.02		$2.16^{+0.04}_{-0.06}$	2.4	$(8.6^{+16.6}_{-4.5})\times 10^{12}$	3.2 ± 0.3	2.0 ± 0.5	$(1^{+3}_{-1})\times 10^{9}$	$1.10^{+0.07}_{-0.07}$	$(9^{+10}_{-8})\times 10^{10}$
450.03	850.00	$0.34^{+0.01}_{-0.01}$	4.7	$(4.3^{+5.1}_{-3.6})\times 10^{10}$	0.9 ± 0.1	$\equiv 2.0$	–	$-0.50^{+0.07}_{-0.07}$	$(6^{+8}_{-5})\times 10^{10}$
450.04	850.03	$3.82^{+0.44}_{-0.69}$	1.2	$(1.9^{+3.3}_{-1.1})\times 10^{13}$	3.5 ± 0.3	1.8 ± 0.5	$(1^{+2}_{-1})\times 10^{9}$	$2.45^{+0.11}_{-0.32}$	$(7^{+10}_{-5})\times 10^{10}$
450.05	850.08	$3.99^{+0.08}_{-0.85}$	2.4	$(1.9^{+3.4}_{-1.1})\times 10^{13}$	3.5 ± 0.2	1.8 ± 0.6	$(7^{+9}_{-6})\times 10^{8}$	$2.16^{+0.10}_{-0.09}$	$(7^{+8}_{-6})\times 10^{11}$
450.06	850.12	$2.08^{+0.08}_{-0.07}$	0.3	$(7.2^{+9.2}_{-5.7})\times 10^{12}$	3.1 ± 0.1	1.9 ± 0.1	$(6^{+7}_{-5})\times 10^{8}$	$2.00^{+0.07}_{-0.07}$	$(1^{+1}_{-1})\times 10^{11}$
450.07		$4.70^{+0.07}_{-0.08}$	4.3	$(7.2^{+8.7}_{-6.0})\times 10^{13}$	4.1 ± 0.1	$\equiv 2.0$	–	$2.53^{+0.14}_{-0.47}$	$(4^{+6}_{-3})\times 10^{11}$
450.08		$5.15^{+0.20}_{-0.33}$	3.7	$(8.7^{+10.4}_{-7.2})\times 10^{13}$	4.2 ± 0.1	$\equiv 2.0$	–	$2.51^{+0.25}_{-0.59}$	$(2^{+3}_{-2})\times 10^{11}$
450.09	850.34	$1.90^{+0.03}_{-0.04}$	0.1	$(7.7^{+10.3}_{-5.7})\times 10^{12}$	3.1 ± 0.1	1.8 ± 0.1	$(3^{+4}_{-2})\times 10^{8}$	$2.26^{+0.09}_{-0.08}$	$(8^{+8}_{-7})\times 10^{9}$
450.12		$0.93^{+0.01}_{-0.01}$	0.1	$(5.8^{+18.6}_{-1.8})\times 10^{11}$	2.0 ± 0.5	$\equiv 2.0$	–	$1.61^{+0.07}_{-0.07}$	$(3^{+3}_{-3})\times 10^{10}$
450.13		$2.87^{+0.13}_{-0.26}$	0.1	$(8.7^{+11.5}_{-6.6})\times 10^{12}$	3.2 ± 0.1	1.8 ± 0.1	$(4^{+5}_{-3})\times 10^{8}$	$2.01^{+0.08}_{-0.09}$	$(2^{+2}_{-2})\times 10^{11}$
450.14		$1.47^{+0.01}_{-0.02}$	3.2	$(1.6^{+2.8}_{-0.9})\times 10^{12}$	2.4 ± 0.2	2.0 ± 0.2	$(6^{+10}_{-4})\times 10^{8}$	$1.81^{+0.08}_{-0.10}$	$(2^{+2}_{-2})\times 10^{11}$
450.15	850.28	$2.79^{+0.28}_{-0.29}$	0.5	$(1.1^{+1.4}_{-0.8})\times 10^{13}$	3.3 ± 0.1	1.8 ± 0.1	$(4^{+4}_{-3})\times 10^{8}$	$1.62^{+0.33}_{-0.19}$	$(4^{+5}_{-3})\times 10^{10}$
450.16		$2.32^{+0.02}_{-0.03}$	2.1	$(2.0^{+2.8}_{-1.4})\times 10^{12}$	2.5 ± 0.2	2.2 ± 0.2	$(9^{+40}_{-2})\times 10^{9}$	$1.20^{+0.07}_{-0.07}$	$(1^{+1}_{-1})\times 10^{11}$
450.17	850.42	$1.23^{+0.21}_{-0.11}$	0.1	$(7.9^{+18.9}_{-3.3})\times 10^{11}$	2.1 ± 0.4	2.1 ± 0.5	$(6^{+20}_{-2})\times 10^{8}$	$-0.35^{+0.40}_{-0.31}$	$(6^{+9}_{-3})\times 10^{8}$
450.19		$1.11^{+0.06}_{-0.02}$	9.7	$(9.7^{+32.0}_{-3.0})\times 10^{11}$	2.2 ± 0.5	$\equiv 2.0$	–	$0.56^{+0.09}_{-0.09}$	$(8^{+10}_{-7})\times 10^{9}$
450.20		$0.76^{+0.04}_{-0.03}$	0.8	$(2.6^{+5.7}_{-1.2})\times 10^{11}$	1.6 ± 0.3	2.2 ± 0.5	$(7^{+40}_{-2})\times 10^{8}$	$-0.05^{+0.37}_{-0.28}$	$(8^{+10}_{-6})\times 10^{8}$
450.21		$0.84^{+0.01}_{-0.01}$	0.1	$(4.7^{+7.9}_{-2.8})\times 10^{11}$	1.9 ± 0.2	2.1 ± 0.2	$(2^{+4}_{-1})\times 10^{8}$	$1.98^{+0.08}_{-0.07}$	$(4^{+4}_{-3})\times 10^{10}$
450.22	850.149	$2.11^{+0.20}_{-0.28}$	5.5	$(3.2^{+10.6}_{-1.\ })\times 10^{12}$	2.7 ± 0.5	$\equiv 2.0$	–	$0.31^{+0.13}_{-0.36}$	$(4^{+5}_{-3})\times 10^{9}$
450.23		$0.97^{+0.06}_{-0.04}$	0.6	$(5.4^{+17.9}_{-1.6})\times 10^{11}$	2.0 ± 0.5	$\equiv 2.0$	–	$0.46^{+0.34}_{-0.16}$	$(8^{+10}_{-6})\times 10^{8}$
450.24		$0.16^{+0.01}_{-0.01}$	3.5	$(3.2^{+10.6}_{-1.\ })\times 10^{10}$	0.7 ± 0.5	$\equiv 2.0$	–	$0.55^{+0.09}_{-0.11}$	$(6^{+7}_{-5})\times 10^{10}$
450.25		$0.61^{+0.01}_{-0.01}$	2.0	$(1.7^{+3.1}_{-1.\ })\times 10^{11}$	1.5 ± 0.3	2.2 ± 0.2	$(2^{+10}_{-1})\times 10^{8}$	$0.80^{+0.07}_{-0.07}$	$(1^{+2}_{-1})\times 10^{11}$
450.26		$2.68^{+0.11}_{-0.13}$	4.6	$(5.3^{+17.7}_{-1.6})\times 10^{12}$	3.0 ± 0.5	$\equiv 2.0$	–	$1.89^{+0.63}_{-0.12}$	$(7^{+9}_{-3})\times 10^{9}$
450.28		$1.98^{+0.03}_{-0.07}$	0.7	$(1.2^{+1.7}_{-0.8})\times 10^{12}$	2.3 ± 0.2	2.3 ± 0.2	$(1^{+10}_{-1})\times 10^{10}$	$2.10^{+0.07}_{-0.07}$	$(1^{+1}_{-1})\times 10^{10}$
450.30		$2.81^{+0.56}_{-0.56}$	3.5	$(6.0^{+10.}_{-3.6})\times 10^{12}$	3.0 ± 0.2	1.9 ± 0.2	$(4^{+5}_{-3})\times 10^{8}$	$1.81^{+0.12}_{-0.18}$	$(1^{+1}_{-1})\times 10^{11}$
450.32	850.26	$1.72^{+0.15}_{-0.09}$	5.0	$(1.6^{+2.3}_{-1.1})\times 10^{12}$	2.4 ± 0.2	2.1 ± 0.2	$(7^{+10}_{-5})\times 10^{8}$	$-0.27^{+0.22}_{-0.52}$	$(4^{+20}_{-1})\times 10^{8}$
450.33		$0.84^{+0.01}_{-0.01}$	0.1	$(3.8^{+7.2}_{-2.1})\times 10^{11}$	1.8 ± 0.3	2.1 ± 0.2	$(3^{+6}_{-1})\times 10^{8}$	$1.30^{+0.08}_{-0.09}$	$(4^{+4}_{-4})\times 10^{10}$
450.34		$1.83^{+0.03}_{-0.03}$	3.9	$(2.4^{+6.5}_{-0.9})\times 10^{12}$	2.6 ± 0.4	2.0 ± 0.7	$(6^{+10}_{-3})\times 10^{8}$	$1.89^{+0.08}_{-0.07}$	$(8^{+9}_{-7})\times 10^{10}$
450.36	850.58	$3.04^{+0.16}_{-0.12}$	0.1	$(6.9^{+18.8}_{-2.6})\times 10^{12}$	3.1 ± 0.4	1.9 ± 0.7	$(7^{+10}_{-5})\times 10^{8}$	$2.39^{+0.13}_{-0.41}$	$(3^{+6}_{-3})\times 10^{10}$
450.37		$2.17^{+0.08}_{-0.08}$	1.9	$(3.1^{+10.6}_{-0.9})\times 10^{12}$	2.7 ± 0.5	$\equiv 2.0$	–	$1.26^{+0.37}_{-0.15}$	$(4^{+6}_{-2})\times 10^{9}$
450.39		$0.61^{+0.02}_{-0.02}$	0.1	$(1.6^{+5.4}_{-0.5})\times 10^{11}$	1.4 ± 0.5	$\equiv 2.0$	–	$-2.37^{+0.67}_{-3.00}$	$(3^{+4}_{-3})\times 10^{9}$
450.41		$3.46^{+1.74}_{-1.90}$	0.1	$(8.8^{+30.3}_{-2.5})\times 10^{12}$	3.2 ± 0.5	$\equiv 2.0$	–	$1.14^{+0.39}_{-0.56}$	$(5^{+10}_{-2})\times 10^{9}$
450.42	850.48	$4.81^{+0.14}_{-0.21}$	3.1	$(1.6^{+4.0}_{-0.6})\times 10^{13}$	3.4 ± 0.4	1.7 ± 0.8	$(3^{+4}_{-2})\times 10^{8}$	$2.60^{+0.12}_{-0.34}$	$(3^{+4}_{-3})\times 10^{11}$
450.43		$0.36^{+0.06}_{-0.07}$	1.6	$(3.8^{+13.3}_{-1.1})\times 10^{10}$	0.8 ± 0.5	$\equiv 2.0$	–	$-1.11^{+0.48}_{-0.55}$	$(2^{+3}_{-1})\times 10^{8}$
450.44		$1.75^{+0.50}_{-0.51}$	0.1	$(1.8^{+6.3}_{-0.5})\times 10^{12}$	2.5 ± 0.5	$\equiv 2.0$	–	$0.33^{+0.41}_{-0.39}$	$(8^{+20}_{-4})\times 10^{8}$
450.45		$2.01^{+0.93}_{-0.71}$	1.0	$(2.5^{+8.9}_{-0.7})\times 10^{12}$	2.6 ± 0.5	$\equiv 2.0$	–	$0.61^{+0.43}_{-0.37}$	$(3^{+4}_{-1})\times 10^{9}$
450.46		$3.06^{+0.08}_{-0.06}$	4.3	$(5.5^{+19.6}_{-1.6})\times 10^{12}$	3.0 ± 0.5	$\equiv 2.0$	–	$2.17^{+0.12}_{-0.36}$	$(3^{+5}_{-3})\times 10^{10}$
450.47		$1.77^{+0.07}_{-0.24}$	0.1	$(1.1^{+4.0}_{-0.3})\times 10^{12}$	2.3 ± 0.5	$\equiv 2.0$	–	$1.64^{+0.35}_{-0.10}$	$(6^{+8}_{-4})\times 10^{9}$
450.49		$1.70^{+0.16}_{-0.10}$	4.1	$(1.4^{+5.1}_{-0.4})\times 10^{12}$	2.4 ± 0.6	$\equiv 2.0$	–	$0.48^{+0.28}_{-0.34}$	$(2^{+3}_{-1})\times 10^{9}$
450.51		$1.58^{+0.22}_{-0.45}$	0.1	$(1.1^{+3.8}_{-0.3})\times 10^{12}$	2.3 ± 0.6	$\equiv 2.0$	–	$0.79^{+0.37}_{-0.28}$	$(1^{+2}_{-0.7})\times 10^{9}$
450.53	850.109	$1.01^{+0.01}_{-0.01}$	1.8	$(8.6^{+14.6}_{-5.1})\times 10^{11}$	2.2 ± 0.2	2.0 ± 0.2	$(2^{+3}_{-1})\times 10^{8}$	$1.40^{+0.08}_{-0.08}$	$(8^{+9}_{-7})\times 10^{10}$
450.54	850.96	$1.90^{+0.14}_{-0.12}$	1.1	$(1.5^{+4.7}_{-0.5})\times 10^{12}$	2.4 ± 0.5	2.0 ± 0.8	$(4^{+7}_{-2})\times 10^{8}$	$1.73^{+0.13}_{-0.36}$	$(3^{+5}_{-3})\times 10^{9}$
450.55	850.06	$0.37^{+0.01}_{-0.01}$	1.6	$(2.8^{+3.4}_{-2.3})\times 10^{10}$	0.7 ± 0.1	$\equiv 2.0$	–	$-2.12^{+0.11}_{-3.40}$	$(3^{+4}_{-3})\times 10^{10}$
450.56		$2.82^{+1.39}_{-1.20}$	3.6	$(5.0^{+17.8}_{-1.4})\times 10^{12}$	2.9 ± 0.6	$\equiv 2.0$	–	$0.94^{+0.74}_{-0.74}$	$(3^{+20}_{-1})\times 10^{9}$
450.57		$3.48^{+1.33}_{-1.60}$	3.6	$(7.4^{+26.5}_{-2.1})\times 10^{12}$	3.1 ± 0.6	$\equiv 2.0$	–	$-3.61^{+2.43}_{-0.32}$	$(1^{+1}_{-0.9})\times 10^{11}$
450.59	850.101	$0.47^{+0.01}_{-0.01}$	4.0	$(8.3^{+18.6}_{-3.7})\times 10^{10}$	1.2 ± 0.3	2.2 ± 0.4	$(2^{+50}_{-1})\times 10^{8}$	$0.91^{+0.08}_{-0.08}$	$(3^{+3}_{-2})\times 10^{10}$
450.61		$4.58^{+0.11}_{-0.06}$	1.4	$(1.3^{+2.6}_{-0.7})\times 10^{13}$	3.3 ± 0.3	1.7 ± 0.3	$(2^{+3}_{-2})\times 10^{8}$	$2.69^{+0.12}_{-0.36}$	$(1^{+20}_{-7})\times 10^{10}$
450.62		$1.95^{+1.32}_{-1.10}$	0.1	$(1.9^{+6.7}_{-0.5})\times 10^{12}$	2.5 ± 0.6	$\equiv 2.0$	–	$0.40^{+0.56}_{-0.74}$	$(1^{+7}_{-0.2})\times 10^{9}$

Table 9 – *continued*

Short 450 μm name	Short 850 μm name	$z_{\rm phot}$	$\chi^2_{\rm fit}$	Estimates from infrared SED fitting (Section 4.2) $L_{\rm IR}$ ($L_\odot$)	$\log {\rm SFR_{IR}}$ ($M_\odot$ yr^{-1})	$\log \lambda_{\rm peak}$ (μm)	$M_{\rm dust}$ ($M_\odot$)	Le Phare properties $\log {\rm SFR_{UV}}$ ($M_\odot$ yr^{-1})	$M_\star$ ($M_\odot$)
450.63		$2.36^{+0.13}_{-0.12}$	3.4	$(2.8^{+10.2}_{-0.8})\times 10^{12}$	2.7 ± 0.6	$\equiv 2.0$	–	$0.53^{+0.35}_{-0.11}$	$(3^{+5}_{-2})\times 10^{9}$
450.65		$0.70^{+2.57}_{-0.49}$	0.1	$(1.5^{+5.5}_{-0.4})\times 10^{11}$	1.4 ± 0.6	$\equiv 2.0$	–	$-0.30^{+0.50}_{-0.57}$	$(2^{+4}_{-1})\times 10^{8}$
450.67		$0.93^{+0.01}_{-0.01}$	1.4	$(8.7^{+18.1}_{-4.2})\times 10^{11}$	2.2 ± 0.3	2.0 ± 0.2	$(2^{+4}_{-1})\times 10^{8}$	$2.23^{+0.09}_{-0.10}$	$(5^{+5}_{-4})\times 10^{10}$
450.69		$2.04^{+0.49}_{-0.48}$	0.1	$(2.0^{+7.3}_{-0.5})\times 10^{12}$	2.5 ± 0.6	$\equiv 2.0$	–	$0.71^{+0.41}_{-0.38}$	$(3^{+5}_{-2})\times 10^{9}$
450.70		$3.03^{+0.04}_{-0.03}$	0.1	$(8.6^{+17.7}_{-4.1})\times 10^{12}$	3.2 ± 0.3	1.8 ± 0.3	$(3^{+4}_{-2})\times 10^{8}$	$3.06^{+0.09}_{-0.36}$	$(6^{+8}_{-5})\times 10^{10}$
450.71		$1.95^{+0.61}_{-0.42}$	0.6	$(2.6^{+9.5}_{-0.7})\times 10^{12}$	2.6 ± 0.6	$\equiv 2.0$	–	$0.67^{+0.41}_{-0.38}$	$(2^{+4}_{-1})\times 10^{9}$
450.72		$1.43^{+0.31}_{-0.11}$	2.8	$(9.9^{+36.1}_{-2.7})\times 10^{11}$	2.2 ± 0.6	$\equiv 2.0$	–	$0.91^{+0.24}_{-0.51}$	$(2^{+4}_{-1})\times 10^{9}$
450.74		$0.75^{+0.01}_{-0.01}$	3.8	$(1.9^{+7.0}_{-0.5})\times 10^{11}$	1.5 ± 0.6	$\equiv 2.0$	–	$1.04^{+0.09}_{-0.10}$	$(4^{+5}_{-3})\times 10^{9}$
450.75		$2.26^{+2.30}_{-1.30}$	3.9	$(3.2^{+11.9}_{-0.9})\times 10^{12}$	2.7 ± 0.6	$\equiv 2.0$	–	$0.56^{+0.44}_{-0.39}$	$(2^{+3}_{-1})\times 10^{9}$
450.76		$1.96^{+0.45}_{-0.51}$	0.1	$(1.9^{+6.8}_{-0.5})\times 10^{12}$	2.5 ± 0.6	$\equiv 2.0$	–	$-0.03^{+0.43}_{-0.38}$	$(1^{+2}_{-0.5})\times 10^{9}$
450.77		$1.43^{+0.03}_{-0.04}$	0.1	$(8.8^{+32.3}_{-2.4})\times 10^{11}$	2.2 ± 0.6	$\equiv 2.0$	–	$1.27^{+0.63}_{-0.48}$	$(3^{+4}_{-1})\times 10^{10}$
450.81	850.10	$1.75^{+0.08}_{-0.12}$	0.1	$(1.6^{+2.3}_{-1.1})\times 10^{12}$	2.4 ± 0.2	2.1 ± 0.2	$(1^{+2}_{-1})\times 10^{9}$	$1.58^{+0.14}_{-0.15}$	$(2^{+2}_{-1})\times 10^{10}$
450.86	850.55	$3.59^{+0.45}_{-0.81}$	1.8	$(6.8^{+25.4}_{-1.8})\times 10^{12}$	3.1 ± 0.6	$\equiv 2.0$	–	$1.69^{+0.41}_{-0.29}$	$(1^{+2}_{-0.9})\times 10^{10}$
450.87	850.09	$2.71^{+0.19}_{-0.17}$	3.2	$(6.3^{+9.0}_{-4.4})\times 10^{12}$	3.0 ± 0.2	1.9 ± 0.2	$(1^{+10}_{-8})\times 10^{8}$	$2.04^{+0.09}_{-0.10}$	$(1^{+2}_{-1})\times 10^{11}$
450.94	850.23	$0.71^{+0.01}_{-0.01}$	3.4	$(8.2^{+30.9}_{-2.1})\times 10^{10}$	1.1 ± 0.6	$\equiv 2.0$	–	$-4.41^{+3.35}_{-0.33}$	$(2^{+3}_{-2})\times 10^{10}$
450.96	850.133	$2.34^{+0.40}_{-0.41}$	0.1	$(2.1^{+8.0}_{-0.6})\times 10^{12}$	2.6 ± 0.6	$\equiv 2.0$	–	$1.09^{+0.42}_{-0.22}$	$(2^{+2}_{-1})\times 10^{10}$
450.99	850.33	$2.16^{+0.08}_{-0.13}$	2.9	$(1.9^{+5.0}_{-0.7})\times 10^{12}$	2.5 ± 0.4	2.1 ± 0.6	$(2^{+4}_{-1})\times 10^{9}$	$1.74^{+0.11}_{-0.32}$	$(9^{+10}_{-7})\times 10^{10}$
450.106	850.92	$1.0^{+0.01}_{-0.01}$	0.1	$(2.3^{+8.8}_{-0.6})\times 10^{11}$	1.6 ± 0.6	$\equiv 2.0$	–	$0.96^{+0.27}_{-0.11}$	$(2^{+2}_{-1})\times 10^{10}$
450.126	850.159	$2.04^{+0.92}_{-1.30}$	0.4	$(1.4^{+5.5}_{-0.4})\times 10^{12}$	2.4 ± 0.6	$\equiv 2.0$	–	$1.27^{+0.27}_{-0.35}$	$(1^{+3}_{-0.5})\times 10^{10}$
450.133	850.131	$0.93^{+0.01}_{-0.01}$	0.1	$(1.8^{+7.2}_{-0.4})\times 10^{11}$	1.5 ± 0.6	$\equiv 2.0$	–	$2.80^{+0.07}_{-0.07}$	$(3^{+3}_{-2})\times 10^{10}$
450.134	850.52	$2.89^{+0.14}_{-0.24}$	2.8	$(4.1^{+7.0}_{-2.5})\times 10^{12}$	2.8 ± 0.2	1.9 ± 0.3	$(4^{+6}_{-4})\times 10^{8}$	$1.73^{+0.14}_{-0.32}$	$(6^{+7}_{-4})\times 10^{10}$
450.135	850.163	$1.68^{+0.08}_{-0.06}$	1.0	$(2.5^{+9.9}_{-0.6})\times 10^{12}$	2.6 ± 0.6	$\equiv 2.0$	–	$1.88^{+0.08}_{-0.08}$	$(2^{+3}_{-2})\times 10^{10}$
450.166	850.83	$0.93^{+0.01}_{-0.01}$	3.2	$(1.7^{+7.1}_{-0.4})\times 10^{11}$	1.5 ± 0.6	$\equiv 2.0$	–	$0.54^{+0.12}_{-0.12}$	$(2^{+3}_{-2})\times 10^{9}$
450.173	850.104	$1.01^{+0.01}_{-0.01}$	3.3	$(5.8^{+23.9}_{-1.4})\times 10^{11}$	2.0 ± 0.6	$\equiv 2.0$	–	$1.83^{+0.36}_{-0.12}$	$(2^{+3}_{-2})\times 10^{10}$
450.179	850.88	$0.66^{+0.01}_{-0.01}$	0.1	$(6.9^{+28.8}_{-1.7})\times 10^{10}$	1.1 ± 0.6	$\equiv 2.0$	–	$1.62^{+0.11}_{-0.42}$	$(5^{+6}_{-4})\times 10^{9}$
450.193	850.49	$3.08^{+0.13}_{-0.16}$	2.9	$(3.2^{+13.3}_{-0.8})\times 10^{12}$	2.7 ± 0.6	$\equiv 2.0$	–	$2.28^{+0.10}_{-0.29}$	$(1^{+2}_{-1})\times 10^{11}$
450.206	850.53	$1.70^{+0.20}_{-0.20}$	3.4	$(7.9^{+33.5}_{-1.9})\times 10^{11}$	2.1 ± 0.6	$\equiv 2.0$	–	$-0.16^{+0.15}_{-0.09}$	$(1^{+2}_{-0.6})\times 10^{9}$
450.215	850.27	$2.76^{+0.10}_{-0.12}$	3.0	$(4.1^{+6.5}_{-2.6})\times 10^{12}$	2.8 ± 0.2	1.9 ± 0.3	$(6^{+8}_{-5})\times 10^{8}$	$1.66^{+0.25}_{-0.10}$	$(8^{+9}_{-6})\times 10^{10}$
450.240	850.67	$2.73^{+2.39}_{-1.20}$	3.0	$(2.4^{+10.3}_{-0.5})\times 10^{12}$	2.6 ± 0.6	$\equiv 2.0$	–	$1.12^{+0.28}_{-2.30}$	$(2^{+3}_{-1})\times 10^{10}$
450.247	850.151	$1.78^{+0.93}_{-0.71}$	0.1	$(7.1^{+31.1}_{-1.6})\times 10^{11}$	2.1 ± 0.6	$\equiv 2.0$	–	$0.07^{+0.44}_{-0.42}$	$(5^{+10}_{-2})\times 10^{8}$
	850.01	$1.37^{+0.44}_{-0.25}$	1.9	$(4.7^{+8.6}_{-2.6})\times 10^{11}$	1.9 ± 0.3	2.3 ± 0.3	$(6^{+20}_{-2})\times 10^{9}$	$0.98^{+0.29}_{-0.25}$	$(2^{+2}_{-1})\times 10^{9}$
	850.04	$1.39^{+0.02}_{-0.02}$	1.3	$(4.7^{+7.9}_{-2.8})\times 10^{11}$	1.9 ± 0.2	2.4 ± 0.2	$(1^{+2}_{-1})\times 10^{10}$	$1.37^{+0.09}_{-0.07}$	$(3^{+4}_{-3})\times 10^{10}$
	850.05	$2.55^{+0.12}_{-0.15}$	0.1	$(2.8^{+5.1}_{-1.5})\times 10^{12}$	2.7 ± 0.3	2.1 ± 0.3	$(5^{+10}_{-2})\times 10^{9}$	$1.47^{+0.10}_{-0.08}$	$(2^{+2}_{-2})\times 10^{10}$
	850.11	$2.77^{+0.16}_{-0.19}$	0.3	$(1.5^{+4.4}_{-0.5})\times 10^{12}$	2.4 ± 0.5	$\equiv 2.1$	–	$1.36^{+0.10}_{-0.34}$	$(4^{+5}_{-4})\times 10^{10}$
	850.13	$0.86^{+0.48}_{-0.55}$	0.2	$(9.0^{+17.5}_{-4.7})\times 10^{10}$	1.2 ± 0.3	2.4 ± 0.3	$(2^{+10}_{-1})\times 10^{9}$	$-0.13^{+0.51}_{-0.38}$	$(8^{+10}_{-3})\times 10^{8}$
	850.18	$3.01^{+0.17}_{-0.21}$	0.1	$(2.3^{+5.6}_{-1.})\times 10^{12}$	2.6 ± 0.4	2.0 ± 0.6	$(1^{+2}_{-1})\times 10^{9}$	$1.08^{+0.35}_{-0.30}$	$(9^{+10}_{-6})\times 10^{9}$
	850.19	$2.24^{+2.19}_{-1.00}$	0.1	$(4.5^{+14.0}_{-1.5})\times 10^{11}$	1.9 ± 0.5	$\equiv 2.1$	–	$0.48^{+0.43}_{-0.39}$	$(1^{+2}_{-0.7})\times 10^{9}$
	850.20	$2.80^{+0.05}_{-0.07}$	0.1	$(1.4^{+3.4}_{-0.5})\times 10^{12}$	2.4 ± 0.4	2.1 ± 0.5	$(2^{+4}_{-1})\times 10^{9}$	$1.08^{+0.08}_{-0.07}$	$(3^{+4}_{-3})\times 10^{10}$
	850.22	$2.06^{+0.10}_{-0.10}$	0.4	$(1.2^{+2.6}_{-0.6})\times 10^{12}$	2.3 ± 0.3	2.3 ± 0.3	$(5^{+20}_{-1})\times 10^{9}$	$1.83^{+0.11}_{-0.35}$	$(2^{+2}_{-2})\times 10^{11}$
	850.24	$2.94^{+0.96}_{-0.36}$	1.2	$(1.0^{+1.5}_{-0.7})\times 10^{13}$	3.2 ± 0.2	1.8 ± 0.1	$(5^{+6}_{-4})\times 10^{8}$	$0.21^{+0.14}_{-0.35}$	$(1^{+10}_{-0.2})\times 10^{9}$
	850.25	$2.33^{+0.05}_{-0.05}$	1.3	$(1.9^{+3.5}_{-1.1})\times 10^{12}$	2.5 ± 0.2	2.3 ± 0.3	$(8^{+30}_{-2})\times 10^{9}$	$2.50^{+0.13}_{-0.50}$	$(2^{+2}_{-2})\times 10^{11}$
	850.30	$0.23^{+0.01}_{-0.01}$	1.9	$(1.4^{+2.2}_{-1.})\times 10^{10}$	0.4 ± 0.2	2.3 ± 0.1	$(1^{+2}_{-1})\times 10^{8}$	$0.15^{+0.10}_{-0.10}$	$(1^{+2}_{-1})\times 10^{9}$
	850.31	$1.80^{+0.04}_{-0.05}$	0.6	$(2.9^{+4.5}_{-1.9})\times 10^{12}$	2.7 ± 0.2	2.0 ± 0.3	$(5^{+6}_{-4})\times 10^{8}$	$2.05^{+0.10}_{-0.12}$	$(7^{+8}_{-5})\times 10^{10}$
	850.32	$2.87^{+0.13}_{-0.26}$	13.	$(8.5^{+11.9}_{-6.1})\times 10^{12}$	3.2 ± 0.1	1.8 ± 0.1	$(4^{+4}_{-3})\times 10^{8}$	$2.01^{+0.08}_{-0.09}$	$(2^{+2}_{-2})\times 10^{11}$
	850.35	$2.36^{+0.20}_{-0.33}$	0.1	$(1.1^{+3.4}_{-0.4})\times 10^{12}$	2.3 ± 0.5	2.2 ± 0.6	$(3^{+10}_{-1})\times 10^{9}$	$1.00^{+0.08}_{-0.09}$	$(1^{+2}_{-0.9})\times 10^{10}$
	850.36	$2.05^{+0.02}_{-0.03}$	2.9	$(2.2^{+7.0}_{-0.7})\times 10^{12}$	2.6 ± 0.5	$\equiv 2.1$	–	$1.72^{+0.10}_{-0.30}$	$(1^{+2}_{-1})\times 10^{11}$
	850.37	$4.57^{+1.07}_{-1.60}$	0.3	$(3.3^{+10.6}_{-1.0})\times 10^{12}$	2.8 ± 0.5	$\equiv 2.1$	–	$2.10^{+0.19}_{-0.33}$	$(7^{+10}_{-4})\times 10^{10}$
	850.38	$2.04^{+0.14}_{-0.09}$	0.1	$(1.5^{+4.0}_{-0.6})\times 10^{12}$	2.4 ± 0.4	2.1 ± 0.6	$(1^{+2}_{-1})\times 10^{9}$	$1.79^{+0.07}_{-0.07}$	$(3^{+3}_{-2})\times 10^{9}$
	850.43	$0.84^{+0.43}_{-0.42}$	1.3	$(5.1^{+16.4}_{-1.6})\times 10^{10}$	0.9 ± 0.5	$\equiv 2.1$	–	$-0.07^{+0.52}_{-0.38}$	$(8^{+20}_{-4})\times 10^{8}$

Table 9 – *continued*

Short 450 μm name	Short 850 μm name	z_{phot}	χ^2_{fit}	Estimates from infrared SED fitting (Section 4.2) L_{IR} ($L_\odot$)	log SFR_{IR} ($M_\odot$ yr^{-1})	log λ_{peak} (μm)	M_{dust} ($M_\odot$)	LE PHARE properties log SFR_{UV} ($M_\odot$ yr^{-1})	$M_\star$ ($M_\odot$)
	850.44	$2.48^{+0.13}_{-0.10}$	1.5	$(3.0^{+4.9}_{-1.9})\times 10^{12}$	2.7 ± 0.2	1.9 ± 0.2	$(4^{+5}_{-3})\times 10^8$	$1.61^{+0.11}_{-0.34}$	$(1^{+2}_{-0.7})\times 10^{10}$
	850.45	$1.32^{+0.03}_{-0.05}$	1.1	$(2.3^{+7.4}_{-0.7})\times 10^{11}$	1.6 ± 0.5	$\equiv 2.1$	–	$1.56^{+0.11}_{-0.27}$	$(3^{+3}_{-2})\times 10^{10}$
	850.46	$2.82^{+0.13}_{-0.19}$	0.1	$(1.5^{+2.0}_{-1.0})\times 10^{13}$	3.4 ± 0.1	1.8 ± 0.1	$(4^{+5}_{-4})\times 10^8$	$1.90^{+0.16}_{-0.24}$	$(2^{+2}_{-2})\times 10^{11}$
	850.50	$2.38^{+0.37}_{-0.51}$	0.1	$(3.2^{+10.6}_{-1.})\times 10^{11}$	1.7 ± 0.5	2.4 ± 0.4	$(2^{+70}_{-1})\times 10^{10}$	$0.90^{+0.40}_{-0.19}$	$(5^{+8}_{-2})\times 10^9$
	850.51	$1.11^{+0.07}_{-0.04}$	1.0	$(6.6^{+10.5}_{-4.1})\times 10^{11}$	2.1 ± 0.2	2.1 ± 0.2	$(6^{+10}_{-3})\times 10^8$	$1.29^{+0.08}_{-0.07}$	$(8^{+10}_{-7})\times 10^9$
	850.54	$3.07^{+1.19}_{-1.20}$	1.6	$(2.3^{+7.5}_{-0.7})\times 10^{12}$	2.6 ± 0.5	$\equiv 2.1$	–	$1.25^{+0.40}_{-0.48}$	$(8^{+10}_{-4})\times 10^9$
	850.57	$0.74^{+0.01}_{-0.01}$	1.2	$(9.4^{+21.3}_{-4.1})\times 10^{10}$	1.2 ± 0.4	2.4 ± 0.4	$(2^{+7}_{-1})\times 10^9$	$-1.83^{+1.35}_{-0.14}$	$(2^{+3}_{-2})\times 10^{11}$
	850.59	$3.15^{+0.13}_{-0.17}$	0.3	$(3.8^{+12.9}_{-1.1})\times 10^{12}$	2.8 ± 0.5	$\equiv 2.1$	–	$1.05^{+0.38}_{-0.13}$	$(8^{+10}_{-4})\times 10^9$
	850.60	$1.44^{+0.02}_{-0.02}$	4.5	$(1.4^{+2.2}_{-0.9})\times 10^{12}$	2.4 ± 0.2	2.0 ± 0.2	$(4^{+5}_{-3})\times 10^8$	$1.43^{+0.08}_{-0.09}$	$(1^{+1}_{-1})\times 10^{11}$
	850.61	$0.53^{+0.02}_{-0.02}$	0.4	$(5.4^{+14.4}_{-2.0})\times 10^{10}$	1.0 ± 0.4	2.3 ± 0.5	$(4^{+50}_{-1})\times 10^8$	$-0.31^{+0.23}_{-0.15}$	$(6^{+8}_{-6})\times 10^8$
	850.63	$1.89^{+0.23}_{-0.18}$	1.2	$(3.4^{+4.1}_{-2.8})\times 10^{11}$	1.8 ± 0.1	$\equiv 2.1$	–	$0.23^{+0.14}_{-0.33}$	$(3^{+4}_{-2})\times 10^9$
	850.64	$3.39^{+1.16}_{-1.50}$	0.1	$(2.1^{+7.1}_{-0.6})\times 10^{12}$	2.6 ± 0.5	$\equiv 2.1$	–	$1.61^{+0.30}_{-0.40}$	$(1^{+2}_{-0.7})\times 10^{10}$
	850.65	$0.48^{+0.01}_{-0.01}$	5.3	$(7.6^{+13.1}_{-4.4})\times 10^{10}$	1.1 ± 0.2	2.3 ± 0.2	$(3^{+30}_{-1})\times 10^8$	$0.42^{+0.80}_{-0.09}$	$(4^{+4}_{-2})\times 10^8$
	850.66	$0.94^{+0.14}_{-0.16}$	1.2	$(1.6^{+5.6}_{-0.5})\times 10^{11}$	1.4 ± 0.5	$\equiv 2.1$	–	$0.14^{+0.37}_{-0.37}$	$(5^{+8}_{-4})\times 10^8$
	850.68	$1.95^{+0.04}_{-0.04}$	0.1	$(2.7^{+4.4}_{-1.7})\times 10^{12}$	2.7 ± 0.2	2.0 ± 0.2	$(4^{+5}_{-3})\times 10^8$	$1.76^{+0.10}_{-0.30}$	$(2^{+2}_{-1})\times 10^{11}$
	850.69	$1.80^{+0.15}_{-0.11}$	0.1	$(1.6^{+2.9}_{-0.9})\times 10^{12}$	2.4 ± 0.3	2.0 ± 0.2	$(4^{+6}_{-3})\times 10^8$	$1.60^{+0.07}_{-0.07}$	$(4^{+5}_{-3})\times 10^{10}$
	850.70	$0.78^{+0.01}_{-0.03}$	2.3	$(1.8^{+3.2}_{-1.})\times 10^{11}$	1.5 ± 0.3	2.2 ± 0.2	$(4^{+10}_{-1})\times 10^8$	$1.40^{+0.07}_{-0.07}$	$(2^{+3}_{-2})\times 10^9$
	850.71	$2.17^{+1.36}_{-1.40}$	0.3	$(8.7^{+30.0}_{-2.5})\times 10^{11}$	2.2 ± 0.5	$\equiv 2.1$	–	$0.61^{+0.60}_{-0.78}$	$(2^{+10}_{-1})\times 10^9$
	850.72	$2.80^{+0.15}_{-0.16}$	2.0	$(4.5^{+7.9}_{-2.6})\times 10^{12}$	2.9 ± 0.2	1.9 ± 0.2	$(3^{+4}_{-2})\times 10^8$	$1.78^{+0.10}_{-0.09}$	$(2^{+2}_{-2})\times 10^{11}$
	850.73	$3.91^{+0.94}_{-1.20}$	0.1	$(7.2^{+25.2}_{-2.1})\times 10^{12}$	3.1 ± 0.5	$\equiv 2.1$	–	$2.32^{+0.13}_{-0.19}$	$(6^{+9}_{-4})\times 10^{10}$
	850.74	$2.76^{+2.78}_{-1.50}$	0.1	$(1.8^{+6.4}_{-0.5})\times 10^{12}$	2.5 ± 0.5	$\equiv 2.1$	–	$1.21^{+0.36}_{-0.42}$	$(8^{+10}_{-4})\times 10^9$
	850.76	$1.99^{+0.07}_{-0.22}$	1.4	$(9.1^{+32.0}_{-2.6})\times 10^{11}$	2.2 ± 0.5	$\equiv 2.1$	–	$2.69^{+0.07}_{-0.07}$	$(5^{+5}_{-5})\times 10^9$
	850.78	$0.94^{+0.01}_{-0.01}$	0.3	$(4.2^{+7.3}_{-2.4})\times 10^{11}$	1.9 ± 0.2	2.1 ± 0.2	$(3^{+5}_{-2})\times 10^8$	$0.79^{+0.08}_{-0.07}$	$(1^{+2}_{-1})\times 10^{10}$
	850.80	$3.54^{+0.12}_{-0.15}$	0.2	$(2.8^{+9.8}_{-0.8})\times 10^{12}$	2.7 ± 0.5	$\equiv 2.1$	–	$1.77^{+0.12}_{-0.36}$	$(4^{+6}_{-3})\times 10^{10}$
	850.81	$0.40^{+0.03}_{-0.03}$	1.3	$(1.4^{+4.9}_{-0.4})\times 10^{10}$	0.4 ± 0.5	$\equiv 2.1$	–	$-1.45^{+0.35}_{-0.23}$	$(5^{+7}_{-3})\times 10^8$
	850.82	$2.87^{+0.17}_{-0.25}$	1.3	$(6.2^{+11.3}_{-3.4})\times 10^{12}$	3.0 ± 0.3	1.8 ± 0.2	$(3^{+4}_{-2})\times 10^8$	$2.10^{+0.08}_{-0.10}$	$(2^{+3}_{-2})\times 10^{11}$
	850.84	$2.42^{+0.38}_{-0.48}$	1.1	$(2.0^{+7.1}_{-0.6})\times 10^{12}$	2.5 ± 0.6	$\equiv 2.1$	–	$0.68^{+0.40}_{-0.17}$	$(4^{+6}_{-2})\times 10^9$
	850.87	$2.24^{+0.42}_{-0.19}$	0.1	$(4.2^{+7.3}_{-2.4})\times 10^{12}$	2.9 ± 0.2	1.8 ± 0.2	$(2^{+2}_{-1})\times 10^8$	$1.07^{+0.62}_{-0.70}$	$(6^{+40}_{-1})\times 10^9$
	850.91	$2.71^{+0.46}_{-0.55}$	0.1	$(2.0^{+7.1}_{-0.6})\times 10^{12}$	2.5 ± 0.6	$\equiv 2.1$	–	$1.03^{+0.41}_{-0.36}$	$(8^{+10}_{-5})\times 10^9$
	850.94	$2.04^{+0.10}_{-0.21}$	0.1	$(7.3^{+9.1}_{-5.8})\times 10^{11}$	2.1 ± 0.1	$\equiv 2.1$	–	$2.10^{+0.07}_{-0.07}$	$(1^{+1}_{-1})\times 10^{11}$
	850.95	$1.55^{+0.05}_{-0.08}$	0.2	$(2.2^{+7.9}_{-0.6})\times 10^{12}$	2.6 ± 0.6	$\equiv 2.1$	–	$2.48^{+0.09}_{-0.28}$	$(8^{+10}_{-7})\times 10^{10}$
	850.97	$0.73^{+0.01}_{-0.01}$	0.1	$(3.4^{+6.4}_{-1.8})\times 10^{11}$	1.8 ± 0.3	2.1 ± 0.2	$(2^{+4}_{-1})\times 10^8$	$-3.90^{+1.94}_{-0.88}$	$(2^{+2}_{-2})\times 10^{11}$

Notes. Some basic derived properties of 450 μm sources using the infrared SED fitting described in Section 4.2. The sources' optical/NIR photometric redshifts are given by z_p. Their integrated 8–1000 μm infrared luminosity, L_{IR}, infrared star formation rates SFR_{IR} (calculated via the relation given in Kennicutt 1998a), SED peak wavelength, and approximated dust masses M_{dust} are calculated assuming SEDs as described in Section 4.2. Sources with fewer than three IR photometric points have the SED peak wavelength (or dust temperature) fixed to the mean of the remainder of the sample, measured to be $\langle \log(\lambda_{peak}/\mu m)\rangle = 2.05 \pm 0.04$ for 450 μm detected galaxies and $\langle \log(\lambda_{peak}/\mu m)\rangle = 2.12 \pm 0.04$ for 850 μm only detected galaxies.

log $\lambda_{peak} = 2.12 \pm 0.03$, respectively. We do not attempt to constrain the SEDs of sources without photometric redshifts.

4.3 Bulk infrared properties of the population

Fig. 14 illustrates infrared luminosities against photometric redshift for both 450 μmand 850 μm selected galaxies. Both 450 μm and 850 μm samples by and large sit at $1 < z < 4$ with $10^{12} < L_{IR} < 10^{13.2}$ $L_\odot$. This is very similar to the luminosity and redshift range probed by the original SCUBA 850 μm surveys; the distribution of the Chapman et al. (2005) spectroscopically confirmed sample (with improved luminosity estimates using photometry from Kovács et al. 2006) is shown for comparison. The parameter space probed by ∼1 mm-selected populations (e.g. Yun et al. 2012) is similar. We also compare to the recent spectroscopically confirmed sample of *Herschel*-SPIRE sources analysed in Casey et al. (2012a,b); the SPIRE sources (selected at 250–500 μm) peak in density at lower redshifts and lower luminosities, although at a given redshift, the SCUBA-2 sources probe ∼0.1–0.5 dex fainter sources than SPIRE.

The distributions in infrared luminosity and peak SED wavelength (the two free parameters of our SED fitting technique) are plotted in the middle of Fig. 14 and can be used to assess basic differences between subsets of the population. What we find is that the subset detected at both 450 μm and 850 μm is more luminous than the marginal sample and those detected at only one wavelength. The median SED peak wavelength of the 850 μm only sample is longer than those detected at both wavelengths (translating to cooler temperatures). The subsets which are 450 μm only

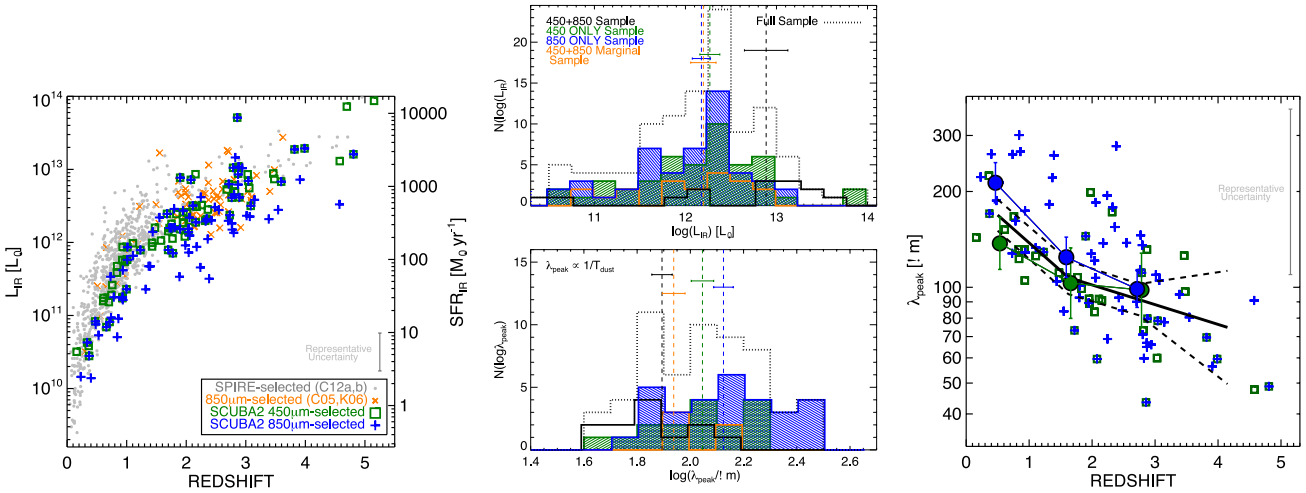

Figure 14. Left: infrared luminosity against photometric redshift for 450 μm (green squares) and 850 μm selected (blue crosses) sources. For context, the 850 μm selected SCUBA sources (orange crosses; Chapman et al. 2005; Kovács et al. 2006) and *Herschel*-SPIRE-selected, spectroscopically confirmed sources (grey circles; Casey et al. 2012a,b) are overplotted. The mean redshift of the SCUBA2 sample is similar to the original SCUBA-selected sources and higher than SPIRE sources while the SCUBA-2 luminosities, at a given redshift, probe to slightly lower luminosities (∼0.1–0.4 dex) than SPIRE sources. Middle: histograms of infrared luminosity and SED peak wavelength (inversely proportional to dust temperature), for various subsamples of SCUBA-2 sources: the whole sample (dotted lines), the overlapping $>3.6\sigma$ 450 and 850 sources (detected in both bands, black), 450 μm $>3.6\sigma$ sources not detected at 850 μm (green), 850 μm $>3.6\sigma$ sources not detected at 450 μm (blue), and the marginal $3 < \sigma < 3.6$ 450 and 850 source catalogue (orange). Vertical lines mark the median value for each subset and 1σ statistical variation on the median determined by bootstrapping. Right: SED peak wavelength against redshift for sources which have peak wavelength constraints. The median SED peak wavelength for all SCUBA-2 galaxies as a function of redshift is shown in black with dashed 67 per cent intervals and error bars representing uncertainty on the median. The median dust temperature evolution of 450 μm only detected galaxies is shown as green circles, while 850 μm only detected galaxies are in blue. At low redshifts ($z \leq 2$) the two populations have statistically distinct SED shapes, echoing the results from Fig. 12.

detected and marginal $3 < \sigma < 3.6$ sources have median SED peak wavelengths which lie between. Uncertainties on the median values in luminosity and SED peak wavelength are determined through bootstrapping.

Fig. 14 also shows the change in SED peak wavelength with redshift, where higher redshift sources tend to have hotter SEDs peaking at shorter rest-frame wavelengths. This increase in temperature (decrease in SED peak wavelength) also correlates with $L_{\rm IR}$, whereby the higher redshift sources are also the most luminous and hotter, which is a well-documented correlation (e.g. Soifer et al. 1987, 1989; Chapman et al. 2003; Chapin, Hughes & Aretxaga 2009; Hwang et al. 2010). Fig. 14 shows us that the sources detected only at 450 μm are statistically warmer (peak at shorter wavelengths) than average and 850 μm are statistically cooler (peak at longer wavelengths), and that the difference in median peak wavelengths is $\Delta\log(\lambda_{\rm peak}) = 0.16$ dex, which is ∼50 μm, at $z \lesssim 1$ and 0.10 dex at $1 < z < 2.5$, which is ∼20 μm.

These results suggest that, by and large, SCUBA-2 450 μm and 850 μm galaxies are not significantly dissimilar in their redshifts, luminosities, or SED peak wavelengths/temperatures, but that systems detected in only one of the two bands can be primarily distinguished based on their SED peak wavelengths (or temperatures) rather than their luminosities or redshifts.

4.4 Galaxies' distribution in z–$L_{\rm IR}$–$\lambda_{\rm peak}$ space

To better understand the relative selection differences between 450 μm and 850 μm, we use Monte Carlo methods to test for detectability as a function of the primary SED parameters, z, $L_{\rm IR}$ and $\lambda_{\rm peak}$. For a given redshift, luminosity and SED peak wavelength, we generate a number of SEDs satisfying those characteristics with varying emissivity, opacities and MIR power-law slopes and then compute the relative probability that a galaxy of those characteristics (z, $L_{\rm IR}$, and $\lambda_{\rm peak}$) is detectable in our survey. Instead of setting a strict flux density threshold which is representative of our sample (e.g. $S_{450} > 14.9$ mJy or $S_{850} > 2.9$ mJy, at $>3.6\sigma$), we inject galaxies of these given SED types into our jackknife maps and measure the $>3.6\sigma$ detectability.

We then assume an underlying distribution or density of galaxies in z–$L_{\rm IR}$–$\lambda_{\rm peak}$ space, as given by integrated-infrared luminosity functions (Le Floc'h et al. 2005; Caputi et al. 2007; Magnelli et al. 2011; Casey et al. 2012a; Gruppioni et al. 2013). However, the luminosity functions only constrain the distribution of galaxies in z and $L_{\rm IR}$, therefore we must assume some distribution of sources in SED peak wavelength, or temperature. The simplest assumption is that any galaxy SED, regardless of luminosity or redshift, should peak at 100 ± 40 μm. This model of the population fails since it predicts that 450 μm detected galaxies peak at $\langle z \rangle = 0.8$ while 850 μm detected galaxies peak at $\langle z \rangle = 2.8$. It also predicts that the populations have indistinguishable SED shapes and that nearly all 450 μm sources will be 850 μm detected. Both the predicted redshift and SED peak wavelength distributions and fraction of overlap between populations disagree significantly with our observations.

Adjusting the distribution of sources in SED peak wavelength produces results which are consistent with our observations. In other words, by invoking a correlation whereby $L_{\rm IR} \propto T_{\rm dust} \propto 1/\lambda_{\rm peak}$, we can predict $\langle z \rangle$ =1.5–2.0 for 450 μm sources and $\langle z \rangle$ =2.3–2.6 for 850 μm sources. Perhaps most pertinent, we can recover approximately the same overlap fraction of the population, namely that only ∼25–40 per cent of the 450 μm galaxies are 850 μm detected and vice versa. The predicted SED peak wavelength distributions also differ between 450 μm and 850 μm with this model. Unfortunately, our data are not significant enough to place

meaningful constraints on the slope of the underlying correlation between luminosity and peak wavelength, or provide better estimates to overlap fraction than ∼25 per cent. However, future large samples (N≈5000) selected at even more wavelengths across the submillimetre will provide meaningful constraints on the distribution of galaxies in z–$L_{\rm IR}$–$\lambda_{\rm peak}$ space.

These simulations can also be used to test the reliability of our SED fits. For instance, does SED fitting at 450 μm and 850 μm (versus a more fully sampled range of wavelengths) have a systematic effect on measured SED peak wavelength? Having generated sets of SEDs which describe a galaxy of known z, $L_{\rm IR}$ and $\lambda_{\rm peak}$, we can re-measure the SED characteristics by refitting the noise-added 450 μm and 850 μm photometry (and using an additional constraint at observed 24 μm). At high S/N, where galaxies are luminous enough to be detected at both wavelengths, the scatter in the log of measured SED peak wavelength is 0.05 dex with no systematic offset. At lower luminosities, where galaxies are more likely to be detected in only one of the two bands, the scatter in measured SED peak wavelength increases to 0.11 dex although there is still no systematic offset. We attribute the lack of systematic offset in measured peak wavelengths to the SCUBA-2 selection wavelengths, which sample the SED in significantly different regimes, e.g. the SED's peak and the SED's Rayleigh–Jeans tail. Even galaxies which are not formally detected in one of the two bands still has a flux density constraint at both wavelengths which, on average, provides an accurate estimate to the SED peak wavelength.

5 DISCUSSION

The ultimate goal of this work is the characterization of galaxies which emit at 450 μm and 850 μm, how they relate to other similarly selected galaxy populations, how they relate to the more extensively studied optical/UV-selected populations, and how important they are in the context of total star formation in the Universe. Follow-up studies can pursue source characterization in more detail. These initial observations from SCUBA-2 are also incredibly valuable in providing first insight of high-resolution bolometer observations which will become more commonplace with completion of the Large Millimeter Telescope (LMT) and the Cornell-Caltech Atacama Telescope (CCAT).

5.1 Are 450 μm and 850 μm populations different?

When contrasting the physical characteristics of 450 μm with 850 μm galaxies, like redshift distribution, luminosity and dust temperature, this work suggests that the two populations are quite similar. Are these similarities between 450 μm and 850 μm galaxies what we expect, given the lack of direct overlap of the samples?

If you naïvely assume there is little evolution or luminosity dependence of SMG SEDs, then selecting at shorter wavelengths than 850 μm would select a lower redshift population. If you take the mean redshift for 850 μm selected SMGs as $\langle z\rangle = 2.2$ and assume they peak at rest-frame 100 μm, then no change in SED type would predict the mean redshift for 450 μm selected galaxies is $\langle z\rangle \approx 0.5$. This assumption fails primarily since it does not consider that 850 μm selects galaxies almost exclusively on the Raleigh–Jeans tail of dust emission versus the peak. Adjusting this to reflect that 450 μm will select more galaxies near their peak (a factor of ∼2 in wavelength) implies that 450 μm galaxies should peak near $\langle z\rangle \approx 1$ (this test is similar to that in Section 4.4). Still, this is inconsistent with our data which predict that both populations peak at around $z \sim 2$.

Geach et al. (2013), who reference Roseboom et al. (2013), find a 450 μm redshift distribution which averages $\langle z\rangle = 1.3$, which is statistically different from our finding of $\langle z\rangle = 2.0 \pm 0.2$. Note, however, that the median distribution of the Geach et al. and Roseboom et al. sample is $z \sim 1.6$, significantly different from the average, and closer to the median value we measure. The offset between median redshifts between the two samples is likely due to the difference in depths of coverage between our surveys; the Geach et al. and Roseboom et al. work is a factor of ≈3 × deeper at its centre, while ours is a factor of ≈4 × larger, so our sample naturally picks up more luminous sources that might sit at higher redshifts than the fainter, lower redshift 450 μm population.

Despite the overlap in redshift distribution with 850 μm sources, 62–76 per cent of 450 μm sources are not 850 μm detected. Similarly, 61–81 per cent of 850 μm sources are not 450 μm detected. If the difference is not the sources' redshifts, then the SED properties could be the cause of the lack of overlap between the galaxy populations. Dust temperature has been thought to cause a significant selection difference between 850 μm–1 mm and <500 μm populations (Blain et al. 2004; Chapman et al. 2004; Casey et al. 2009b), where the former population is biased towards colder temperature SEDs. Before *Herschel* and SCUBA-2, this population of warm-dust high-z ULIRGs was called Optically Faint Radio Galaxies (OFRGs) or Submm-faint, Star-Forming Radio Galaxies (SFRGs), and was shown to exist in Casey et al. (2009b). In this paper, our finding that 850 μm only sources are statistically cooler (at a fixed redshift or luminosity) than 450 μm only sources is consistent with this hypothesis and is the most prominent difference between 450 μm only and 850 μm only populations, even though the average SED peak wavelength offset is only ∼20 μm at $z \sim 2$ (information presented in Fig. 14).

Certainly the lack of one-to-one overlap in the 450 μm and 850 μm samples implies that systems selected at any one wavelength in the FIR are *not* representative of *all* ultraluminous infrared star formation at high redshift. This becomes an issue when studies try to compare the relative importance of normal galaxies to infrared galaxies in the context of universal star formation and completeness for interpretation of the star formation rate density (SFRD).

5.2 Relation to 'normal' galaxies

Recent work has proposed that most submillimetre or infrared-luminous systems are a different, more extreme class of galaxy than most 'normal' star-forming galaxies in the Universe (e.g. Daddi et al. 2009; Genzel et al. 2010; Tacconi et al. 2010). This distinction is likely valid when speaking of the most luminous subset of SMGs. SMGs at $\approx 10^{13}\,L_\odot$ are nearly all found to be major merger-driven starbursts, much more extreme and much more rare than normal, more modest star-forming galaxies at comparable redshifts (e.g. Engel et al. 2010).

Although many SMGs exhibit extreme properties not seen in typical star-forming systems, this is not true of the entire infrared-luminous population. Here we measure a mean infrared luminosity of SCUBA-2 galaxies as ≈ 1–$2 \times 10^{12}\,L_\odot$, and the average star formation rates in our sample are $\approx 200\,M_\odot\,{\rm yr}^{-1}$, which is typical of high-mass ($>10^{10}\,M_\odot$) 'normal' galaxies at $z \approx 2$. Most normal galaxies at this epoch have specific star formation rates (sSFR) of 1–10 Gyr^{-1} while SCUBA-2 galaxies span sSFRs from 1 to 100 Gyr^{-1}, averaging 10 Gyr^{-1} at the upper end of sSFRs for normal galaxies. This is consistent with the idea that SMGs, although rare and extreme systems, can exhibit both properties of 'normal' star-forming

galaxies and extreme starbursts during different stages of evolution (as suggested in the models of Hayward et al. 2013).

Comparing the star formation rates from the UV/optical/NIR SED fits (dubbed 'SFR$_{\rm UV}$') directly with the star formation rates in the FIR, there is a substantial discrepancy. Despite the fact that SFR$_{\rm UV}$ is supposedly corrected for the effects of dust extinction, a cap on the maximum extinction introduced in the Le Phare SED fitting procedure implies that very dust obscured galaxies will have much higher SFR$_{\rm IR}$ than SFR$_{\rm UV}$. By our measure, SFR$_{\rm UV}$ is underestimating the star formation rate by a factor of $\gtrsim$13 (where the total SFR can be approximated as SFR$_{\rm IR}$ in infrared-luminous galaxies).

Table 9 gives the Le Phare-estimated quantities for star formation rate and stellar mass, as derived from the UV through to the NIR. These Scuba-2 sources are known to be unusual in that they *are* directly detected in the infrared, so the discrepancy between star formation rate measurements is not unexpected or new (Rosa-González, Terlevich & Terlevich 2002; Dye et al. 2008; Yun et al. 2012). Nevertheless, the discrepancy should emphasize the need to treat extinction carefully in model fits, especially for infrared-luminous galaxies. This potentially will alter the interpretation of galaxies' specific star formation rates. A future work, which will summarize our progress in confirming redshifts spectroscopically, will explore the total energy output of these galaxies in more depth and provide more context for comparing the sample to 'normal' galaxies.

5.3 Contribution to Universal star formation

Here we measure the net contribution of Scuba-2 galaxies to the SFRD of the Universe, or in other words, how significantly they impact net star formation in the Universe at any given epoch.

We compute SFRD estimates for the Scuba-2 population in this paper using the $1/V_{\rm max}$ method. Within a redshift bin, we sum each galaxy's star formation rate divided by accessible volume. Our survey area is roughly uniform over 394 arcmin^2, although individual sources' accessible volume is computed as a function of the local map noise. Note that we avoid estimating the luminosity functions directly given the limited statistics of this sample, where $\gtrsim$500 galaxies would be necessary to place accurate constraints in $L_{\rm IR}$ and z. The maximum accessible volume for a source is computed given that sources' selection wavelength, flux density and peak wavelength (either measured explicitly or assumed to be $\log \lambda_{\rm peak} = 2.05$ [450 μm] or 2.12 [850 μm] if unconstrained). We split the sample into five redshift bins spanning the range of our data: $0 < z < 1$, $1 < z < 2$, $2 < z < 3$, $3 < z < 4$ and $4 < z < 5$. We exclude the three individual sources which have luminosities $\log L_{\rm IR} > 13.6$, as they might be contaminated by AGN or could be lensed. Fig. 15 shows the results. The black points – representing the total contribution from 450 μm and 850 μm sources – should be regarded as lower limits as they only constitute narrow dynamic range in luminosity where our survey is sensitive ($>3.6\sigma$).

Fig. 15 shows us that (a) work done to date on measuring the SFRD from infrared/submm samples has been incomplete and is highly dependent on survey depth, but (b) with more multi-wavelength submillimetre surveys – like the Scuba-2 survey presented herein – we are beginning to see more of the infrared contribution to cosmic star formation which we had not previously seen. This is particularly evident at $z \sim$ 1–2, where 450 μm selected galaxies are dominant, while at $z \sim$ 2–3 450 μm and 850 μm selected galaxies contribute equally, and 850 μm selected galaxies might have a more prominent contribution to the SFRD at $z \sim$ 3. This survey is conducted at similar depths to previous submillimetre surveys; however it probes more of cosmic infrared-based star formation due to the multiwavelength submillimetre approach. Although deeper, wider surveys are necessary for complete surveys, probing a larger dynamic range in luminosity, there is no doubt that the multi-wavelength selection approach is also necessary, as these Scuba-2 samples represent a more complete subset of ultraluminous activity at these epochs than single-wavelength selected populations at 850 μm–1.2 mm.

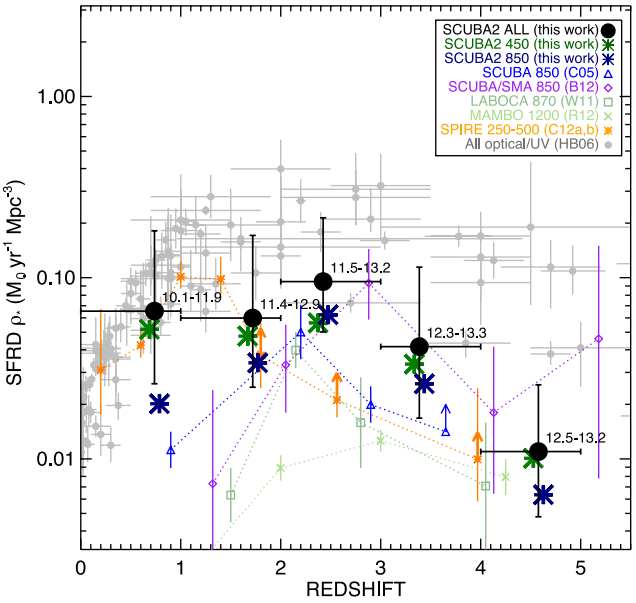

Figure 15. The estimated contribution of Scuba-2 sources in this paper to the cosmic SFRD. We split up the contribution estimates by selection wavelength, showing both the contribution from 450 μm selected (dark green) and 850 μm selected sources (navy), and we compare the total (black points) to literature SFRD values for similarly selected populations. Note that the total SFRD estimate is incomplete and only represents sources characterized at $>3.6\sigma$ in this paper and does not extrapolate to fainter luminosities; thus they should be regarded as lower limits. The range of luminosities represented by each black point is given adjacent to the point, in logarithmic solar luminosities. Galaxies with $\log L_{\rm IR} > 13.6$ are excluded from this estimate due to potential lensing bias. Literature comparisons are Chapman et al. (2005) 850 μm selected SCUBA sources (blue), Barger et al. (2012) SCUBA sources (purple), Wardlow et al. (2011) 870 μm selected LABOCA sources (light sea green), the Roseboom et al. (2012) 1.2-mm-selected MAMBO sources (light green) and the Casey et al. (2012a,b) *Herschel*-SPIRE 250–500 μm selected sources (orange).

The contribution from infrared-luminous galaxies appears 1–10 times less significant than the SFRD contribution from more normal, optical and UV selected galaxies (Hopkins & Beacom 2006). However, here the estimates from Hopkins & Beacom are corrected for dust extinction, in that they are scaled up by a factor proportional to the rest-frame UV slope. As addressed earlier by the discrepancy between optical SED-derived SFR and infrared SFR, there might be cause for concern if the dust extinction is not properly handled for some of the potentially dustier optically selected galaxies.

6 CONCLUSIONS

With simultaneous mapping at 450 μm and 850 μm, the Scuba-2 instrument is making substantial headway in the detection and characterization of infrared emission in the distant Universe. The ∼7 arcsec high-resolution blank-field mapping at 450 μm opens up a unique parameter space in high-z submillimetre science, and the

efficient mapping at 850 μm means that the confusion limit is reached in far less time than previous observations. This paper has presented initial SCUBA-2 mapping of a uniformly covered 394 arcmin^2 area in the COSMOS field at both 450 μm and 850 μm. We reach the following conclusions about our maps and the identification of point sources:

(i) The rms noise values of our maps are $\sigma_{450} = 4.13$ mJy and $\sigma_{850} = 0.80$ mJy at our map centres and find largely uniform rms over a 22.4 arcmin diameter (394 arcmin^2), the threshold where the rms exceeds two times the central rms value.

(ii) We extract point sources down to a 3.6σ detection threshold at 450 μm and 850 μm, where we find 78 and 99 sources, respectively. These extraction limits are determined via Monte Carlo simulations and an expected sample contamination rates of 3–5 per cent.

(iii) Source number counts at 450 μm and 850 μm are measured and we compare them to previous results at both wavelengths. We provide best-fitting double-power-law and Schechter function fits.

(iv) Positional uncertainties of 1–2.5 arcsec at 450 μm and 2–6 arcsec at 850 μm are estimated using Monte Carlo tests; we use this uncertainty to match both 450 μm and 850 μm sources to multiwavelength counterparts. The low positional uncertainties at 450 μm allow direct matching to counterparts in the optical/NIR, without relying on detection at 24 μm or radio wavelengths. Our 850 μm counterpart matching is done first by identifying 24 μm and radio counterparts, then if absent, taken as the nearest neighbour optical source.

(v) 56 per cent of all 450 μm galaxies and 40 per cent of all 850 μm galaxies lack both 24 μm and radio counterparts down to the deep field detection limits ($S_{24} \approx 80$ μJy and $S_{1.4} \approx 50$ μJy). This suggests that submillimetre samples relying on identification at either wavelength could be significantly biased, producing up to ∼1/2 misidentifications.

After the analysis of field number counts and counterpart matching techniques, we also analyse the population characteristics of 450 μm and 850 μm galaxies, how they differ from one another and how they relate to other high-redshift galaxy populations. We reach the following conclusions on their physical attributes.

(i) The redshift distributions for both populations is measured using the extensive COSMOS ancillary optical and NIR data. The 450 μm population peaks at $\langle z \rangle = 1.95 \pm 0.19$ while the 850 μm population peaks at $\langle z \rangle = 2.16 \pm 0.11$.

(ii) The FIR colour of SCUBA-2 sources [measured as $\log(S_{850}/S_{450})$] is found not to evolve significantly with redshift, although 450 μm identified galaxies have statistically 'bluer' FIR SEDs than 850 μm identified galaxies. Both 450 and 850 μm populations have colours which are inconsistent with a fixed SED peak wavelength (i.e. fixed temperature) across $0 < z < 5$.

(iii) 850 μm detected sources which are 450 μm dropouts peak at $z \approx 2$ and do not sit at higher redshifts as would be suspected if SED shape were not evolving or changing with infrared luminosity. Similarly 450 μm detected sources which are 850 μm dropouts also sit at $z \approx 2$ and not at lower redshifts. This is consistent with model populations where there is correlation between luminosity and dust temperatures, although whether or not that correlation evolves with z is unconstrained by these data.

(iv) Infrared luminosities, SED peak wavelengths and dust masses are estimated for both populations, and we determine that 450 μm galaxies and 850 μm galaxies are equally luminous and peak at similar rest-frame wavelengths. The most significant distinction is the SED peak wavelength of 450 μm only or 850 μm only detected galaxies, which differs by ∼20–50 μm (or 8–12 K, with 450 μm sources being the warmer subset).

(v) The star formation rates measured directly in the FIR exceed those predicted from UV/optical/NIR photometry by ∼13 times if restrictions are placed on extinction when generating best-fitting stellar population fits.

(vi) The contribution of these SCUBA-2 sources to the cosmic infrared luminosity density, or the SFRD, is measured to be higher than previous submm surveys, not due to depth, but due to multiwavelength selection. The 450 μm and 850 μm samples complement one another in that they only overlap by ∼30 per cent, so together they constitute a more complete census of luminous infrared activity than either subset. The total SFRD contribution we measure here is a factor of 2–3 times higher than previous single-wavelength ∼850 μm selection at the same depth. This demonstrates that multiple selection wavelengths are necessary for a complete census of infrared luminous star formation.

SCUBA-2 high-resolution 450 μm mapping has allowed the first detailed look at an infrared-luminous population not surveyed before. This work has revealed the necessity to exercise caution when identifying multiwavelength counterparts of submillimetre sources (especially those with a large beamsize) and the biases and limitations of previously analysed 850 μm–1 mm samples. Direct FIR interferometry still proves the best method for unequivocally identifying multiwavelength counterparts; however future work from CCAT will enable large field-of-view mapping with resolution significantly improved over JCMT, both at 850 μm and 450 μm. This work provides a stepping stone to link infrared-luminous systems to the more ubiquitous, 'normal' star-forming galaxies across a wide range of epochs, shedding light on galaxy evolution and the nature of cosmic star formation.

ACKNOWLEDGEMENTS

We would like to thank the referee for a very thoughtful and helpful report in reviewing this manuscript. CMC is generously supported by a Hubble Fellowship from Space Telescope Science Institute, grant HST-HF-51268.01-A. CCC and LC are generously supported by NSF grant AST 0709356. AB thanks the University of Wisconsin Research Committee with funds granted by the Wisconsin Alumni Research Foundation, and the David and Lucile Packard Foundation. CMC and DBS would like to thank the Aspen Center for Physics and the NSF grant 1066293 for many fruitful conversations with the community regarding this work during 'The Obscured Universe' summer workshop. The JCMT is operated by the Joint Astronomy Centre on behalf of the Science and Technology Facilities Council of the United Kingdom, the National Research Council of Canada, and (until 2013 March 31) the Netherlands Organization for Scientific Research. Additional funds for the construction of SCUBA-2 were provided by the Canada Foundation for Innovation. The authors also wish to recognize and acknowledge the very significant cultural role and reverence that the summit of Mauna Kea has always had within the indigenous Hawaiian community. We are most fortunate to have the opportunity to conduct observations from this mountain.

REFERENCES

Alaghband-Zadeh S. et al., 2012, MNRAS, 3329
Alexander D. M., Bauer F. E., Chapman S. C., Smail I., Blain A. W., Brandt W. N., Ivison R. J., 2005, ApJ, 632, 736
Aretxaga I. et al., 2011, MNRAS, 415, 3831

Armus L. et al., 2009, PASP, 121, 559
Banerji M., Chapman S. C., Smail I., Alaghband-Zadeh S., Swinbank A. M., Dunlop J. S., Ivison R. J., Blain A. W., 2011, MNRAS, 418, 1071
Barger A. J., Cowie L. L., Sanders D. B., Fulton E., Taniguchi Y., Sato Y., Kawara K., Okuda H., 1998, Nat, 394, 248
Barger A. J., Cowie L. L., Smail I., Ivison R. J., Blain A. W., Kneib J., 1999, AJ, 117, 2656
Barger A. J., Cowie L. L., Richards E. A., 2000, AJ, 119, 2092
Barger A. J., Wang W.-H., Cowie L. L., Owen F. N., Chen C.-C., Williams J. P., 2012, ApJ, 761, 89
Barnard V. E., Vielva P., Pierce-Price D. P. I., Blain A. W., Barreiro R. B., Richer J. S., Qualtrough C., 2004, MNRAS, 352, 961
Bertin E., Arnouts S., 1996, A&A, 117, 393
Bertoldi F. et al., 2007, ApJS, 172, 132
Béthermin M. et al., 2012, A&A, 542, 58
Blain A. W., Barnard V. E., Chapman S. C., 2003, MNRAS, 338, 733
Blain A. W., Chapman S. C., Smail I., Ivison R., 2004, ApJ, 611, 725
Borys C., Chapman S., Halpern M., Scott D., 2003, MNRAS, 344, 385
Bothwell M. S. et al., 2010, MNRAS, 405, 219
Bruzual G., Charlot S., 2003, MNRAS, 344, 1000
Caputi K. I. et al., 2007, ApJ, 660, 97
Casey C. M., 2012, MNRAS, 425, 3094
Casey C. M. et al., 2009a, MNRAS, 399, 121
Casey C. M., Chapman S. C., Muxlow T. W. B., Beswick R. J., Alexander D. M., Conselice C. J., 2009b, MNRAS, 395, 1249
Casey C. M. et al., 2012a, ApJ, 761, 140
Casey C. M. et al., 2012b, ApJ, 761, 139
Chapin E. L., Hughes D. H., Aretxaga I., 2009, MNRAS, 393, 653
Chapin E. L. et al., 2011, MNRAS, 411, 505
Chapin E. L. Berry D. S., Gibb A. G., Jenness T., Scott D., Tilanus R. P. J., Economou F., Holland W. S., 2013, MNRAS, 430, 2545
Chapman S. C., Helou G., Lewis G. F., Dale D. A., 2003, ApJ, 588, 186
Chapman S. C., Smail I., Blain A. W., Ivison R. J., 2004, ApJ, 614, 671
Chapman S. C., Blain A. W., Smail I., Ivison R. J., 2005, ApJ, 622, 772
Chen C.-C., Cowie L. L., Barger A. J., Casey C. M., Lee N., Sanders D. B., Wang W.-H., Williams J. P., 2013, ApJ, 762, 81
Clements D. L. et al., 2010, A&A, 518, L8
Condon J. J., 1992, ARA&A, 30, 575
Coppin K., Halpern M., Scott D., Borys C., Chapman S., 2005, MNRAS, 357, 1022
Coppin K. et al., 2006, MNRAS, 372, 1621
Coppin K. E. K. et al., 2008, MNRAS, 389, 45
Coppin K. et al., 2010, ApJ, 713, 503
Cowie L. L., Barger A. J., Kneib J.-P., 2002, AJ, 123, 2197
Daddi E. et al., 2009, ApJ, 694, 1517
Dempsey J. T. et al., 2013, MNRAS, 430, 2534
Downes A. J. B., Peacock J. A., Savage A., Carrie D. R., 1986, MNRAS, 218, 31
Dye S. et al., 2008, MNRAS, 386, 1107
Eales S., Lilly S., Gear W., Dunne L., Bond J. R., Hammer F., Le Fèvre O., Crampton D., 1999, ApJ, 515, 518
Eales S. et al., 2010, PASP, 122, 499
Eddington A. S., 1913, MNRAS, 73, 359
Elbaz D. et al., 2011, A&A, 533, A119
Engel H. et al., 2010, ApJ, 724, 233
Frayer D. T. et al., 2009, AJ, 138, 1261
Geach J. E. et al., 2013, MNRAS, 432, 53
Genzel R. et al., 2010, MNRAS, 407, 2091
Greve T. R. et al., 2005, MNRAS, 359, 1165
Gruppioni C. et al., 2013, MNRAS, 432, 23
Hayward C. C., Jonsson P., Kereš D., Magnelli B., Hernquist L., Cox T. J., 2012, MNRAS, 424, 951
Hayward C. C., Behroozi P. S., Somerville R. S., Primack J. R., Moreno J., Wechsler R. H., 2013, MNRAS, 434, 2572
Helou G., Soifer B. T., Rowan-Robinson M., 1985, ApJ, 298, L7
Hinshaw G. et al., 2009, ApJS, 180, 225
Hodge J. A. et al., 2013, ApJ, 768, 91
Holland W. S. et al., 1999, MNRAS, 303, 659
Holland W. S. et al., 2013, MNRAS, 430, 2513
Hopkins A. M., Beacom J. F., 2006, ApJ, 651, 142
Hughes D. H. et al., 1998, Nat, 394, 241
Hwang H. S. et al., 2010, MNRAS, 409, 75
Ilbert O. et al., 2009, ApJ, 690, 1236
Ilbert O. et al., 2010, ApJ, 709, 644
Ivison R. J. et al., 2010a, MNRAS, 402, 245
Ivison R. J. et al., 2010b, A&A, 518, L31
Karim A. et al., 2013, MNRAS, 432, 2
Kennicutt R. C., Jr, 1998a, ARA&A, 36, 189
Kennicutt R. C., Jr, 1998b, ApJ, 498, 541
Knudsen K. K., van der Werf P. P., Kneib J.-P., 2008, MNRAS, 384, 1611
Kovács A., Chapman S. C., Dowell C. D., Blain A. W., Ivison R. J., Smail I., Phillips T. G., 2006, ApJ, 650, 592
Kovács A. et al., 2010, ApJ, 717, 29
Laird E. S., Nandra K., Pope A., Scott D., 2010, MNRAS, 401, 2763
Le Floc'h E. et al., 2005, ApJ, 632, 169
Le Floc'h E. et al., 2009, ApJ, 703, 222
Lee N. et al., 2010, ApJ, 717, 175
Magnelli B., Elbaz D., Chary R. R., Dickinson M., Le Borgne D., Frayer D. T., Willmer C. N. A., 2011, A&A, 528, A35
Menéndez-Delmestre K. et al., 2009, ApJ, 699, 667
Meurer G. R., Heckman T. M., Calzetti D., 1999, ApJ, 521, 64
Neri R. et al., 2003, ApJ, 597, L113
Oliver S. et al., 2010, MNRAS, 405, 2279
Oliver S. J. et al., 2012, MNRAS, 424, 1614
Pilbratt G. L. et al., 2010, A&A, 518, L1
Polletta M. et al., 2007, ApJ, 663, 81
Pope A. et al., 2008, ApJ, 675, 1171
Reddy N. et al., 2012, ApJ, 744, 154
Rodighiero G. et al., 2011, ApJ, 739, L40
Rosa-González D., Terlevich E., Terlevich R., 2002, MNRAS, 332, 283
Roseboom I. G. et al., 2012, MNRAS, 419, 2758
Roseboom I. G. et al., 2013, MNRAS, preprint (arXiv:1308.4443)
Sanders D. B., Mirabel I. F., 1996, ARA&A, 34, 749
Sanders D. B., Soifer B. T., Elias J. H., Neugebauer G., Matthews K., 1988, ApJ, 328, L35
Sanders D. B. et al., 2007, ApJS, 172, 86
Scott S. E. et al., 2002, MNRAS, 331, 817
Scott K. S. et al., 2008, MNRAS, 385, 2225
Scoville N. et al., 2007, ApJS, 172, 1
Scoville N. et al., 2013, ApJS, 206, 3
Serjeant S. et al., 2008, MNRAS, 386, 1907
Smail I., Ivison R. J., Blain A. W., 1997, ApJ, 490, L5
Smail I., Ivison R. J., Blain A. W., Kneib J., 2002, MNRAS, 331, 495
Smolčić V. et al., 2012, A&A, 548, A4
Soifer B. T., Sanders D. B., Madore B. F., Neugebauer G., Danielson G. E., Elias J. H., Lonsdale C. J., Rice W. L., 1987, ApJ, 320, 238
Soifer B. T., Boehmer L., Neugebauer G., Sanders D. B., 1989, AJ, 98, 766
Swinbank A. M., Smail I., Chapman S. C., Blain A. W., Ivison R. J., Keel W. C., 2004, ApJ, 617, 64
Tacconi L. J. et al., 2006, ApJ, 640, 228
Tacconi L. J. et al., 2008, ApJ, 680, 246
Tacconi L. J. et al., 2010, Nat, 463, 781
Targett T. A., 2011, MNRAS, 412, 295
U V. et al., 2012, ApJS, 203, 9
Wang W.-H., Cowie L. L., Barger A. J., 2006, ApJ, 647, 74
Wang W.-H., Cowie L. L., Barger A. J., Williams J. P., 2011, ApJ, 726, L18
Wardlow J. L. et al., 2011, MNRAS, 415, 1479
Webb T. M. et al., 2003, ApJ, 582, 6
Wilson C. D. et al., 2008, ApJS, 178, 189
Younger J. D. et al., 2007, ApJ, 671, 1531
Younger J. D. et al., 2008, ApJ, 688, 59
Younger J. D. et al., 2009, MNRAS, 394, 1685
Yun M. S. et al., 2012, MNRAS, 420, 957

This paper has been typeset from a TEX/LATEX file prepared by the author.